Universitat Autònoma de Barcelona

# ELUCIDATING REACTION MECHANISMS FOR METAL-CATALYZED OXIDATIONS

Laia Vilella Arribas

Ph.D. Thesis

Chemistry

Supervisors:

David Balcells Badia

Agustí Lledós Falcó

Departament de Química

Facultat de Ciències

2015

*"Trees that are slow to grow bear the best fruit"*

Molière

# 5

# *Comparing Model Ir-based Water Oxidation Catalysts*

In this chapter a model hybrid-type catalyst for water oxidation reaction is presented. DFT calculations have been used to determine the viability of this catalytic system, which consists in a dimeric Ir complex attached on an $IrO_2$(110) surface. The stability and the catalytic activity of this hybrid system has been investigated and also compared to its corresponding homogeneous and heterogeneous constituents. This work was conducted during my stay in Stanford University under the supervision of Prof. Núria López from the ICIQ, Tarragona, and Dr. Aleksandra Vojvodic from SUNCAT Center for Interface Science and Catalysis, Stanford University.

## 5.1. Introduction

As mention in the previous chapter, the best homogeneous and heterogeneous water oxidation catalysts reported to date are based on Ir and Ru,[45,230–232,214] although they still require high overpotentials and in some cases, are not stable enough. Besides, the scarcity and the high cost of these precious metals also limit scaling them up to the industrial level.[233] To overcome all these issues, several approaches have been undertaken such as the synthesis of nature-inspired[234–236] and non-precious metal-based catalysts,[65,237,238] the addition of dopants[239,240] or the design of catalysts with high surface area.[241,242]

Another appealing strategy, although not very exploited yet, consists in anchoring active homogeneous water oxidation catalysts on a solid support (either active or inactive), thus creating a *hybrid-type* catalyst.[243,244] The fundamental idea behind these combined systems is that they might benefit from the individual properties of their homogeneous and heterogeneous constituents, as the limitations of ones are generally the main advantages of the others.[30] Homogeneous catalysts typically exhibit a high activity and are more tunable, but they lack the high stability and good electron transport shown by heterogeneous catalytic systems. To date, the few successful examples of this strategy include the very recent experimental works on water oxidation using an Ir-based HEDTA catalyst supported on $TiO_2$,[31] and a dimeric Ir complex anchored on tin-doped indium oxide nanoparticles.[32] However, the interplay between the anchored molecular catalyst and the support remains still unknown.

In this work, we investigated the viability of a hybrid water oxidation catalyst and the role of the surface in this type of systems by anchoring the iridium complex $[Ir_2(H_2O)_4(OH)_4(\mu\text{-}OH)_2]$ on the $IrO_2(110)$ surface through two oxygen atoms (Figure 5.1). We chose this dimeric Ir complex as homogeneous catalyst because it resembles the molecular species suggested to be involved in the formation of the purple-blue solution that catalyzes water oxidation.[245] Moreover, such a dimeric complex allows for comparison of the two main water oxidation mechanisms proposed in the literature, namely the water nucleophilic attack (WNA) and the direct coupling

(DC).[231,80,72], also known as interaction between two M–O units (I2M). On the other hand, we selected $IrO_2$ as heterogeneous catalyst because it is one of the most active pure metal oxides reported to date,[230,232] and it has also been computationally studied in detail.[53,54] In particular, we used the most stable $IrO_2$ facet, the (110), which features five- and six- coordinated Ir atoms at the surface, commonly known as *cus* and *bridge* sites.

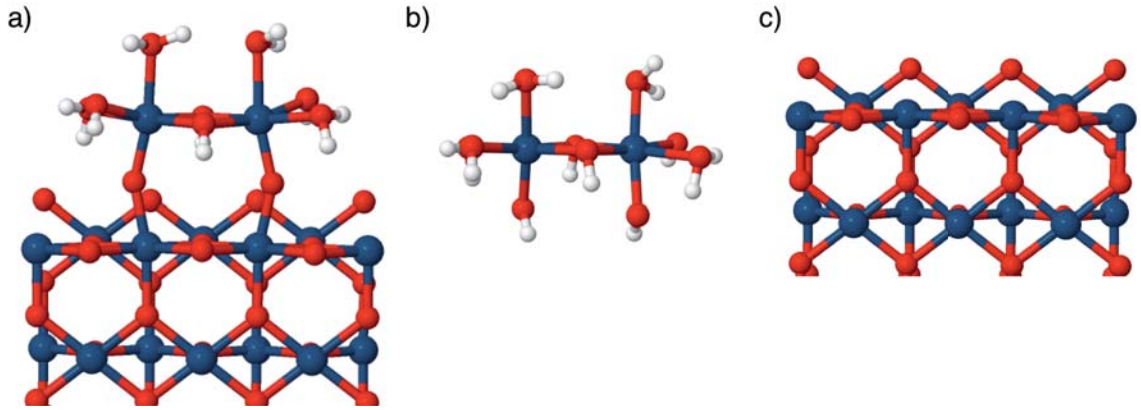


**Figure 5.1:** Side-view of the atomic structure for the investigated (a) hybrid, (b) homogeneous and (c) heterogeneous Ir-based catalysts. Color code: Ir (dark blue), O (red), and H (white).

It is important to note that the hybrid catalyst considered in this work was intended to serve as a model to probe the feasibility and operation of this type of systems, thus it has not be considered as a potential high-performance water oxidation catalyst.

## 5.2. Computational Details

The stability and activity of the considered Ir-based catalysts was investigated by means of DFT calculations in conjunction with the computational standard hydrogen electrode (SHE) model.[246] By setting the reference potential to be that of the standard hydrogen electrode, the free energy for the $e^- + H^+$ can be related to that of $1/2H_2$ in gas phase. This means that, at $pH = 0$ and 1bar of $H_2$ at 298 K, the reaction Gibbs energy of the $*AH \rightarrow A + e^- + H^+$ reaction is equal to the Gibbs energy of the $*AH \rightarrow A + 1/2H_2$, where the asterisk corresponds to an active site on the surface.

All the calculations in this study were performed at the periodic DFT level using the Perdew–Burke–Ernzenhof (PBE) exchange correlation functional[247] as implemented in the VASP code, version 5.3.2.[248,249] The core electrons of the Ir, O, and H atoms were replaced by projector-augmented wave (PAW) pseudopotentials,[197] whereas their valence electrons were expanded in plane waves with a kinetic energy cutoff of 450 eV. However, the lattice parameters for the bulk $IrO_2$ structure were optimized using a higher cutoff energy of 600 eV and a 9×9×13 Monkhorst Pack (MP) k-point grid. The obtained lattice parameters were $a_{calc} = b_{calc} = 4.543$ Å and $c_{calc} = 3.187$ Å, which are in very good agreement with previous theoretical findings[250,251] and experimental values of $a_{exp} = b_{exp} = 4.505$ Å and $c_{exp} = 3.159$ Å.[252] To model the heterogeneous $IrO_2$ surface catalyst, we chose a 2x1 supercell including a slab containing nine atomic layers of the most stable (110) facet[253] and a vacuum of at least 13 Å. Geometry optimizations for this system were carried out using a 5×5×1 MP k-point mesh allowing the adsorbed species (O*, HOO*, OO*, $H_2O$* and HO*) and the five topmost atomic layers to relax, while keeping the rest of the atoms fixed at their bulk positions. When it comes to the homogeneous $[Ir_2(H_2O)_4(OH)_4(\mu\text{-}OH)_2]$ catalyst, it was simulated using a cell of 18x15x15 Å in size and sampling the Brillouin zone at the Γ–point. Moreover, we always considered neutrally charged complexes to avoid the complexity of dealing with charged species in periodic calculations.

To model the hybrid catalyst, we anchored the dimeric Ir complex on top of the $IrO_2(110)$ surface with a 6x2 periodicity through two oxygen atoms to the *cus* sites of the surface. Due to the considerable size of the combined system, calculations for this catalyst were performed at the Γ–point. However, the energy convergence with respect to the k-point sampling was examined for selected species using a denser 2x3x1 k-point mesh, obtaining energy differences within 0.02 eV (Table A5.1 in Appendix). Geometry optimizations for this catalyst were performed relaxing the atoms in the attached dimer and the three topmost surface layers.

For the three model Ir catalysts, total energies were converged with a threshold of $10^{-5}$ eV in the self-consistent field and geometries were relaxed until the energy threshold of $10^{-4}$ eV was fulfilled. Spin-polarized calculations were carried out when needed, relaxing the total magnetic moment during

the self-consistent cycles. The nature of all the stationary points was confirmed by calculating the vibrational frequencies of the adsorbed species and metal atoms directly coordinated to them. Contributions to the Gibbs free energies for the adsorbates in the gas phase and on the surface were calculated at T = 300 K and p = 1 atm. However, in the case of $H_2O$, we used p = 0.035 atm, as it is the pressure at which vapor water is in equilibrium with liquid water at T = 300 K. It is important to note that in this work we only studied the thermochemistry of the reaction, thus all the energy barriers corresponds to Gibbs energies differences of the intermediates.

The Gibbs energies for the three catalytic systems, *G*, were calculated assuming that the electronic and vibrational contributions to this term are the most relevant ones, and by approximating the electronic term to the potential energy:

$$G \approx E + G_{vib} \quad [5.1]$$

$G_{vib}$ were calculated as the sum of the zero-point vibrational energy (ZPVE), the vibrational enthalpy and the vibrational entropy term as follows:

$$G_{vib} \approx ZPVE + H_{vib} - TS_{vib} \quad [5.2]$$

$$ZPVE = \frac{1}{2}\sum_{i=1}^{m} h\nu_i \quad [5.3]$$

$$H_{vib} = \sum_{i=1}^{m}\left(h\nu_i/(e^{h\nu_i/k_BT} - 1)\right) \quad [5.4]$$

$$TS_{vib} = k_BT\left[\sum_{i=1}^{m}\left(\frac{h\nu_i}{k_BT(e^{h\nu_i/k_BT}-1)} - \ln\left(1 - e^{-h\nu_i/k_BT}\right)\right)\right] \quad [5.5]$$

being *m* the total number of vibrational modes that result from vibrating the adsorbate atoms and the Ir atoms directly coordinated to them. Thus, the *G* term results in:

$$G \approx E + \sum_{i=1}^{m}\left[h\nu_i\left(\frac{1}{2} + \frac{1}{(e^{h\nu_i/k_BT}-1)}\right) - k_BT\left(\frac{h\nu_i}{k_BT(e^{h\nu_i/k_BT}-1)} - \ln\left(1 - e^{-h\nu_i/k_BT}\right)\right)\right] \quad [5.6]$$

On the other hand, the Gibbs energies for gas molecules ($H_2$ and $H_2O$) were

calculated using the NIST-JANAF thermodynamic tables (http://kinetics.nist.gov/janaf/). In order to avoid introducing the DFT error in the energetics related to molecular oxygen the Gibbs energy for the reaction $2H_2O \rightarrow O_2 + 2H_2$ was fixed to the experimentally value of 4.92 eV. [246,254,255]

In this work, we noted that the correction to the Gibbs energy for the proton-coupled electron transfer (PCET) reactions was basically constant and equal to 0.3 eV. Therefore, for the study of the consecutive deprotonations for the dimeric Ir complex and the hybrid catalyst (Figures 5.5 and 5.8), we calculated the Gibbs reaction energies adding 0.3 eV to the calculated energies.

## 5.3. Results

### 5.3.1. Stability of the Ir-Hybrid Catalyst

Firstly, the stability of the hybrid catalyst was examined by computing the adsorption energy of the dimeric Ir complex to the $IrO_2(110)$ surface as follows:

$$\Delta E_{ads} = E_{H2} + E_{hybrid} - E_{dimer} - E_{IrO2} \qquad [5.7]$$

where $E_{H2}$, $E_{hybid}$, $E_{dimer}$, and $E_{IrO2}$ are the potential energies for molecular hydrogen, and for the hybrid system, dimeric Ir complex and $IrO_2(110)$ surface, respectively. Importantly, the obtained adsorption energy from Eq [5.7] was -2.19 eV, indicating that indeed the dimeric Ir catalyst is strongly attached to $IrO_2(110)$ through the two oxygen linkers. Another interesting feature was that the optimized Ir−Ir bond distance in the supported Ir dimer (3.207 Å) almost matches with the Ir−Ir distance in the $IrO_2(110)$ surface (3.190 Å). In fact, this particular hybrid catalyst containing only aqua and hydroxo ligands might be also conceived as a defect or as an extension of the $IrO_2(110)$ surface, which would explain the strong interaction between its homogeneous and heterogeneous constituents, predicted by calculations. To gain further insight into this interaction, the charge density difference between the molecular and the surface fragments was evaluated (Figure 5.2). This analysis revealed that both Ir atoms from the adsorbed

complex and the surface provide electron density to the O-linkers, thus making these bonds particularly strong.

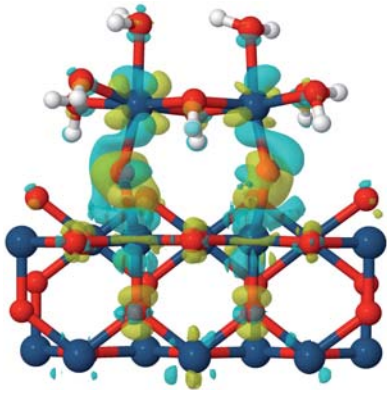

**Figure 5.2:** Charge density difference analysis of the complex $[Ir_2(H_2O)_4(OH)_4(\mu\text{-}OH)_2]$ supported on a clean $IrO_2(110)$ surface. Yellow isosurface indicates accumulation of charge density, whereas cyan indicates depletion. Only part of the $IrO_2(110)$ surface is shown for the sake of clarity.

The stability of the hybrid system was further assessed by investigating the desorption of the dimeric Ir complex with the concomitant hydroxylation of the surface upon the attack of two solvent water molecules, $\Delta E_{des}$, with the following equation:

$$\Delta E_{des} = +2E_{H2O} + E_{hybid} - E_{dimer} - E_{IrO2+2OH} \quad [5.8]$$

where $E_{H2O}$ and $E_{IrO2+2OH}$ are the potential energies for a water gas molecule and the $IrO_2(110)$ surface with two OH groups adsorbed in *cus* positions, respectively. Calculations showed that this deactivation route is a highly endothermic process (1.54 eV), which reinforces the stability of this hybrid-type system.

### 5.3.2. Catalytic Active Species

Before evaluating the water oxidation activity for the hybrid system and its individual constituents, it is necessary to first determine what is the active species of these catalysts under relevant reaction conditions. To this end, for each of them we considered a number of potential species that might exist in aqueous solution and plot their corresponding Pourbaix diagrams. This

representation shows the relative Gibbs energies as a function of the *pH* and the applied voltage (*U*), which allows to map out the most stable species (or surfaces) at certain conditions (Appendix). To construct these diagrams a reference surface (species) has to be considered in order to relate the free energies of the other surfaces (species). In the case of the heterogeneous system our reference structure corresponds to the clean $IrO_2(110)$ surface. On the other hand, for the dimeric Ir complex and the hybrid system we chose the species with the highest content of H atoms as reference. Moreover, we drew a dashed line in the Pourbaix diagrams, which indicates the thermodynamic potential for water oxidation as a function of *pH*, thus all the species that appear above this line could be considered as active species.

### 5.3.2.1. Active Species for the $IrO_2(110)$ Surface Catalyst

To construct the Pourbaix diagram for the $IrO_2(110)$ surface shown in Figure 5.3, we considered up to 19 different H, O and OH surface coverages (Scheme A5.1 in Appendix). In this case, since the area above the dashed line (pink region in the Pourbaix diagram) fully corresponds to a surface with all Ir-*cus* sites occupied by O atoms, we only considered this coverage for $IrO_2(110)$ surface under typical water oxidation conditions, which is in agreement with previous theoretical findings.[53,256]

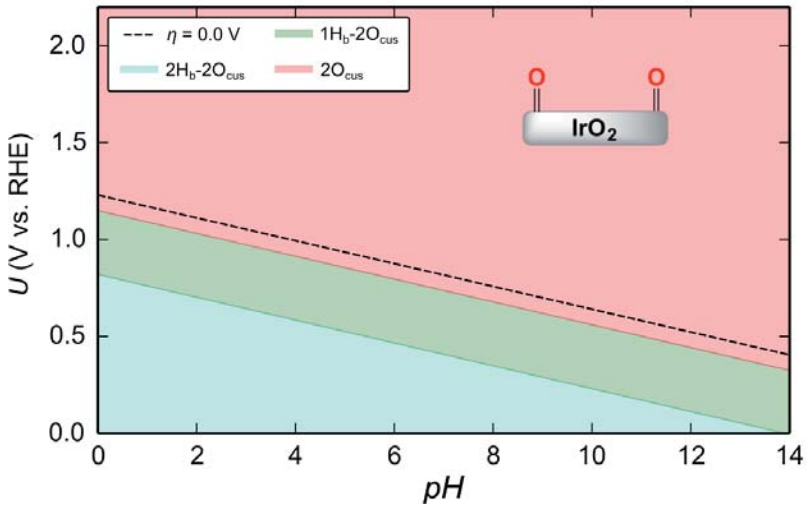


**Figure 5.3:** Calculated Pourbaix diagram for the $IrO_2(110)$ surface. The different coverages are labeled as $n\mathrm{H_b}$-$m\mathrm{O}_{cus}$, where $n\mathrm{H_b}$ is the number of H atoms at the $\mathrm{O_{bridge}}$ positions and $m\mathrm{O}_{cus}$ is the number of $\mathrm{O}_{cus}$. Gibbs energies are in eV.

### 5.3.2.2. Active Species for the Dimeric Ir Catalyst

Due to the vast number of possible protonation states for the dimeric Ir catalyst, an extensive analysis to determine the most likely active species was conducted. We started by exploring several consecutive deprotonations of the $[Ir_2(H_2O)_4(OH)_4(\mu\text{-}OH)_2]$ complex at $pH$ = 0 and 1.23 V. Under these conditions, calculations indicated that water molecules are preferentially deprotonated until a fully hydroxylated dimeric Ir(V) species is obtained (Figure 5.4). Species involved in the different deprotonation pathways are depicted in Figure 5.5.

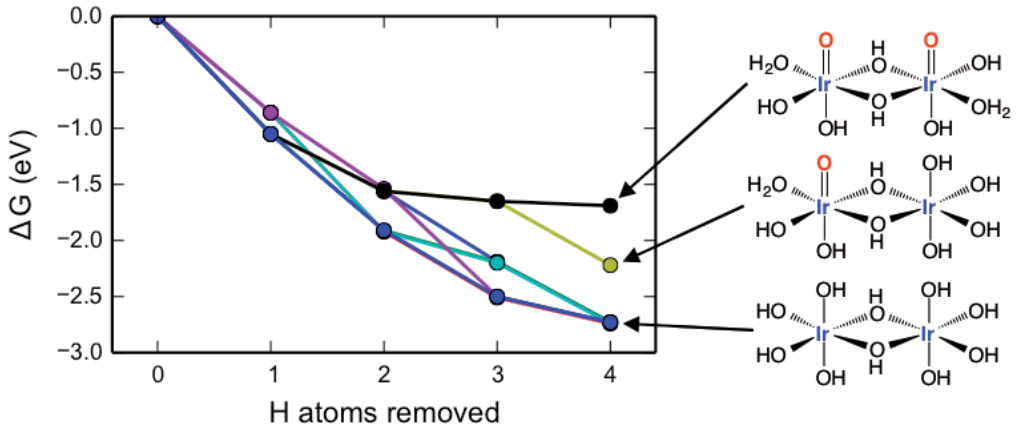


**Figure 5.4:** Graphical representation of the Gibbs energies (in eV) as a function of the number of H atoms removed from the $[Ir_2(H_2O)_4(OH)_4(\mu\text{-}OH)_2]$ complex at $pH$ = 0 and 1.23 V.

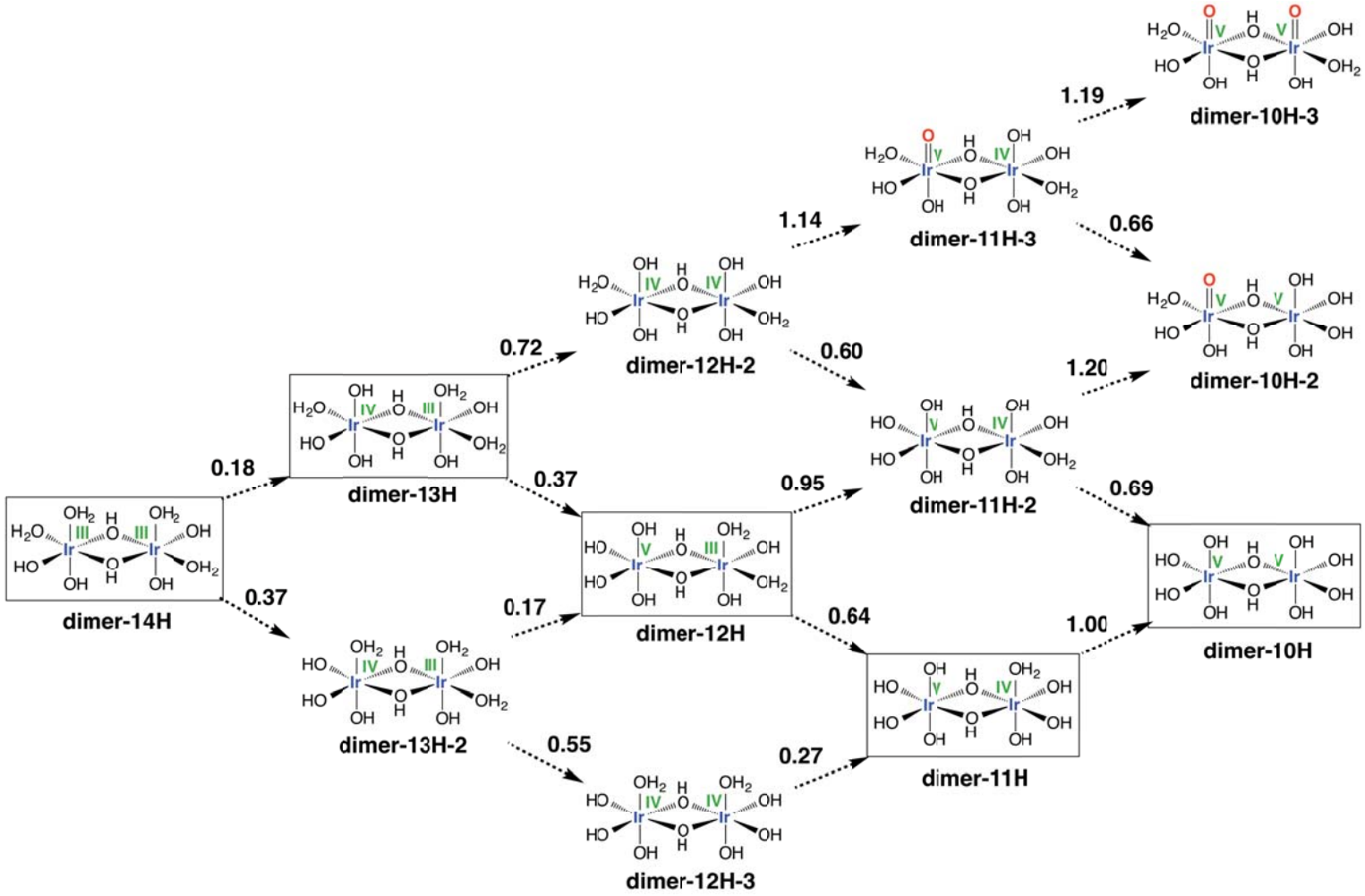


**Figure 5.5:** Consecutive deprotonation pathways investigated for the dimeric Ir complex. Gibbs energy differences are given in eV at $pH$ = 0 and 1.23 V. The Ir species involved in the lowest energy deprotonation pathways are marked with solid rectangles. Formal oxidation states of Ir atoms are indicated in green.

From the dimeric complexes with 10 hydrogen atoms, we further examined all the possible isomers with different hydrogen content and formal Ir oxidation states up to +7 (Scheme A5.2 in Appendix). It is worth mentioning that the existence of $IrO_4$ and $[IrO_4]^+$ species with oxidation states of +8 and +9 have been reported,[257,258] although they have been only characterized in rare-gas matrices. Therefore, to construct the Pourbaix diagram we considered all the above dimeric Ir complexes with oxidation states up to +7.

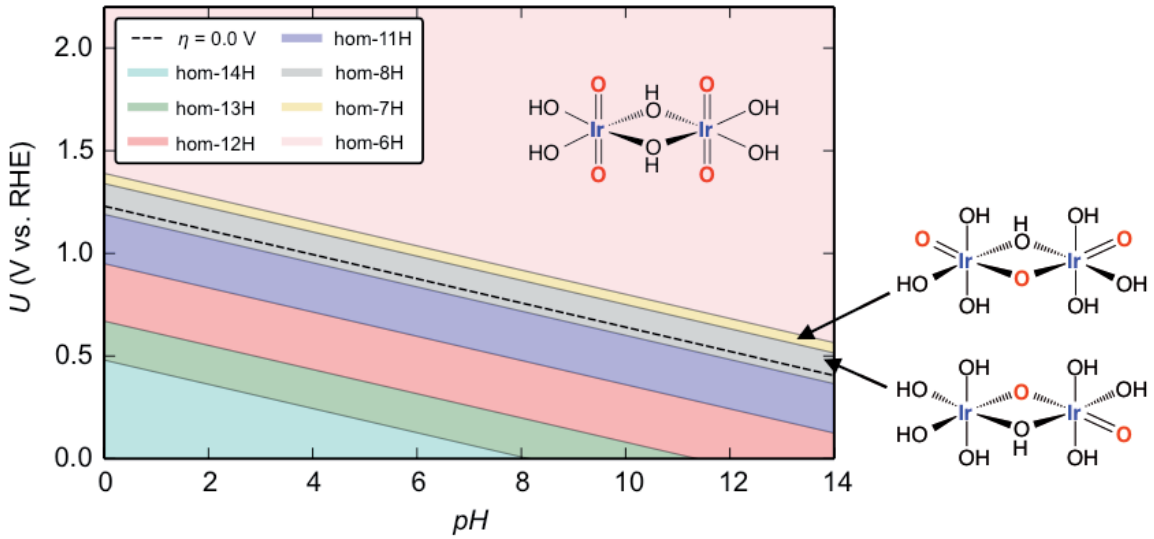


**Figure 5.6:** Calculated Pourbaix diagram for the dimeric Ir complex. The most stable species with a given number of hydrogen atoms are named as *n*H, where *n* is the number of H atoms contained in each species. Gibbs energies are given in eV.

According to the Pourbaix representation showed in Figure 5.6, there are 3 species above the dashed line. Nevertheless, the potential range at which the two first species are stable is very narrow (gray and yellow region in the Pourbaix diagram), which indicates the low probability to have these species. Therefore, we only considered the dimeric species with a total of 6 hydrogen atoms (pink region in the Pourbaix Diagram) since it is stable within a much wider range of potentials. More specifically, this species is a symmetric Ir(VII)/Ir(VII) dimer with hydroxo- and oxo-ligands in the equatorial and axial planes, respectively (inset Figure 5.6).

### 5.3.2.3. Active Species for the Ir-Hybrid Catalyst

Due to the considerable size of the hybrid catalyst and the large number of possible protonation states of the adsorbed dimeric Ir complex, for this system we assumed the same surface coverage obtained in the Pourbaix diagram for $IrO_2$ (110) surface (Figure 5.3); that is, a surface with all *cus* sites fully covered by O atoms. As far as the anchored Ir dimer is concerned, we calculated the same consecutive deprotonations as investigated for the dimeric Ir complex (Figure 5.8). Nevertheless, in contrast to this catalyst, calculations show that equatorial water molecules in the hybrid system are more difficult to deprotonate due to the H-bonds established between the aqua ligands and the $O_{cus}$ surface atoms. Also interesting is the fact that, at $U$ = 1.23 V, the energies required to deprotonate the supported Ir dimer (Figure 5.7) are much less exothermic than the ones calculated for the dimeric Ir complex (Figure 5.4), which suggests that Ir atoms in the hybrid system are less prone to be oxidized due to the presence of the surface. Species involved in the different deprotonation pathways are depicted in Figure 5.8.

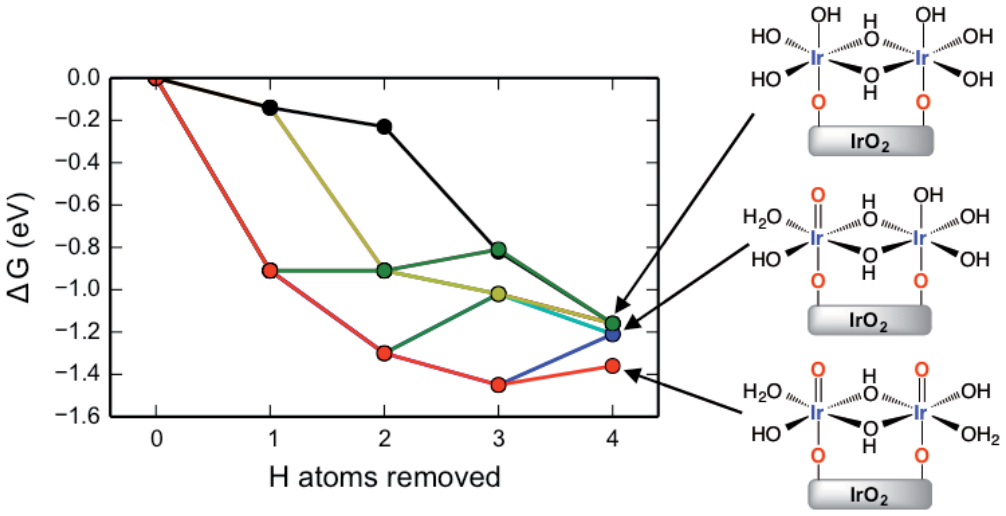


**Figure 5.7:** Graphical representation of the Gibbs energies (in eV) as a function of the number of H atoms removed from the hybrid system at $pH$ = 0 and 1.23 V.

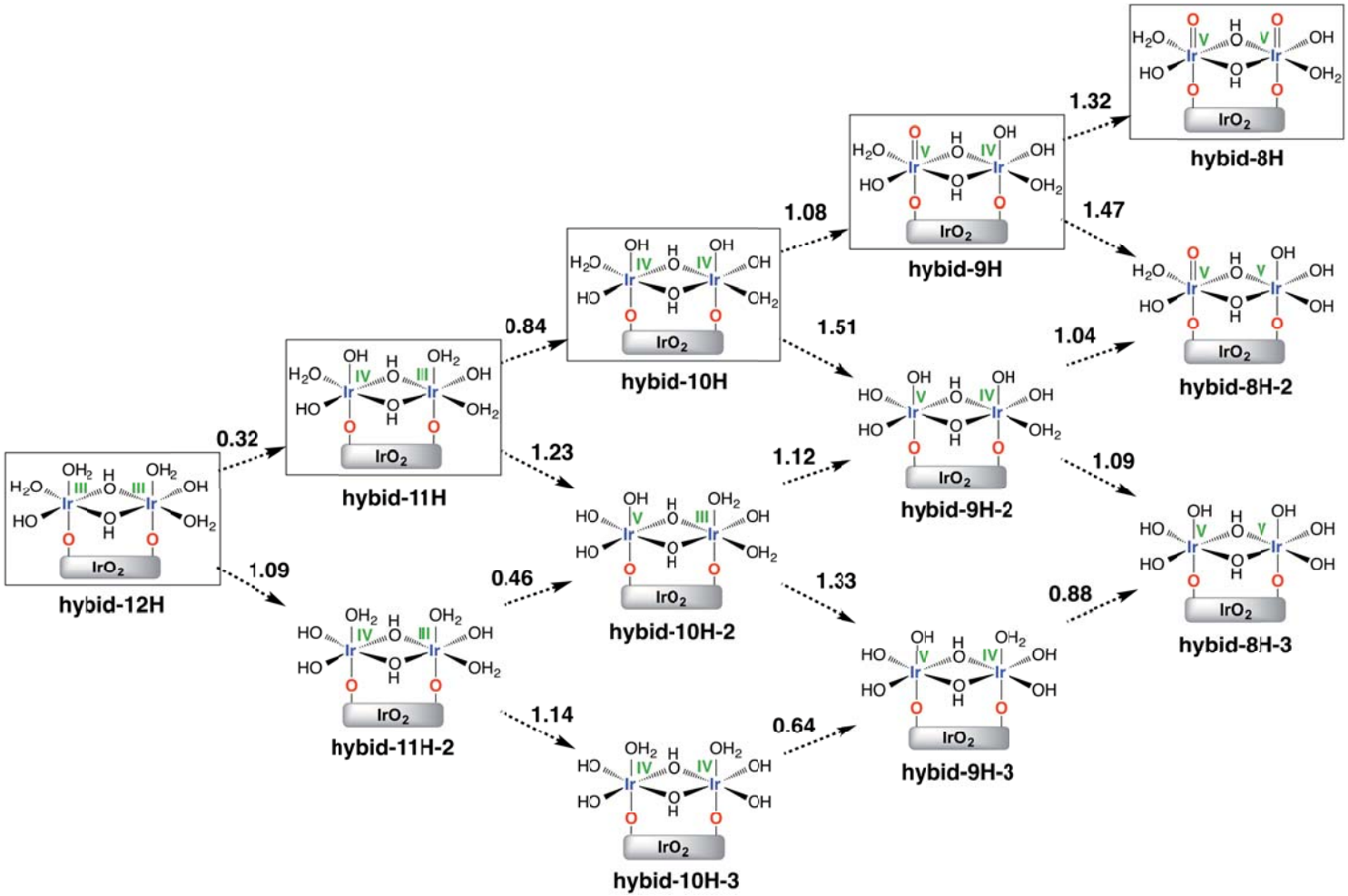


**Figure 5.8:** Consecutive deprotonation pathways investigated for the hybrid system. Gibbs energy differences are given in eV at $pH = 0$ and 1.23 V. The Ir species involved in the lowest energy deprotonation pathways are marked with solid rectangles. Formal oxidation states of Ir atoms are indicated in green.

To construct the Pourbaix diagram for the hybrid system, we included all the species involved in the consecutive deprotonations of the adsorbed dimeric Ir complex and several further oxidized species with formal Ir oxidation states up to +6 (Scheme A5.3 in Appendix). This representation reveals that there are two hybrid species that might exist at relevant water oxidation potentials (insets Figure 5.9). The first one, which is stable in the range from 1.3 to 1.8 V (purple region in Figure 5.9), contains 7 hydrogen atoms and corresponds to an Ir species with the equatorial plane fully hydroxylated except one position that has an aqua ligand. Conversely, the other is stable at potentials higher than 1.8 V and is analogous to the active species found for the dimeric Ir complex. Interestingly, the potentials required to reach the same Ir oxidation states as for the dimeric Ir complex are significantly higher in the hybrid system, which can be explained with the lower tendency of the hybrid system to be oxidized due to the presence of the surface.

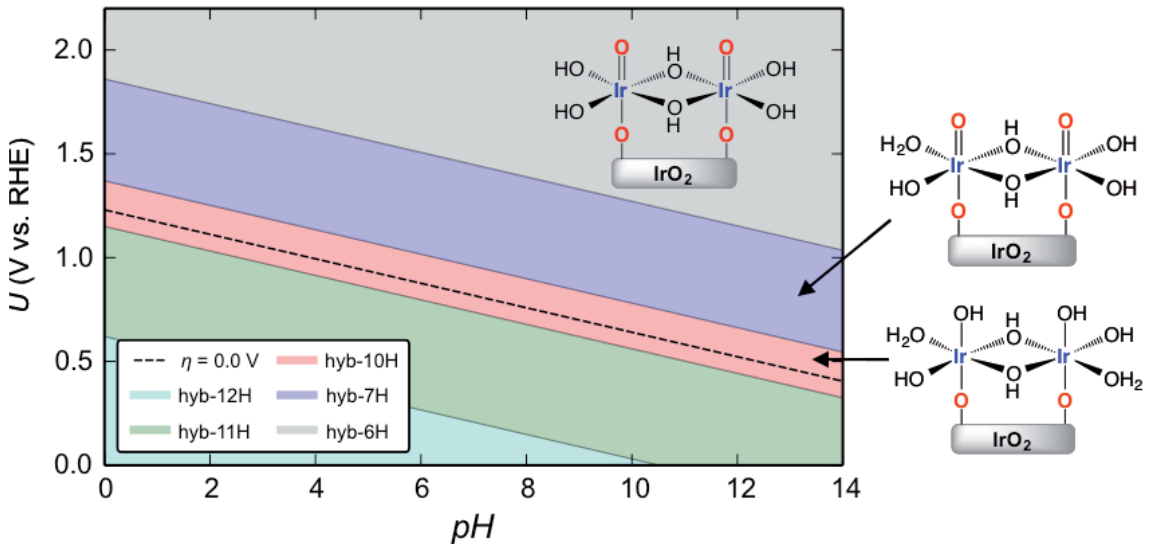


**Figure 5.9:** Calculated Pourbaix diagram for the hybrid system. The most stable species with a given number of hydrogen atoms are named as *n*H, where *n* is the number of H atoms contained in each species. Gibbs energies are given in eV.

### 5.3.3. Reaction Mechanisms

Based on the active species derived from the Pourbaix diagrams (Figures 5.3, 5.6, 5.9), we next evaluated the activity of these three catalytic systems in the water oxidation reaction. In order to compare the activity for these catalysts,

for each of them we determined the potential-limiting step, defined as the onset potential at which all the steps become thermodynamically downhill. The difference between the limiting and the standard water oxidation potentials is the so-called theoretical overpotential, $\eta$:[246]

$$\eta = max\left(\frac{\Delta G_i}{e}\right) - 1.23\ (at\ pH = 0) \qquad [5.9]$$

where $\Delta G_i$ is the Gibbs reaction energy of each step in eV.

#### 5.3.3.1. Water Oxidation with $IrO_2$(110) Surface Catalyst

For rutile oxides, water oxidation in acidic medium has been proposed to occur through a WNA mechanism (WNA-1)[9,53] consisting of the following four electrochemical steps:

(1) $H_2O_{(l)} + O^* \rightarrow HOO^* + e^- + H^+$

$$\Delta G_1 = \Delta G_{HOO*} - \Delta G_{O*} - eU + k_B T ln a_{H+}$$

(2) $HOO^* \rightarrow O_{2(g)} + * + e^- + H^+$

$$\Delta G_2 = 4.92 - \Delta G_{HOO*} - eU + k_B T ln a_{H+}$$

(3) $* + H_2O_{(l)} \rightarrow HO^* + e^- + H^+$

$$\Delta G_3 = \Delta G_{HO*} - eU + k_B T ln a_{H+}$$

(4) $HO^* \rightarrow O^* + e^- + H^+$

$$\Delta G_4 = \Delta G_{O*} - \Delta G_{HO*} - eU + k_B T ln a_{H+}$$

In the first step, the OOH* intermediate is formed by the nucleophilic attack of a water molecule to the $O_{cus}$. This intermediate evolves to molecular oxygen leaving a vacancy on the Ir-*cus* position. Then, a second water molecule is coordinated to the open vacant site and by two subsequent PCET the $O_{cus}$ is

recovered. The sum of the Gibbs energies of the four reaction steps was fixed to the formation energy of $O_2$ (4.92 eV). The Gibbs energy of the intermediates along the reaction path, $\Delta G_{HO*}$, $\Delta G_{O*}$ and $\Delta G_{HOO*}$ were calculated relative to $H_2O$ and $H_2$ in the gas phase at $U = 0$ V. The effect of the bias is also included on all states involving an electron by shifting the energy of these states by $-eU$, where $U$ is the electrode potential. Moreover, at $pH$ different from 0 we correct the Gibbs energy of the $H^+$ by the concentration dependence of the entropy: $\Delta G(pH) = k_B T \cdot ln10 \cdot pH$.

Based on the WNA-1 mechanism, we proposed a mechanistic variant that does not entail calculating unsaturated octahedral Ir atoms at the surface (WNA-2). It consists in replacing (2) and (3) by the alternative steps:

(2') HOO* → OO* + $e^-$ + $H^+$

$$\Delta G_{2'} = \Delta G_{OO*} - \Delta G_{OOH*} - eU + k_B T ln a_{H+}$$

(3') OO* + $H_2O$ (l) → $O_2$ (g) + HO* + $e^-$ + $H^+$

$$\Delta G_{3'} = 4.92 + \Delta G_{HO*} - \Delta G_{OO*} - eU + k_B T ln a_{H+}$$

in which a PCET reaction from the HOO* intermediate yields an adsorbed OO* species that subsequently evolves to molecular oxygen and a HO* group generated via a second PCET. According to our calculations, the thermodynamically most energy demanding step in the WNA-1 corresponds to the desorption of $O_2$, whereas in the WNA-2 it is the generation of the OOH* species (step 1), which involves the formation of the O–O bond. This reaction steps result in overpotentials of 0.61 and 0.40 V for the WNA-1 and WNA-2 mechanisms, respectively (Figure 5.10). Thus, this alternative pathway is more favorable by 0.21 V, and therefore, we considered this mechanism when comparing water oxidation at the $IrO_2$(110) surface with the other model catalysts. Moreover, the calculated overpotential of 0.40 V via the WNA-2 mechanism is in good agreement with the reported experimental value of 0.36 V at a current density of 10 mA·cm$^{-2}$.[230,232]

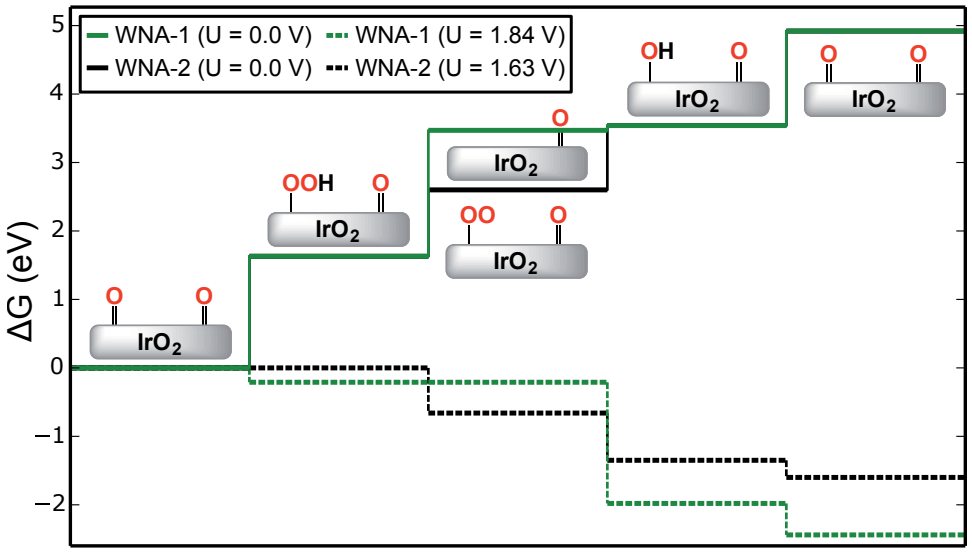


**Figure 5.10.** Gibbs energy diagram for the water oxidation reaction using $IrO_2(110)$ as catalyst. The WNA-1 mechanism is represented in green, while the WNA-2 in black.

### 5.3.3.2. Water Oxidation with the Dimeric Ir Catalyst

For homogeneous water oxidation catalysts, both WNA and DC reaction mechanisms have been shown to operate depending on the nature of the catalyst.[72] Thus, for the dimeric Ir complex we explored these two mechanisms, as well as several variants of them (Scheme A5.4 in Appendix). In the case of the WNA mechanism, we found that the lowest energy pathway is the same as for $IrO_2$ (110) (Figure 5.10), which corresponds to the O–O bond formation (Figure 5.11). Nevertheless, the theoretical overpotential for the dimeric Ir complex, 1.02 V, was significantly higher than that of the $IrO_2(110)$ surface, 0.40 V.

On the other hand, the lowest energy path obtained for the DC mechanism consist of:

(1) $O^* + O^* \rightarrow {}^*OO^*$

$$\Delta G_1 = \Delta G_{*OO*} - 2\Delta G_{O*}$$

(2) $^*OO^* + H_2O_{(l)} \rightarrow OO^* + HO^* + e^- + H^+$

$\Delta G_2 = \Delta G_{OO*} + \Delta G_{OH*} - \Delta G_{*OO*} - eU + k_B T ln a_{H+}$

(3) OO* + HO* + $H_2O_{(l)}$ → 2HO* + $O_{2(g)}$ + $e^-$ + $H^+$

$\Delta G_3 = 4.92 + \Delta G_{HO*} - \Delta G_{OO*} - eU + k_B T ln a_{H+}$

(4) 2HO* → HO* + O* + $e^-$ + $H^+$

$\Delta G_4 = \Delta G_{O*} - \Delta G_{HO*} - eU + k_B T ln a_{H+}$

(5) HO* → O* + $e^-$ + $H^+$

$\Delta G_5 = \Delta G_{O*} - \Delta G_{HO*} - eU + k_B T ln a_{H+}$

where the asterisk indicates that the O is coordinated to an Ir atom.

This mechanism starts with the coupling between two iridium bis-oxo moieties leading to a $\mu$-1,2-peroxo intermediate (Figure 5.11). From this species, the reaction may proceed to the cleavage of one Ir–O bond promoted by the nucleophilic attack of a water molecule and resulting in the formation of a superoxide and an OH group generated via PCET. This superoxide species subsequently evolves to molecular oxygen with the coordination of a second water molecule, which gives rise to an OH group through a second PCET. Finally, the starting bis-oxo species is regenerated after two consecutive PCET reactions, thus closing the catalytic cycle.

The potential at which all the electrochemical steps in the DC mechanism become downhill in energy is 1.57 V (Figure 5.11). However, an additional energy barrier of at least 0.59 eV is required for the formation of the $\mu$-1,2-peroxo species (*OO*), which corresponds to a chemical step, and therefore, it is not affected by the applied bias. The fact that the energy for this chemical step is rather low and the overpotential for this mechanism is much smaller than that of the WNA-2 (0.34 *versus* 1.02 V), suggests that the DC is favored at room temperature.

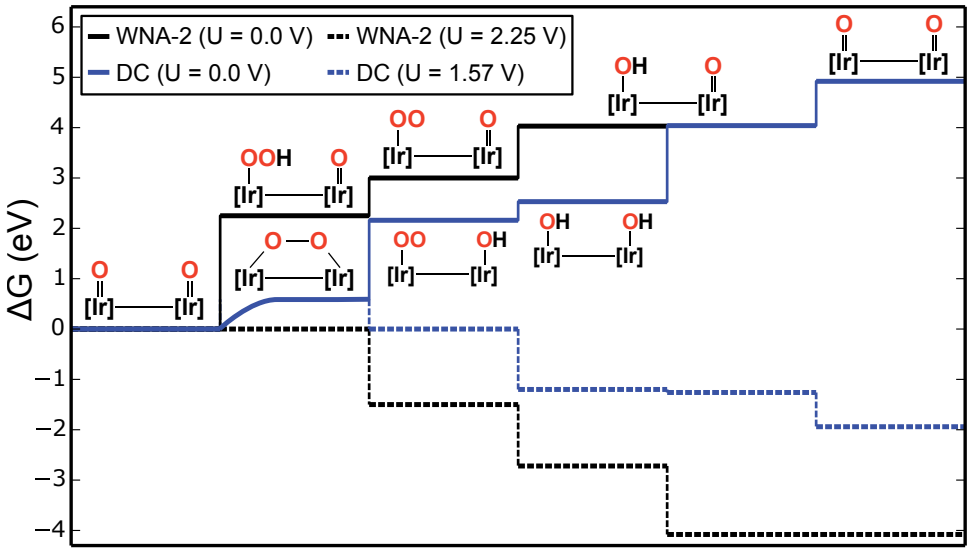


**Figure 5.11.** Gibbs energy diagram for the water oxidation reaction using the dimeric Ir complex as catalyst. The WNA-2 mechanism is indicated in black lines, while the DC is in blue lines. The blue curved line indicates that this is a chemical step.

### 5.3.3.3. Water Oxidation with the Ir-Hybrid Catalyst

Given that the Pourbaix diagram of the hybrid catalyst indicates the existence of two different active species in the range of typical water oxidation conditions (purple and gray regions in Figure 5.9), we examined the activity of both species, considering both the WNA and DC mechanisms for each of them. For the two species, we find the same lowest energy paths and potential limiting steps as for the dimeric Ir complex. In particular, for the hybrid system containing 7 hydrogen atoms, we found that all the electrochemical steps in the WNA-2 and DC mechanisms are downhill in energy at the potentials of 2.24 and 1.50 V, respectively. However, the DC mechanism is further hampered by the high chemical energy required to form the $\mu$-1,2-peroxo intermediate (0.98 eV).

In contrast, for the hybrid system with 6 hydrogen atoms, all the electrochemical steps in the WNA-2 and DC mechanisms become downhill at 2.18 and 1.76 V, respectively. In this case, we found that the formation energy for the $\mu$-1,2-peroxo intermediate is rather small (0.39 eV), and therefore, it may be surpassed even at room temperature. Based on this thermodynamic data, we predict that the DC mechanism for this species may

be more favorable than the WNA-2. Besides, the height of the chemical step and the overpotential for the WNA-2 mechanism for this species are lower than for the one containing 7 hydrogen atoms, which suggests that the hybrid system with 6 hydrogen atoms may be more representative for water oxidation activity with this hybrid catalyst (Figure 5.12).

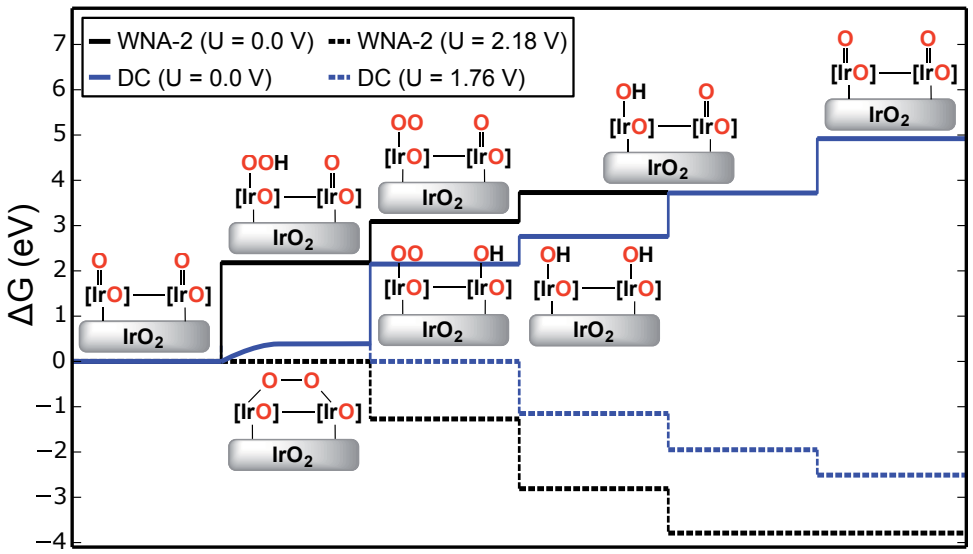


**Figure 5.12.** Gibbs energy diagram for the water oxidation reaction using the hybrid system as catalyst. The WNA-2 mechanism is indicated in black lines, while the DC is in blue lines. The blue curved line indicates that this is a chemical step.

Taken together, our results show that the intrinsic water oxidation activity, based on thermodynamics, of the different model Ir-based catalysts via a WNA-2 mechanism increases as follows: dimer ≈ hybrid < $IrO_2$. As regards to the DC mechanism, the comparison between the dimeric Ir complex and hybrid system is more complicated due to the concurrence of electrochemical and chemical reaction steps. Nevertheless, the fact that the dimeric Ir complex requires a slightly lower overpotential compared to the hybrid (0.34 V *versus* 0.53 V), but a higher chemical barrier (0.59 eV *versus* 0.39 eV), points out that these two catalysts might exhibit a comparable water oxidation activity. The comparison of the overall activity between the three model Ir-based catalysts is also rather complex, since the lowest energy-demanding pathway for both the dimeric Ir complex and the hybrid system

(DC) involves a chemical step, whereas for the $IrO_2$(110) surface does not (WNA-2). If we assume low energy barriers for the chemical steps with the dimeric Ir complex and the hybrid system, the activity trend is then dictated by the applied overpotential: dimer > $IrO_2$ > hybrid. Although this trend is not conclusive, the high activity predicted for the dimeric Ir complex would support that this species is part of the purple-blue solution, as suggested by Crabtree *et al.*[245] However, we note that the same authors also proposed that this species eventually forms $IrO_2$ nanoparticles, and thus it might not be very stable in aqueous solution.

### 5.3.4. Bader Charge Analysis

In order to understand the role of the surface in the hybrid system, we performed the Bader charge analyses presented in Figure 5.12.

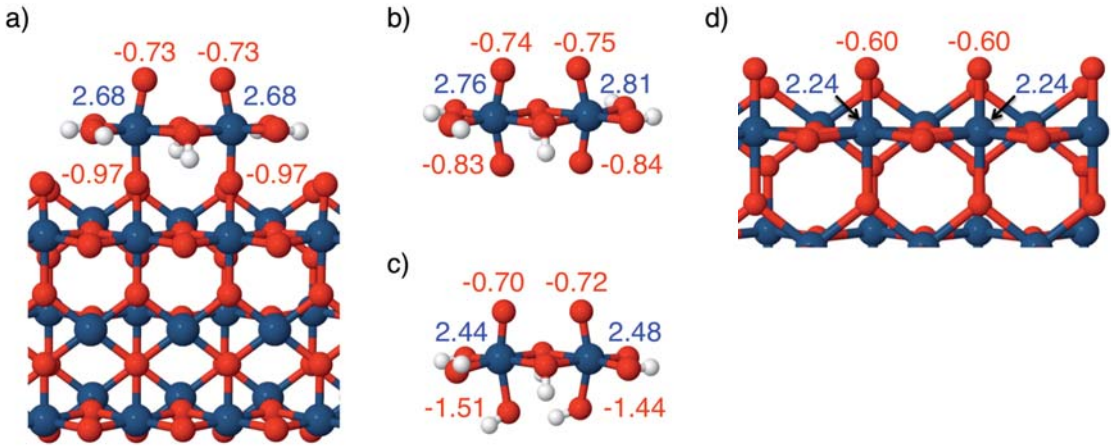


**Figure 5.12.** Selected calculated oxygen (red) and iridium (blue) Bader charges for the active species for the (a) hybrid system, (b and c) dimeric Ir complexes with oxo and hydroxo ligands on the bottom axial positions and (d) $IrO_2$(110) surface.

Interestingly, the electronic charge of the O atoms in the active species of the different Ir-based catalysts (top axial oxo-groups) increase in the order: $|q_{IrO2}| < |q_{hybrid}| \approx |q_{dimer}|$. This indicates that the oxo-moieties in the hybrid system and dimeric Ir complex are less electrophilic than in the $IrO_2$(110) surface. Consequently, oxo-groups in hybrid system and dimeric Ir complex are less reactive towards the nucleophilic attack of a water molecule,

which accounts for the predicted activity trend via the WNA-2 mechanism. In addition, we find that the charge of the Ir atoms of the active site varies within the different model catalysts, pointing to an increase in oxidation state as follows: $IrO_2$ < hybrid < dimer. This trend is tightly coupled to the electronic charge of the O atoms involved in the reaction. We also observed that the charge of the O-linkers of the hybrid system and the bottom oxo-moieties in the dimeric Ir complex (Figures 5.12a,b) are similar, thus suggesting that the former behave more similarly to oxo-ligands rather than hydroxo groups (Figures 5.12c). This can be ascribed to the additional charge donation provided by the $IrO_2$(110) surface to the O-linkers in the hybrid system.

## 5.4. Discussion and Conclusions

In this work, we employed Density Functional Theory calculations to evaluate the viability of a hybrid water oxidation catalyst generated by attaching a dimeric Ir complex to the $IrO_2$(110) surface. Calculations indicate that the interaction between the adsorbed catalyst and the surface is rather strong as a result of the electron donation from both Ir atoms in the anchored complex and the surface to the O linkers. The catalytic activity of the hybrid system was further assessed and compared to its constituent fragments. With the WNA mechanism, the activity of the considered systems is dimer ≈ hybrid < $IrO_2$. Assuming that the chemical barriers in the DC mechanism for the dimeric Ir complex and hybrid systems are feasible under water oxidation conditions, the catalytic activity may be governed by the applied potential, thus resulting in the following trend: dimer > $IrO_2$ > hybrid. The high activity of dimeric Ir complex shown in our calculations was consistent with the similar structures suggested to be involved in the formation of the purple-blue solution by Crabtree and co-workers.[245]

Taken together, results reported herein are encouraging as they indicate that hybrid catalysts are not only viable, but they might also benefit from the activity of homogeneous catalysts and the stability of heterogeneous ones. Importantly, calculations predict no significant activity loss when the dimeric Ir complex is anchored on the $IrO_2$(110) surface through O atoms. Thus, by attaching the dimeric Ir complex to an $IrO_2$(110) surface through O-linkers,

the stability of the homogeneous catalyst might be enhanced, as calculations show that this interaction is very strong. These findings are in line with very recent experimental work of a stable water oxidation catalyst based on a dimeric Ir complex anchored on a metal oxide surface.[33] Furthermore, this work suggests that the catalytic performance of the hybrid system can be enhanced by fine-tuning the ligands of the homogeneous constituent and the electronic properties of the heterogeneous constituent.

## Appendix

**Table A5.1:** Energy convergence test with a denser k-point grid for selected deprotonation reactions.

| Reaction | k-point sampling | ΔE (eV) |
|---|---|---|
| hyb-10H → hyb-9H + $H^+$ +$e^-$ | Γ-point | 1.38 |
| | 2x3x1 | 1.37 |
| hyb-10H → hyb-9H-2 + $H^+$ +$e^-$ | Γ-point | 1.81 |
| | 2x3x1 | 1.83 |
| hyb-9H → hyb-8H + $H^+$ +$e^-$ | Γ-point | 1.62 |
| | 2x3x1 | 1.64 |
| hyb-9H → hyb-8H-2 + $H^+$ +$e^-$ | Γ-point | 1.77 |
| | 2x3x1 | 1.79 |

A brief description of how the Pourbaix diagrams were constructed is provided. As mention above, in the case of the heterogeneous system, our reference structure corresponds to the clean $IrO_2$(110) surface. Given that we considered different H, OH and O coverages to determine the active species for the heterogeneous system, we calculated the change of the surface Gibbs energies ($\Delta G_{surf(i)}$) after different atoms ($G_{surf(i)}$) were adsorbed on the clean surface ($G_{surf(0)}$):

$$\Delta G_{surf(i)} = G_{surf(i)} - G_{surf(0)} + n_H\left(-\frac{1}{2}G_{H2} + U + \mathrm{k}\cdot pH\right) + n_O\left(-\frac{1}{2}G_{O2} - 2(U + k\cdot pH)\right) + n_{OH}\left(-G_{OH} - 1(U + \mathrm{k}\cdot pH)\right)$$

where $n_H$, $n_O$ and $n_{OH}$ are the number of H, O and OH groups adsorbed on the top of the surface and $\frac{1}{2}G_{H2}$, $\frac{1}{2}G_{O2}$ and $G_{OH}$ their corresponding Gibbs energies. The effect of the bias on all steps involving an electron is included by shifting the energy of these states by $-eU$, where $U$ is the electrode potential. The dependence on the $pH$ is accounted in the $k{\cdot}pH$ term, which comes from:

$$\Delta G(pH) = -k_B T \cdot \ln[H^+] = \underbrace{k_B T \cdot \ln 10}_{k} \cdot pH$$

On the other hand, for the dimeric Ir complex and the hybrid system we chose the species with the highest content of H atoms as reference ($G_{species(0)}$). From these species we proceeded by removing hydrogen atoms to obtain the different species ($G_{species(i)}$). Therefore, the change of Gibbs energies ($\Delta G_{species(i)}$) results in:

$$\Delta G_{species(i)} = G_{species(i)} - G_{species(0)} - n_H \left(-\frac{1}{2} G_{H2} + U + \mathrm{k} \cdot pH\right)$$

**Scheme A5.1:** Surface coverages considered in the Pourbaix Diagram for the $IrO_2(110)$ surface.

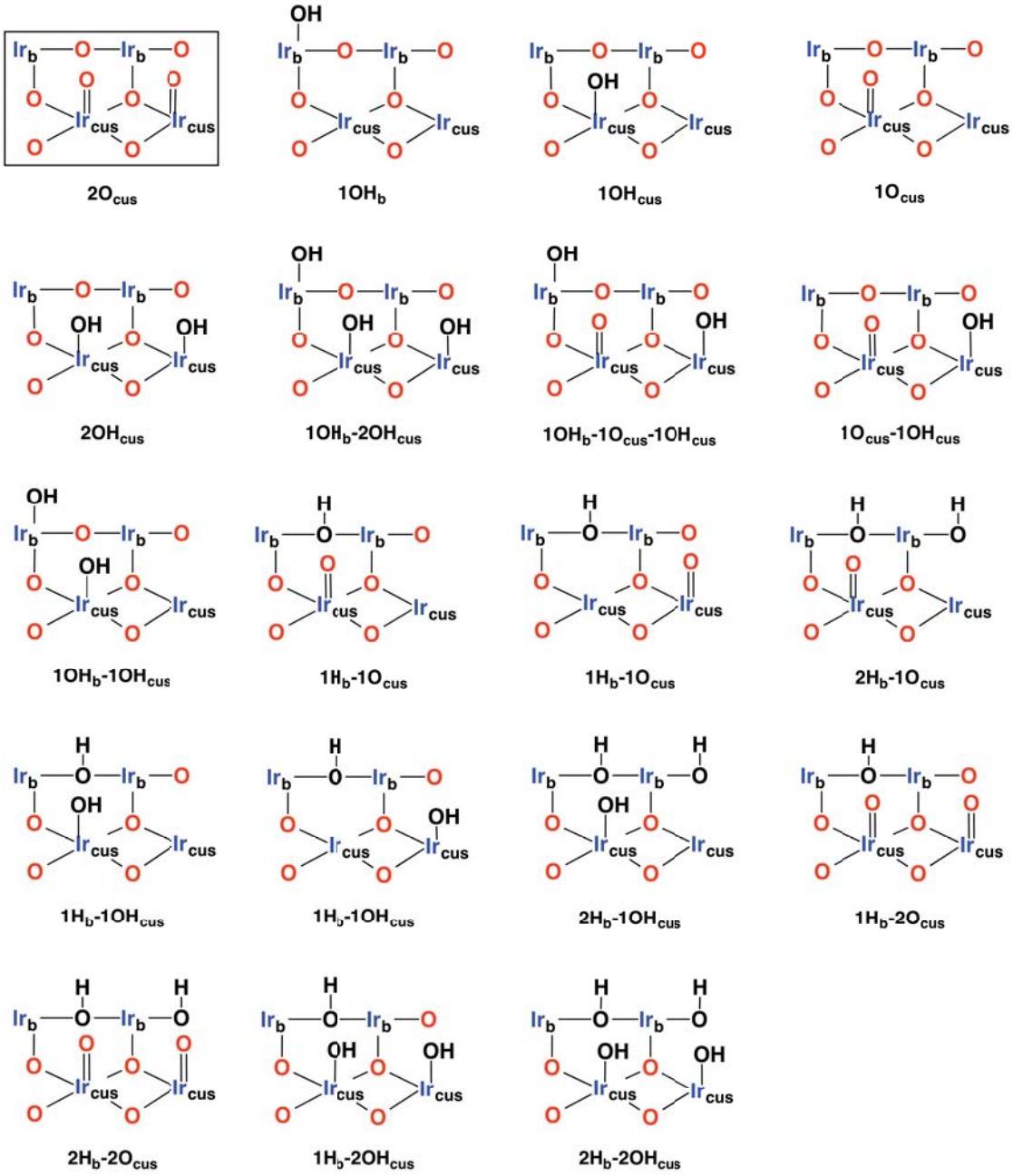

**Scheme A5.2:** Ir species with different protonation states considered in the Pourbaix diagram for the dimeric Ir complex. Solid rectangles indicate the most stable species for a given hydrogen content.

Dimeric species with 14H atoms:

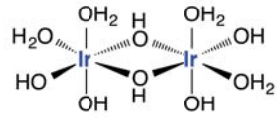

**hom-14H**

Dimeric species with 13H atoms:

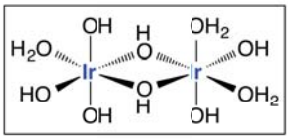

**hom-13H**

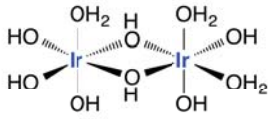

**hom-13H-2**

Dimeric species with 12H atoms:

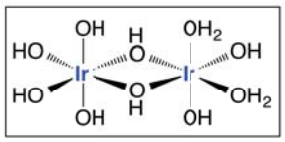

**hom-12H**

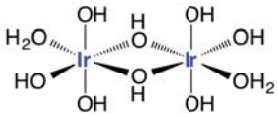

**hom-12H-2**

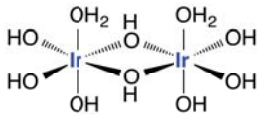

**hom-12H-3**

Dimeric species with 11H atoms:

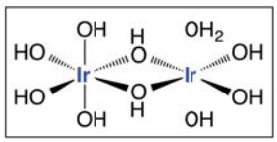

**hom-11H**

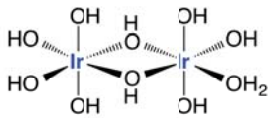

**hom-11H-2**

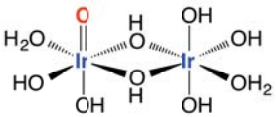

**hom-11H-3**

Dimeric species with 10H atoms:

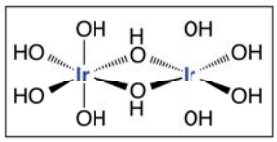

**hom-10H**

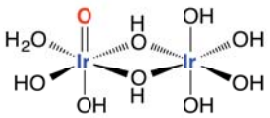

**hom-10H-2**

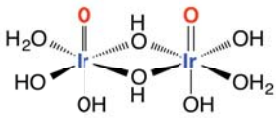

**hom-10H-3**

Dimeric species with 9H atoms:

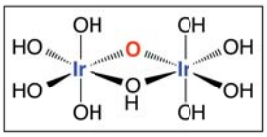
hom-9H

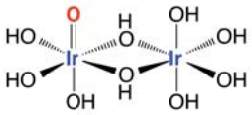
hom-9H-2

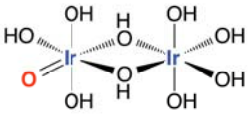
hom-9H-3

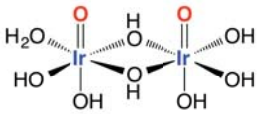
hom-9H-4

Dimeric species with 8H atoms:

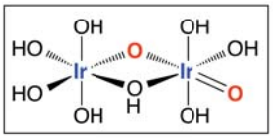
hom-8H

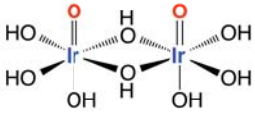
hom-8H-2

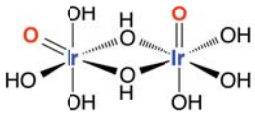
hom-8H-3

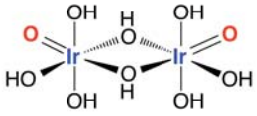
hom-8H-4

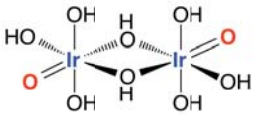
hom-8H-5

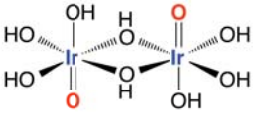
hom-8H-6

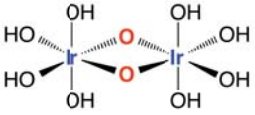
hom-8H-7

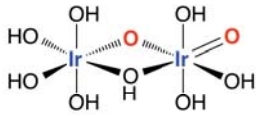
hom-8H-8

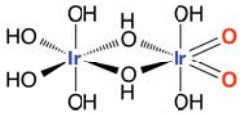
hom-8H-9

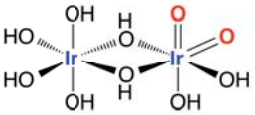
hom-8H-10

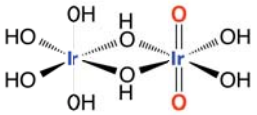
hom-8H-11

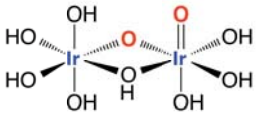
hom-8H-12

Dimeric species with 7H atoms:

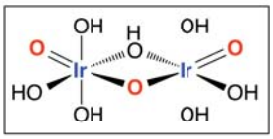
hom-7H

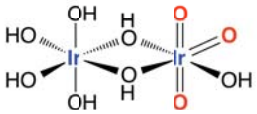
hom-7H-2

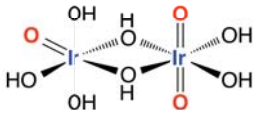
hom-7H-3

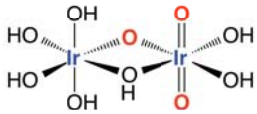
hom-7H-4

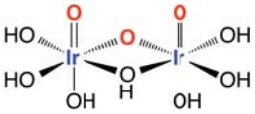
hom-7H-5

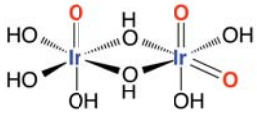
hom-7H-6

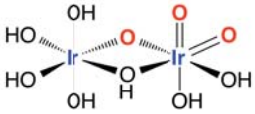
hom-7H-7

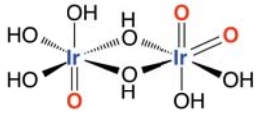
hom-7H-8

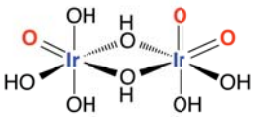
hom-7H-9

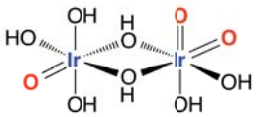
hom-7H-10

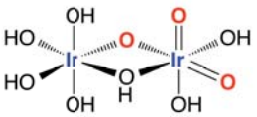
hom-7H-11

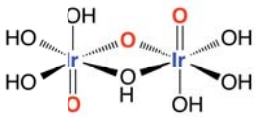
hom-7H-12

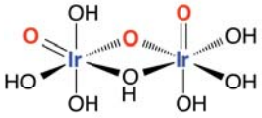
hom-7H-13

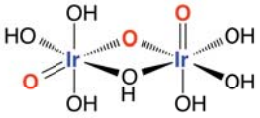
hom-7H-14

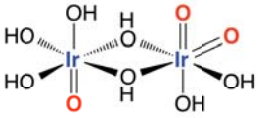
hom-7H-15

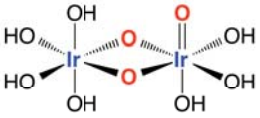
hom-7H-16


hom-7H-17

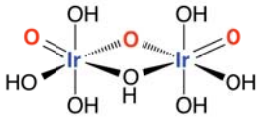
hom-7H-18

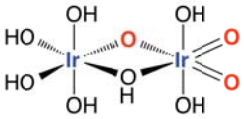
hom-7H-19

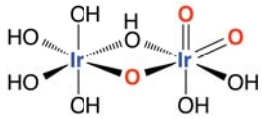
hom-7H-20

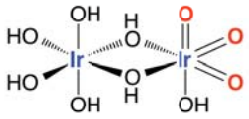
hom-7H-21

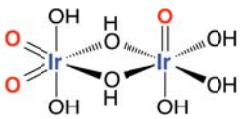
hom-7H-22

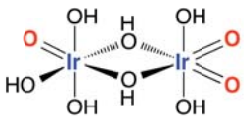
hom-7H-23

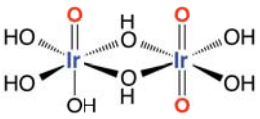
hom-7H-24

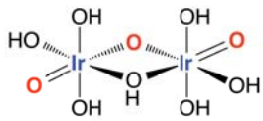
hom-7H-25

Dimeric species with 6H atoms

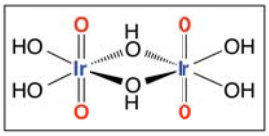
hom-6H

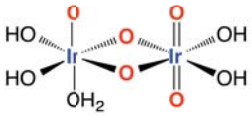
hom-6H-2

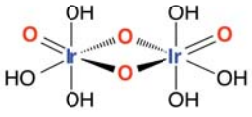
hom-6H-3

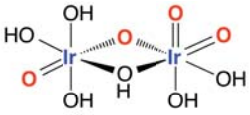
hom-6H-4

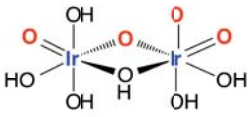
hom-6H-5

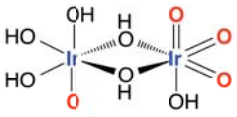
hom-6H-6

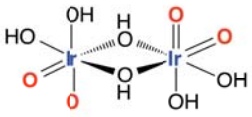
hom-6H-7

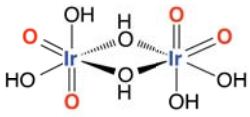
hom-6H-8

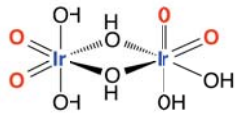
hom-6H-9

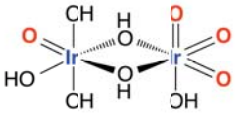
hom-6H-10

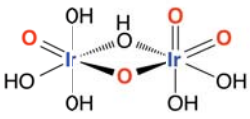
hom-6H-11

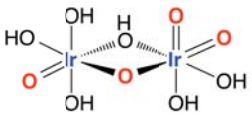
hom-6H-12

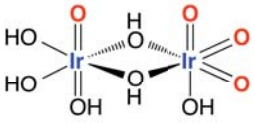

hom-6H-46

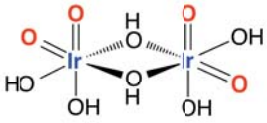

hom-6H-47

**Scheme A5.3:** Ir species with different protonation states considered in the Pourbaix diagram for the hybrid Ir system. Solid rectangles indicate the most stable species for a given hydrogen content.

Hybrid species with 12H atoms:

hyb-12H

Hybrid species with 11H atoms:

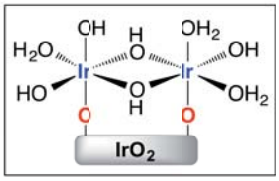

hyb-11H

hyb-11H-2

Hybrid species with 10H atoms:

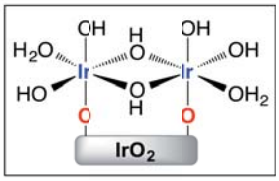

hyb-10H

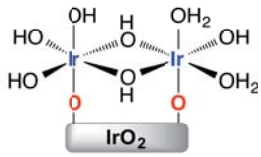

hyb-10H-2

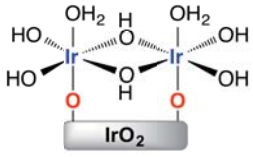

hyb-10H-3

Hybrid species with 9H atoms:

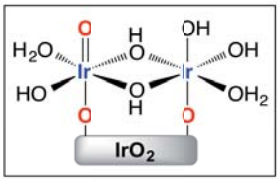

hyb-9H

hyb-9H-2

hyb-9H-3

Hybrid species with 8H atoms:

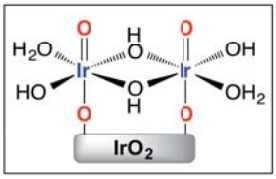


hyb-8H


hyb-8H-2


hyb-8H-3


hyb-8H-4

Hybrid species with 7H atoms:

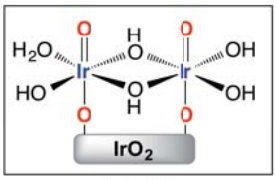


hyb-7H

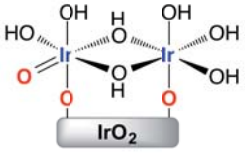


hyb-7H-2


hyb-7H-3

Hybrid species with 6H atoms:

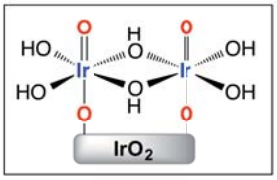


hyb-6H


hyb-6H-2


hyb-6H-3


hyb-6H-4

**Scheme A5.4:** Gibbs reaction energies (in eV) for the WNA and DC mechanisms explored for the dimeric Ir complex (values in parenthesis) and hybrid catalysts. Dashed and solid arrows indicate electrochemical and chemical reaction steps, respectively. The oxygen linkers, $O_l$, in the homogeneous catalyst correspond to OH groups

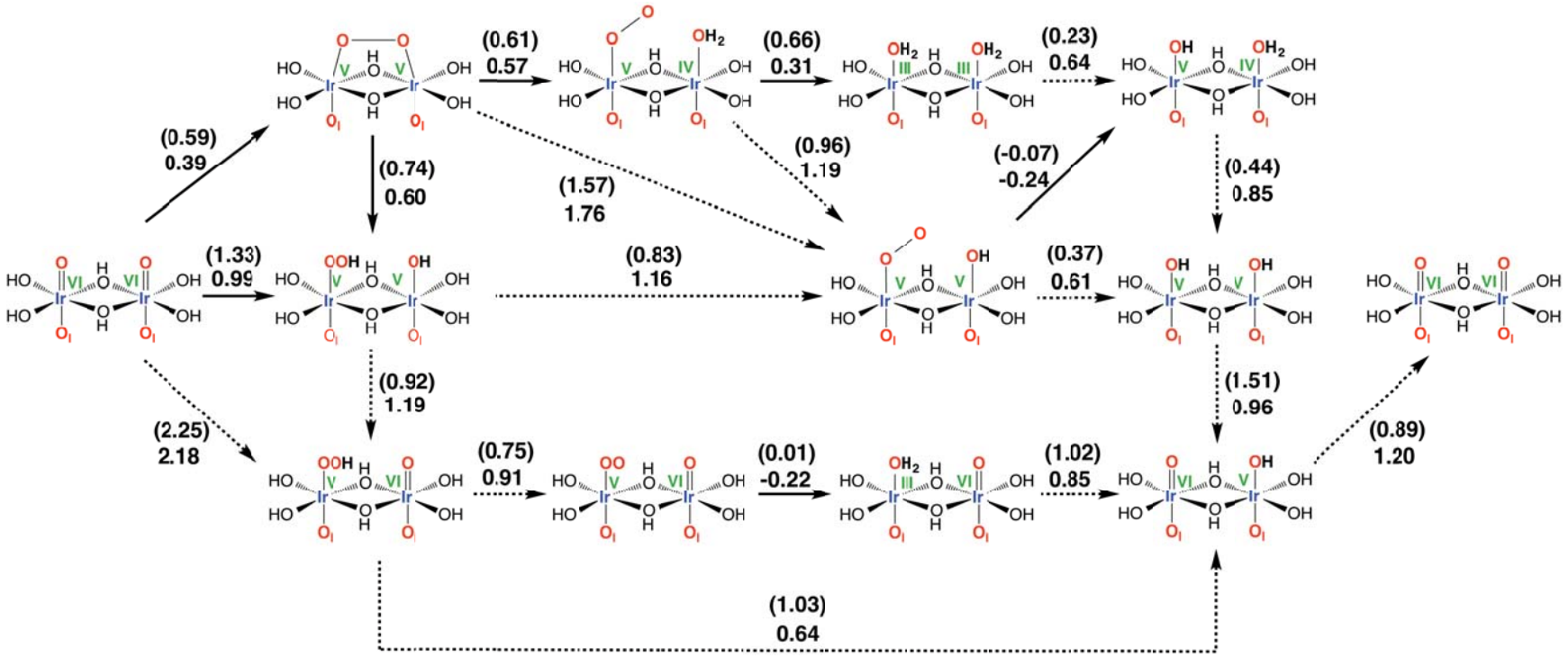

*"La gota horada la piedra, no por su fuerza, sino por su constancia."*

Publio Ovidio

# 6

# *Rhodium- and Iridium-Mediated Alkene Oxidation with $O_2$*

In this chapter a mechanistic study of the metal-promoted olefin-oxidation reaction, using $O_2$ as oxidant, has been performed with the aim to compare a rhodium and an iridium complexes and to provide a mechanistic explanation justifying the different products obtained experimentally. Specifically, this study focuses on the oxygenation of 1,5-cyclooctadiene (cod) directly coordinated to the metal center in the [Ir(PhN=C(NMe$_2$)NPh)(cod)] and the [Rh(PhN$_3$Ph)(cod)] complexes.

## 6.1. Introduction

Oxygenation of C–C double bonds mediated by transition metal complexes is a powerful synthetic strategy to convert hydrocarbon feedstocks into high added-value chemicals such as ketones, epoxides or aldehydes.[86,90,260,261] Ideally, molecular oxygen would be the most desirable oxidant agent to employ in these reactions, as it is an environmentally friendly, abundant and economical reagent. However, oxidation reactions with $O_2$ are significantly more difficult to control, which makes its use still challenging.

In industry, the C–O functionalization of alkenes is typically carried out with Pd[262,263] and Ag-based[86,264,265] complexes, although a number of Rh and Ir compounds have been also proven to accomplish this reaction (even with $O_2$).[88,90,266] With these latter metals and the appropriate choice of ligands, two main types of reaction intermediates have been experimentally characterized depending on the reaction conditions employed, namely metalla-oxetanes[97,100,267] and metalladioxolanes.[95,96] The oxidation of olefins using peroxides and protic solvents often favors the formation of metallaoxetanes (Scheme 6.1a), while molecular oxygen and aprotic solvents tend to produce metalladioxolanes (Scheme 6.1b). An exception to this behavior, however, is the dinuclear 2-metallaoxetane compound synthesized by Tejel and co-workers[87] from $O_2$ and the complex [Rh(PhN$_3$Ph)(cod)] in toluene (Scheme 6.2a). This particular system has further the advantage of using the two oxygen atoms in $O_2$ for the oxidation of two cod ligands, thus optimizing the overall atom economy.

**Scheme 6.1:** General structures for: a) Metallaoxetane and b) Metalla-dioxolane.

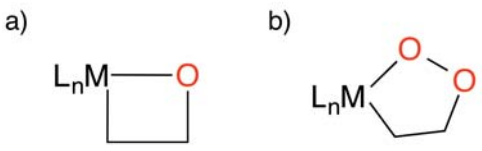


Generally, the oxidation of olefins involves open-shell and unstable intermediates, which are difficult to isolate and characterize. As a result, the mechanistic details on how dioxygen binds to the transition metal complex

and how the subsequent C–O bond formation takes place are rather scarce. However, valuable insight into the reaction mechanism was recently provided by Rohde *et al.*[89] with the identification and characterization of the peroxo intermediate [Ir(PhN=C(NMe$_2$)NPh)(cod)(O$_2$)], which finally affords 4-cycloocten-1-one (Scheme 6.2b). It is remarkable the different evolution of the rhodium and iridium complexes, despite they bear a similar ligand framework. This behavior is investigated in this chapter.

**Scheme 6.2:** Reported oxidation reactions of the cod ligand in the [Rh(PhN$_3$Ph)(cod)] and [Ir(PhN=C(NMe$_2$)NPh)(cod)] complexes.

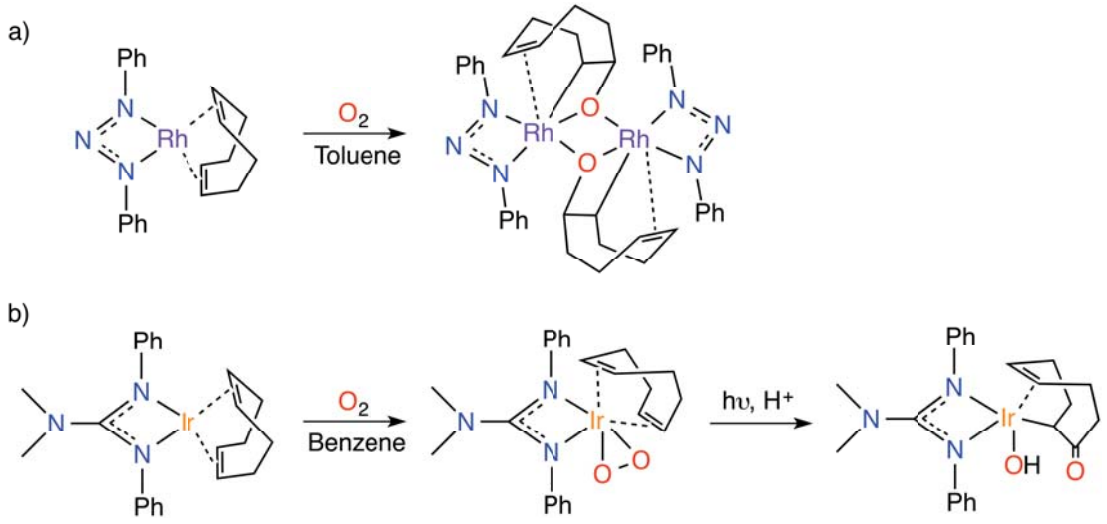


## 6.2. Computational Details

All the calculations presented in this work were carried out in Gaussian09 program[224] by means of the Density Functional Theory (DFT) using the MPWB1K exchange correlation functional. This functional was chosen based on the good results shown by Zhao and Truhlar[184] in thermochemistry, kinetics and noncovalent interactions. Moreover, Borden *et al.* [187] performed a comparative study between a MPW functional and B3LPY, which indicates that the MPW functional is also more suitable for calculations on hydrogen abstraction reactions, such as hydrogen-atom transfer and proton-coupled electron transfer (PCET). In agreement with this, Sodupe and Rodriguez-Santiago studied a series of Cu–H$_2$O complexes with several DFT functionals being BHandHLYP and MPWB1K the ones that better described open-shell hydrogen-transfer reactions.[160,185]

To describe the H, C, N and O atoms, the triple-ζ 6-311G(d,p) basis set was employed, while for the Rh and Ir metal atoms the effective core potential LANL2TZ(f)[268–270] basis set was used. Geometry optimizations were performed in the gas phase without imposing any geometry or symmetry constraints. The nature of all the stationary points was further verified through frequency calculations. Furthermore, for transition states, intrinsic reaction coordinate (IRC) calculations were carried out to verify that they connect the corresponding reaction minima.

Solvent effects were introduced using the experimental solvent employed (iridium complexes: benzene (Ɛ = 2.27); rhodium complexes: toluene (Ɛ = 2.38) through single point calculations on the above gas-phase optimized geometries using the SMD solvation model.[203] In this way absolute energies in solution ($E_{sol}$) were computed using an extended triple-ζ 6-311++G(d,p) basis set for the H, C, N and O atoms. These $E_{sol}$ were transformed into $G_{sol}$ (Gibbs energies in solution) by means of:

$$G_{sol} = E_{sol} + ZPE + H_{vib} + 6k_bT - TS_{mod} \quad [6.1]$$

where $H_{vib}$ is the vibrational enthalpy, $ZPE$ is the zero point energy, and $S_{mod}$ is the entropy calculated as proposed by Ziegler *et al.*[271,272] by using the Wertz's approximation.[211] The latter term $S_{mod}$ is defined as:

$$S_{mod} = S_{elec} + S_{vib} + 0.54(S_{trans} + S_{rot}) + 0.24 \quad [6.2]$$

with $S_{elec}$, $S_{vib}$, $S_{trans}$, and $S_{rot}$ being the electronic, vibrational, translational and rotational contributions to the entropy, respectively.

In order to change the standard state from the gas phase (1 atm) to solution (1M) a correction of 1.90 kcal·mol$^{-1}$ was applied to all G values. This implies that $\Delta G_{sol}$ values were corrected by 1.90 kcal·mol$^{-1}$ when one species is generated from two, i.e. one equivalent of transition metal complex and molecular oxygen, and by 3,80 kcal·mol$^{-1}$ when it is formed by three, i.e. 2 equivalents of transition metal complex and one of molecular oxygen.[273,274] Therefore, all the energies reported throughout this work correspond to Gibbs energies in solution ($G_{sol}$) at the temperature of 298.15 K and 1 M.

Since the reactions start with a singlet transition metal complex and

triplet $O_2$ and end up with singlet products, the triplet (T) and singlet (S) potential energy surfaces, as well as the open-shell singlet (OS) have been explored. It is important to note that in open-shell singlet diradicals, the spin density is often contaminated by higher spin states, especially by the triplet state. In order to take into account this spin contamination all stationary points with an open-shell singlet spin states were further corrected following the approach of Yamaguchi :[275,276]

$$^1E_{sc} = {}^1E + f_{sc}\left({}^1E - {}^3E\right) \qquad [6.3]$$

where $^1E_{sc}$ corresponds to the corrected open-shell singlet energy, $^1E$ and $^3E$ are the calculated energies of the open-shell singlet and triplet states and $f_{sc}$ accounts for the fraction of spin contamination and is defined as:

$$f_{sc} = \frac{^1\langle S^2\rangle}{^3\langle S^2\rangle - {}^1\langle S^2\rangle} \qquad [6.4]$$

where $S^2$ denotes the total spin angular momentum operator.

To locate the minimum energy crossing points (MECPs) between potential energy surfaces of different spin, the program developed by the group of Harvey was employed.[199] To confirm the nature of the stationary points connected to the MECPs, the latter is fully optimized in the two spin states involved in the crossing. The Gibbs energies in solution of the MECPs were estimated by adding the contributions to the Gibbs and solvation energies of the previous intermediate to the calculated potential energies of the MECPs.

Natural bond orbital (NBO) calculations have been performed with the program NBO 6.0.[277]

## 6.3. Results

### 6.3.1. Reaction Mechanisms

This section presents a mechanistic study on the selective oxidation reactions shown in Scheme 6.2, which lead to completely different products despite of the similarities between the two transition metal complexes. For each reaction, we provide a detailed description of the operating mechanism

through the study of the closed-shell singlet (S), open-shell singlet (OS) and triplet (T) spin states. The factors that make so different the reactivity with these two compounds will be also discussed.

#### 6.3.1.1. Oxidation with the [Rh(PhN$_3$Ph)(cod)] complex

In the previous work reported by Tejel and co-workers,[87] the authors proposed a reaction mechanism based on the obtained kinetic data and experimental observations. This mechanism starts with the initial coordination of dioxygen to the [Rh(PhN$_3$Ph)(cod)] complex, which they attributed to the rate-determining step, followed by the attack of a second Rh unit that leads to O–O bond cleavage. In order to get a deeper insight into the reaction mechanism, we carried out a detailed computational study involving different potential spin energy surfaces.

The mechanism proposed herein starts with the coordination of molecular oxygen to Rh in an end-on ($\eta^1$) binding mode. This step is feasible from the kinetic point of view in the triplet spin state with an energy barrier of 11.2 kcal·mol$^{-1}$, **T-TS1,** whereas it is highly demanding in close and open singlet spin states (Figure 6.1). Additionally, the formation of the resulting adduct is less endoergic ($\Delta G_{sol}$ = 10.0 kcal·mol$^{-1}$) in the triplet state, **T-I2**, than in the other spin states. The O–O and Rh–O bond distances in the **T-I2** intermediate are 1.251 and 2.084 Å, respectively, which are very similar to those reported in previous works for $\eta^1$-superoxo ligands.[278,279] Therefore, this superoxo species still maintains the triplet ground spin state of $O_2$ with spin densities localized at the Rh and both O atoms. The spin densities and the natural atomic orbital occupancies indicate that the $O_2$ has been reduced by one electron via charge transfer from the metal center to the dioxygen moiety (see next section for a more detailed spin density analysis). Thus, the complex resulting from the $O_2$ coordination step can be described as a Rh(II)-superoxo species with two unpaired electrons in the rhodium and $O_2$ fragments.

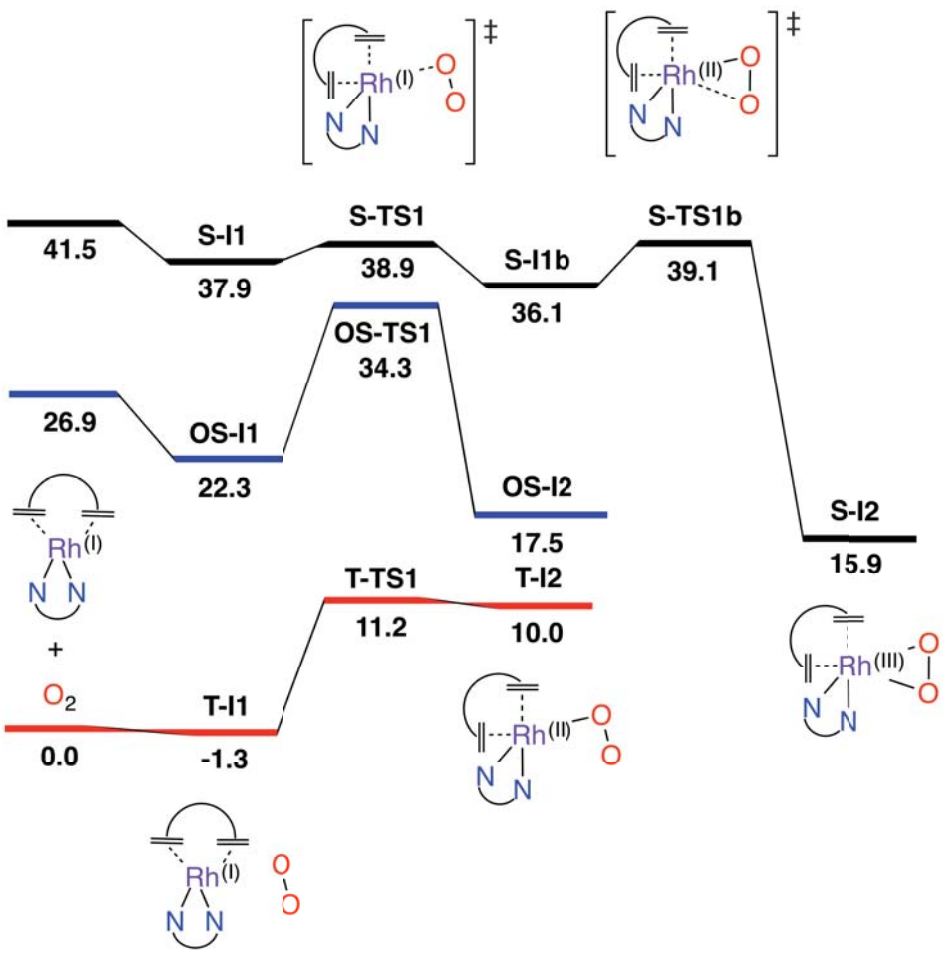


**Figure 6.1.** Gibbs energy profile in toluene, in kcal·mol$^{-1}$, for the coordination of $O_2$ [Rh(PhN$_3$Ph)(cod)]. The different spin states of the stationary points are depicted in red (T), blue (OS) and black (S).

To further reduce the O–O bond, another electron needs to be transferred either from the same metal center or from another complex unit. In this case, our calculations showed that the second electron is more likely to be transferred from a second metal center, as the monomeric Rh(III) peroxo singlet species (**S-I2**) was higher in energy than the dimeric one **T-I3** (15.9 *vs.* 8.2 kcal·mol$^{-1}$, see Figures 6.1 and 6.2). From this point, the lowest energy pathway to trigger the alkene oxidation involves triplet spin-crossover from **T-I3** to **OS-I3** from a triplet to an open-shell singlet spin states, respectively. This spin-crossover takes place through **MECP1**, which lies 16.7 kcal·mol$^{-1}$ above the separated reactants. The **OS-I3** intermediate has almost the same geometric structure than **T-I3** but differs in the inversed spin located in the

Rh atom. The reaction then proceeds via formation of two new Rh–O bonds leading to a $\mu$-$\eta^2$:$\eta^2$-peroxo planar structure **OS-I4** with a low energy barrier of 18.2 kcal·mol$^{-1}$ (**OS-TS3**). The intermediate **OS-I4** exhibits two interesting features: the two metal centers are oxidized in one unit, which is reflected in a stretched O–O bond distance of 1.423 Å, and the two unpaired electrons are localized in both Rh atoms in an antiferromagnetic fashion. Once **OS-I4** is formed, the O–O bond cleavage occurs through the transition state **OS-TS4** (Figure 6.3) with an overall Gibbs energy barrier of 31.0 kcal·mol$^{-1}$. It is important to note that the spin density in this transition state is equally distributed between both Rh and both O atoms; more specifically the Rh atoms are coupled antiferromagnetically in the same way as the O atoms. The relaxation of **OS-TS4** towards products by means of the IRC method leads to the closed-singlet (**S-I5**), where the O–O bond is completely broken (d(O–O) = 2.552 Å). Finally, the partial oxidation of the two cod ligands takes place in two sequential steps with low energy barriers of 9.3 (**S-TS5**) and 7.4 kcal·mol$^{-1}$ (**S-TS6**), respectively.

It is noteworthy to mention that most of these dimetallic dioxygenated species have been extensively investigated by Solomon *et al.*[280] and Tolman *et al.*[281], with Cu as metal center. These $Cu_2O_2$ motifs are particularly important because they are contained in proteins that bind and/or activate dioxygen performing a variety of critical biological functions, such as $O_2$ transport (hemocyanin) and aromatic ring oxidations (tyrosinase).

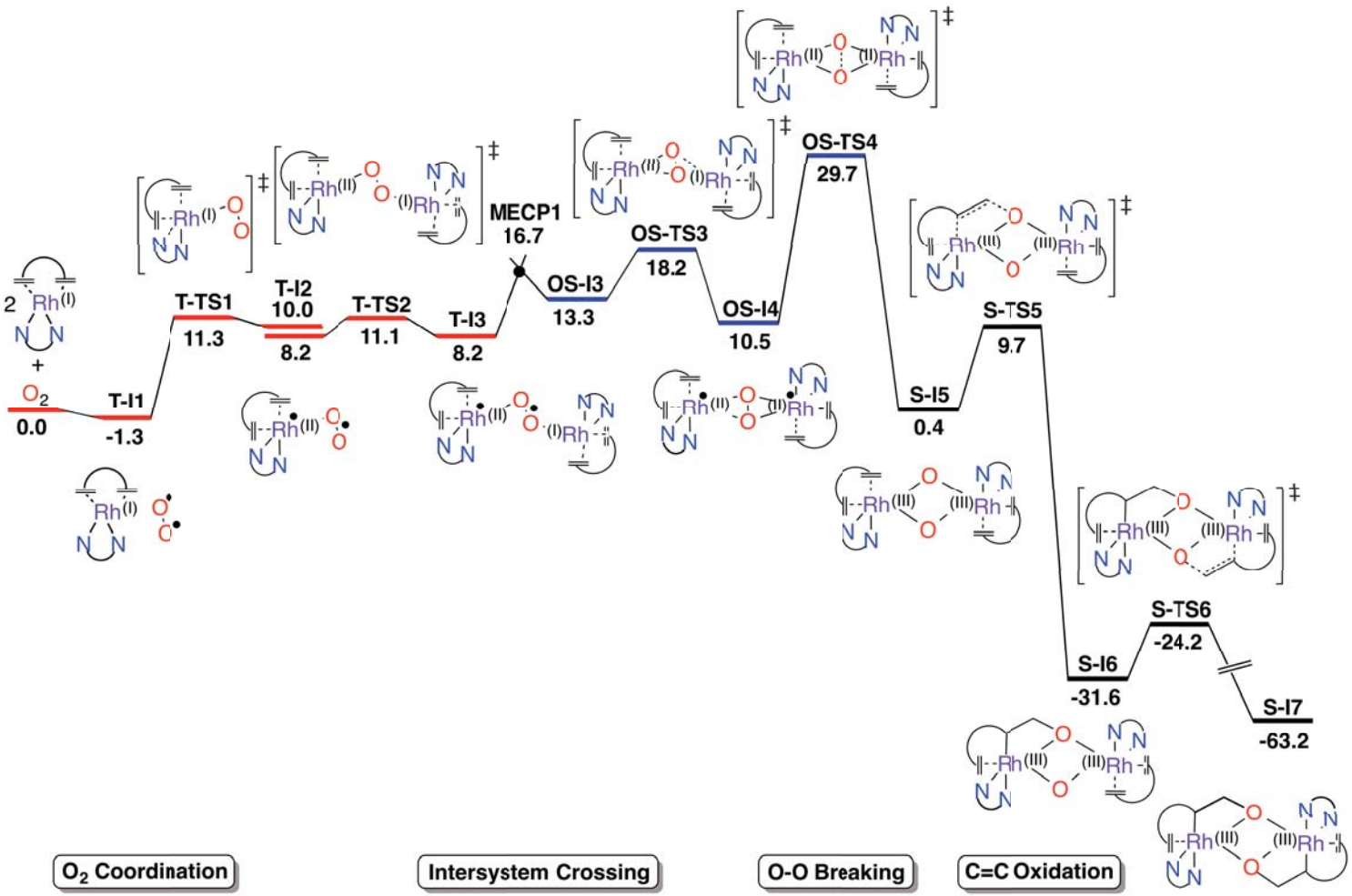


**Figure 6.2:** Lowest Gibbs energy profile in toluene, in kcal·mol$^{-1}$, for the oxidation of cod by $O_2$ in [Rh(PhN$_3$Ph)(cod)]. The different spin state of the stationary points is depicted in red (T), blue (OS) and black (S). For entire pathways on each spin state see Figure A6.1

Overall, according to the Gibbs energy profile shown in Figure 6.2, the oxidation of two cod units in [Rh(PhN$_3$Ph)(cod)] is an exoergic process by -63.2 kcal·mol$^{-1}$. The most energy-demanding step in this reaction corresponds to the O–O bond cleavage, **OS-TS4** (Figure 6.3), with an energy barrier of 31.0 kcal·mol$^{-1}$ with respect to **T-I1**, which it is even higher in the triplet and closed singlet potential energy surfaces (36.3 and 47.1 kcal·mol$^{-1}$ for the triplet and closed-shell singlet, respectively, see Figure A6.1).

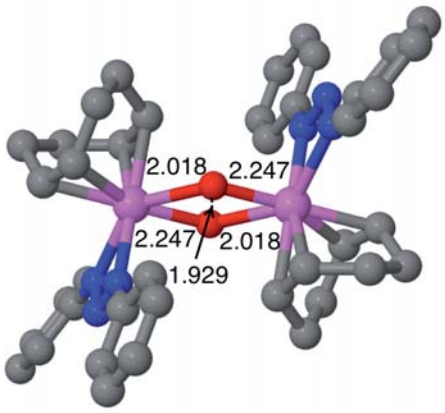


**Figure 6.3:** Optimized geometry of **OS-TS4**. Color code: purple = Rh, blue =N, red = O, gray = C. The H atoms are removed for clarity. Selected bond distances for all the other species involved in the reaction pathway are shown in the Appendix (Table A6.1).

Additionally, in order to discard the possible oxidation of cod via a monomeric species, we also explored the formation of the metalladioxolane product (Figure 6.4). Calculations revealed that the C–O bond formation process is more energy demanding in both the triplet (51.2 kcal·mol$^{-1}$) and the singlet (34.3 kcal·mol$^{-1}$) spin states than for the dimerization mechanism (31.0 kcal·mol$^{-1}$).

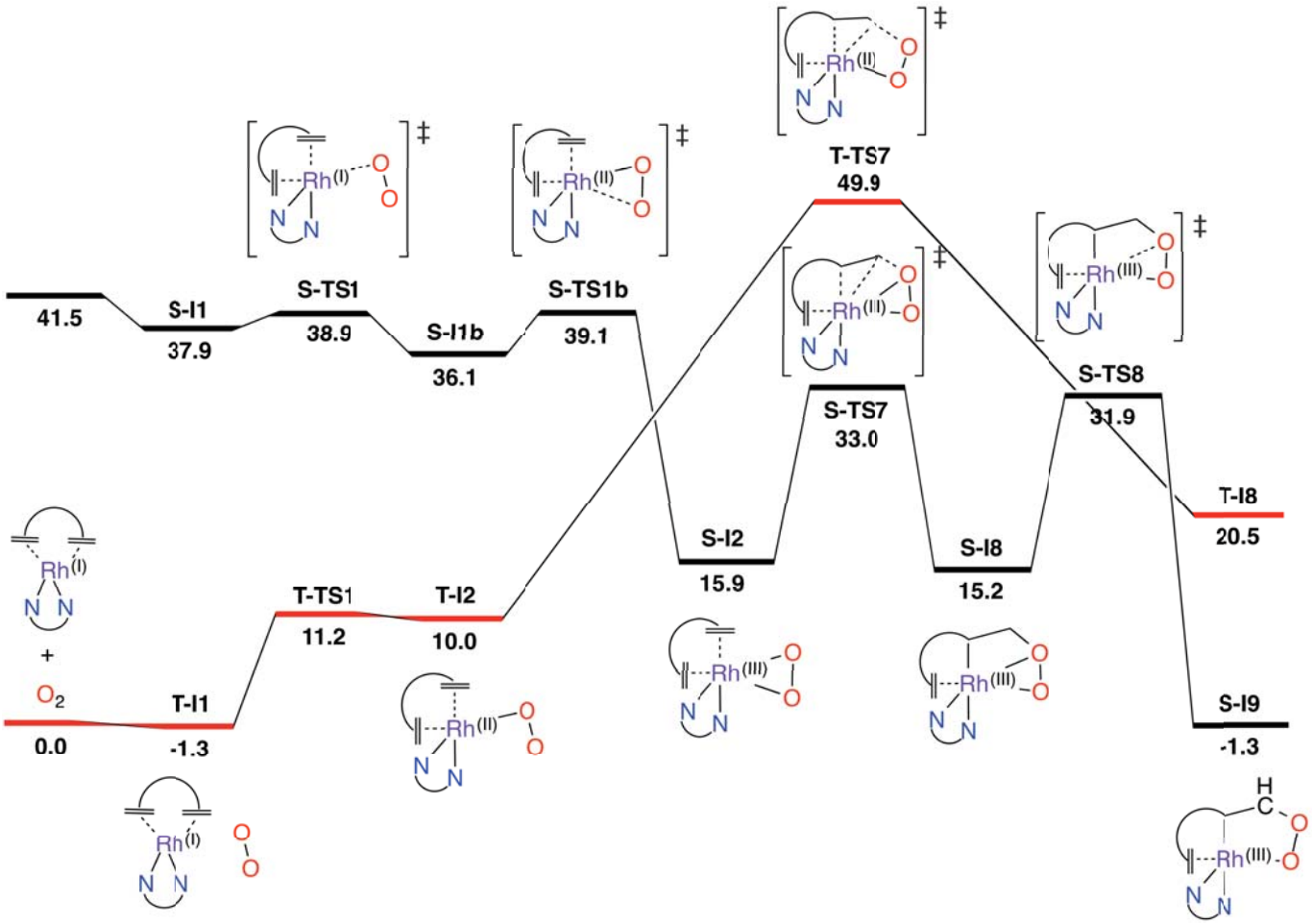


**Figure 6.4.** Gibbs energy profile in toluene, in kcal·mol$^{-1}$, for the formation of metalladioxolane from [Rh(PhN$_3$Ph)(cod)] and $O_2$. The spin states of the stationary points are depicted in red (T) and black (S).

#### 6.3.1.2. Spin Density Analysis

To gain insight into the change in the spin states along the lowest energy oxidation pathway (Figure 6.3), we plot in Scheme 6.3 the spin densities at the Rh and O atoms for the different reaction intermediates and the **OS-TS4**. Initially, the two unpaired electrons in **T-I1** are perfectly localized at the $O_2$ molecule in a ferromagnetic arrangement (Table 6.1). Then, the $Rh_1$ atom and $O_2$ interact in **T-I2** leading to oxidation of the metal center to a formal Rh(II), as reflected in the appearance of some spin density at this atom. Interestingly, this species is still a triplet in its ground state, and all the spin density is distributed within the $Rh_1–O_2^-$ superoxo moiety. From **T-I2**, the coordination of a second Rh complex to the superoxo adduct takes place giving rise to **T-I3**. In this case, we find that there is no spin density located at the $Rh_2$ atom, which indicates that this metal center still maintains its initial oxidation state of +1. The reaction then proceeds by spin-crossover from the triplet (**T-I3**) to the open shell singlet (**OS-I3**) species, which entails a spin inversion on the $Rh_1$ atom. In the next step, the formation of the $Rh_2–O_1$ bond results in the oxidation of the $Rh_2$ atom to Rh(II), as reveals the spin density located at this atom in **OS-I4**. Finally, this intermediate evolves to the product **S-I5** via **OS-TS4**. In this transition state the O–O bond is stretched and the electrons involved in this bond are transferred to each O atoms with opposite spins. As can be observed in Table 6.1, the spin density in **OS-TS4** is equally distributed between both Rh and both O atoms, more specifically Rh atoms are coupled antiferromagnetically as the same way as O atoms. The relaxation of this transition state finally leads to the close shell **S-I5** intermediate, where both Rh(II) are oxidized to Rh(III).

**Scheme 6.3:** Representation spin densities (ρ), in a.u., on the Rh and O atoms, for the most stable intermediates and the **OS-TS4** involved in the reaction pathway using the [Rh(PhN$_3$Ph)(cod)] complex.

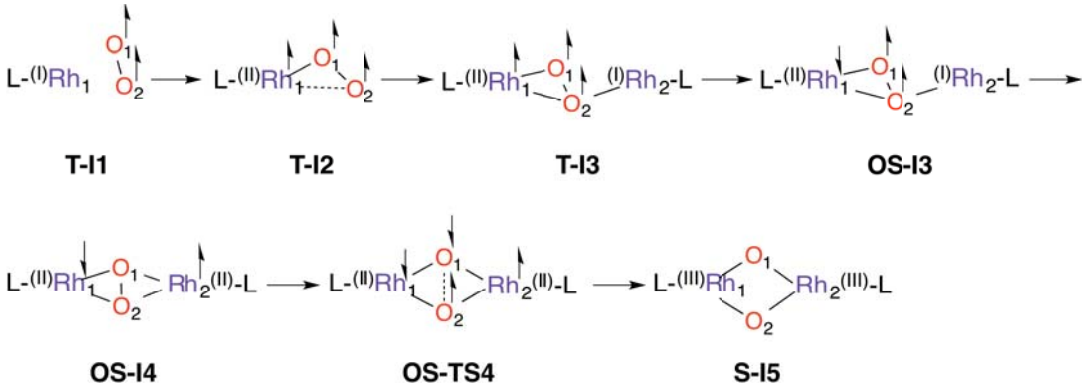


**Table 6.1:** Spin densities (ρ), in a.u., on the Rh and O atoms, for the most stable intermediates and the **OS-TS4** involved in the reaction pathway using the [Rh(PhN$_3$Ph)(cod)] complex.

| Species | ρ(Rh$_1$) | ρ(O$_1$) | ρ(O$_2$) | ρ(Rh$_2$) |
|---|---|---|---|---|
| **T-I1** | 0.00 | 1.01 | 0.99 | - |
| **T-I2** | 0.51 | 0.66 | 0.79 | - |
| **T-I3** | 0.71 | 0.58 | 0.57 | 0.01 |
| **OS-I3** | -0.75 | 0.44 | 0.46 | 0.01 |
| **OS-I4** | -0.71 | 0.00 | 0.00 | 0.71 |
| **OS-TS4** | -0.69 | -0.69 | 0.69 | 0.69 |
| **S-I5** | 0.00 | 0.00 | 0.00 | 0.00 |

### 6.3.1.3. Oxidation with the [Ir(PhN=C(NMe$_2$)NPh)(cod)] complex

Unlike the above [Rh(PhN$_3$Ph)(cod)] compound, the similar complex [Ir(PhN=C(NMe$_2$)NPh)(cod)] reported by Rohde *et al.*,[89] yields an oxidized monomeric species in the presence of $O_2$ (Scheme 6.1).

As previously described, the reaction starts with the coordination of molecular oxygen to the metal center, although in this case the transition state associated to this step (**T-TS1'**) requires a higher energy barrier of 16.0 kcal·mol$^{-1}$ (Figure 6.6). The relaxation of the transition state towards the products-side of the reaction leads to the formation of the Ir(II) superoxo

species, **T-I2'.** In the same way as the [Rh(PhN$_3$Ph)(cod)] complex, the coordination of molecular oxygen in a $\eta^1$-fashion is more favored in the triplet spin state than in closed and open-shell spin states. Moreover, the natural spin densities of this superoxo intermediate are also delocalized between both O atoms and Ir. Nevertheless, in the present case the closed-shell Ir(III) singlet peroxo adduct **(S-I2'),** in which both oxygen atoms are coordinated to the Ir metal center, becomes 9.7 kcal·mol$^{-1}$ even more stable than the superoxo **T-I2'** intermediate. In order to connect these two intermediates the reaction undergoes though a spin crossover, **MECP1',** from the triplet to the closed-shell singlet spin state, which lies 15.3 kcal·mol$^{-1}$ above separated reactants. Thus, in the iridium system the crossing between the triplet and singlet surfaces happens at the oxygen coordination step because the singlet $\eta^2$-peroxo species is more stable than the triplet $\eta^1$-superoxo compound. This is in agreement with the experimental results reported by Rohde, since the peroxo adduct was identified as an intermediate of the reaction, in spite of its limited stability, and characterized by spectroscopic methods.

It is worth mentioning that the O–O moiety in the peroxo species **S-I2'** is bound to Ir in a side-on ($\eta^2$) fashion and that it has been reduced in two units by a unique metal center. From **T-I2'** to the **S-I2'**, the O–O bond distance increases from 1.270 to 1.383 Å, while the Ir–O distance is reduced from 2.075 to 1.976 Å. This supports the observation that the O–O and Ir–O bond orders are inversely correlated, so that the $O_2$ reduction is accompanied by a higher metal-oxygen covalency.[282]

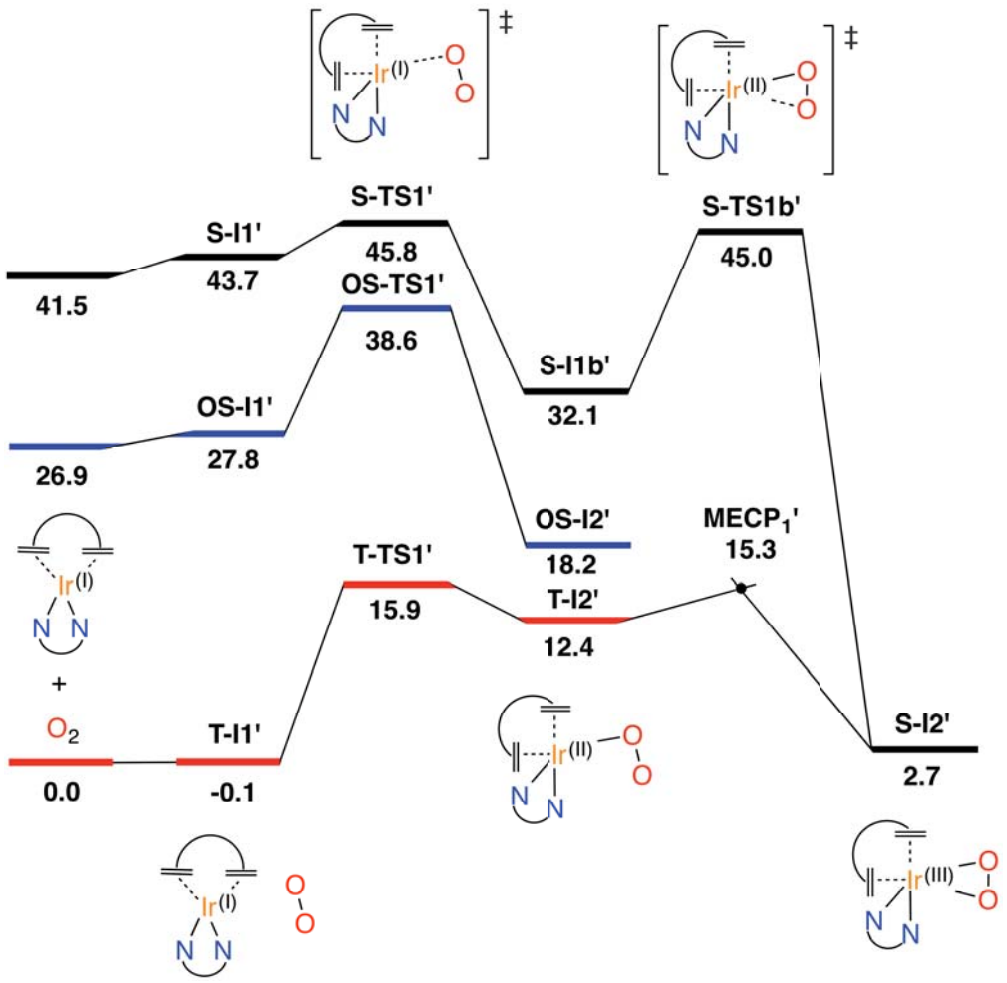


**Figure 6.6.** Gibbs energy profile in benzene, in kcal·mol$^{-1}$, for the coordination of $O_2$ to the [Ir(PhN=C(NMe$_2$)NPh)(cod)] complex. The different spin state of the stationary points is depicted in red (T), blue (OS) and black (S).

In order to oxidize the cod from **S-I2'**, a rearrangement of the $O_2^{2-}$ ligand from an almost coplanar orientation with respect to the C=C bond to an orthogonal disposition is required (Figure 6.7). This orientation favors the insertion of the olefin into the Ir–O bond in two sequential steps, and gives rise to the iridadioxolane species **S-I4'** through an energy barrier of 32.3 kcal·mol$^{-1}$ (**S-TS3'**, Figure 6.8). It has been experimentally shown that the exposure of these metalladioxolane species, **S-I4',** to a source of light or protons[283] (Scheme 6.4) leads spontaneously to the formation of hydroxy-oxo species, **S-I5'**. In fact, we could locate a transition state (**S-TS4',** Figure 6.7) that entailed the beta-hydrogen migration from the cod ligand to the $O_{(1)}$,

thus connecting both **S-I4'** and **S-I5'** intermediates. However, this step required a high-energy barrier of 46.4 kcal·mol$^{-1}$, which does not account for the experimental observations. In order to justify this transformation, we moved the H atom (Scheme 6.4) in the **S-I4'** intermediate from the C atom of the cod ligand to the $O_1$ atom and reoptimized this structure. Indeed, it yields the O–O bond cleavage without energy barrier and results in the formation of the **S-I5'** product. This suggests that adventitious water molecules or other source of protons may assist the hydrogen migration step.

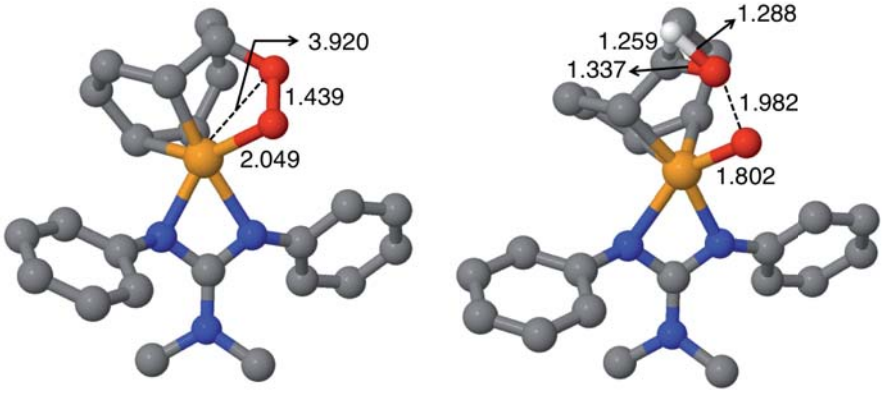


**Figure 6.7:** Optimized geometries of **S-TS3'** (left) **and S-TS4'** (right). Color code: orange = Ir, blue =N, red = O, gray = C, white = H. The H atoms are removed for clarity, except one. Selected bond distances for all the other species involved in the reaction pathway are shown in Appendix (Table A6.2).

**Scheme 6.4:** Rearrangement of metalladioxolane upon exposure to light (top) or protons (bottom).

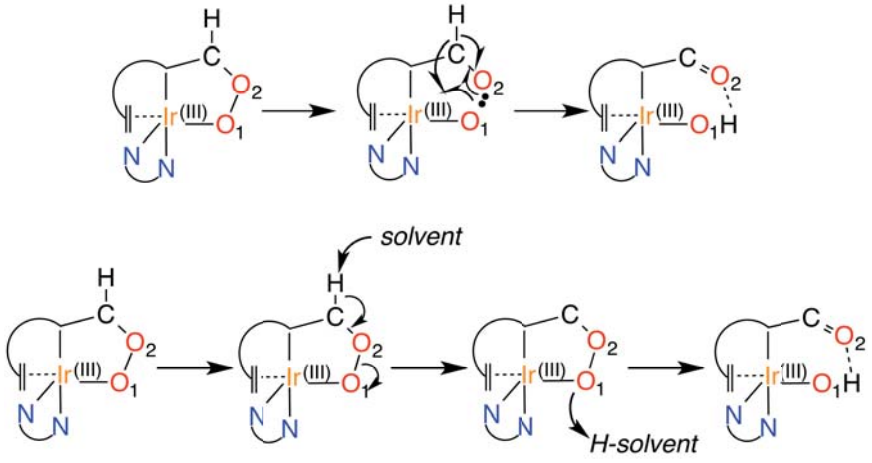

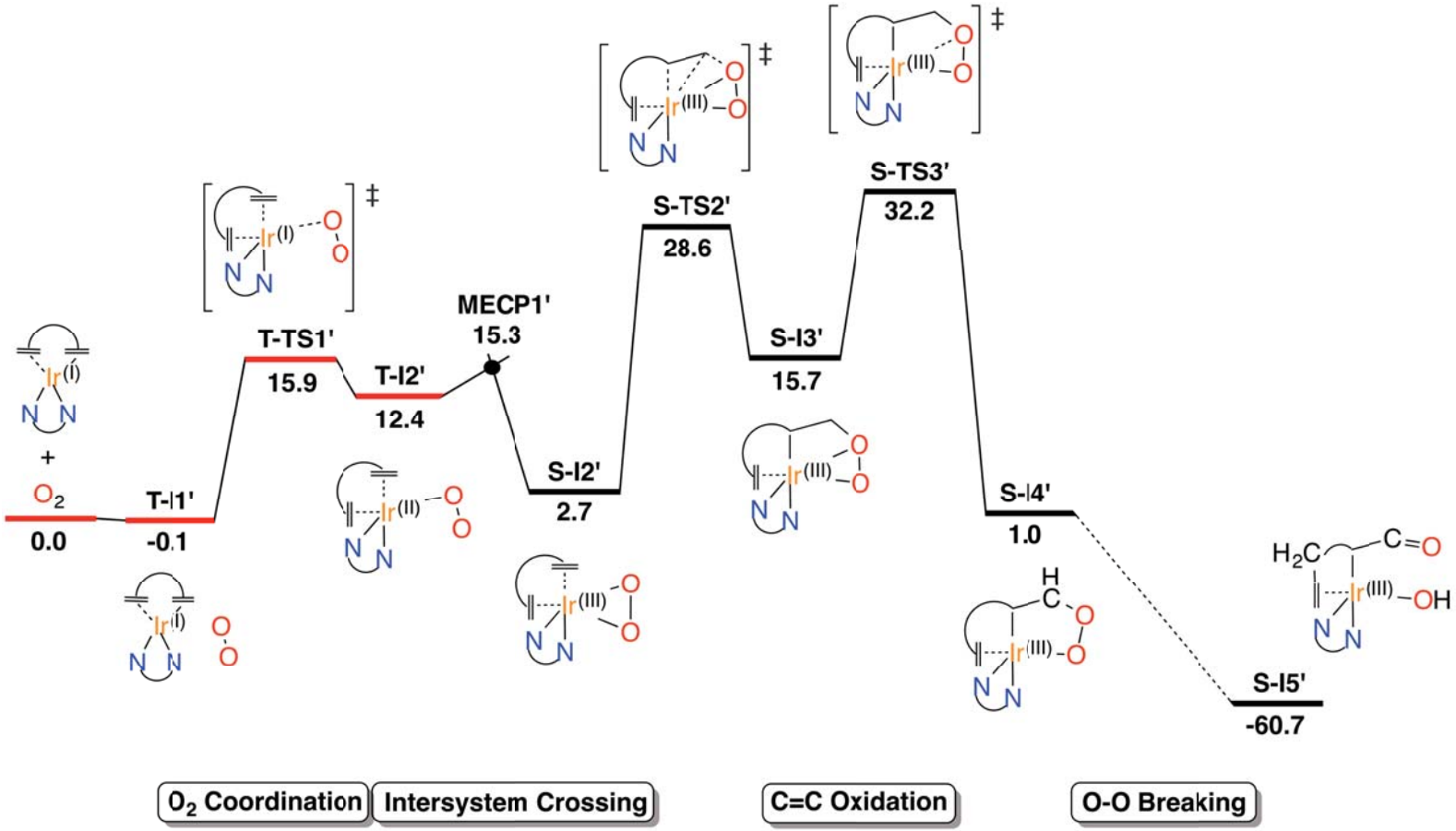


**Figure 6.8.** Lowest Gibbs energy profile in benzene, in kcal·mol$^{-1}$, for the oxidation of cod in the [Ir(PhN=C(NMe$_2$)NPh)(cod)] complex. The different spin states of the stationary points are depicted in red (T) and black (S).

This mechanism shares the same four reaction steps than the above mechanism proposed for the [Rh(PhN$_3$Ph)(cod)] complex, Figure 6.2, namely i) oxygen coordination, ii) intersystem crossing (ISC), iii) O–O breaking bond and iv) C=C bond oxidation. However, they differ in the order in which these steps appeared along the reaction pathway. Specifically, in the Ir complex the intersystem crossing takes place right after $O_2$ is coordinated to the metal, whereas in Rh it happens once a second incoming metal unit interacts with the $O_2^-$. Thus, in the Ir system, the singlet $\eta^2$-peroxide is the responsible to trigger the alkene oxidation followed by the O–O bond cleavage.

Table 6.2 shows the spin densities for the **T-I1'** and **T-I2'** intermediates. In **T-I1'**, both unpaired electrons are located in the oxygen molecule, while in **T-I2'** the metal center is bound to $O_2$ and is oxidized to Ir(II). At this point the ISC between the **T-I2'** and the **S-I2'** takes place and the metal center is further oxidized to Ir(III).

**Table 6.2:** Spin densities (ρ), in a.u., on the Ir and O atoms, for the most stable intermediates involved in the reaction pathway using the [Ir(PhN=C(NMe$_2$)NPh)(cod)] complex.

| Species | ρ(Ir) | ρ(O$_1$) | ρ(O$_2$) |
|---|---|---|---|
| **T-I1'** | 0.00 | 0.99 | 1.01 |
| **T-I2'** | 0.58 | 0.54 | 0.76 |
| **S-I2'** | 0.00 | 0.00 | 0.00 |

**Scheme 6.5:** Representation of the spin densities (ρ) of the Ir and O atoms, in a.u., for the most stable intermediates involved in the reaction pathway using the [Ir(PhN=C(NMe$_2$)NPh)(cod)] complex.

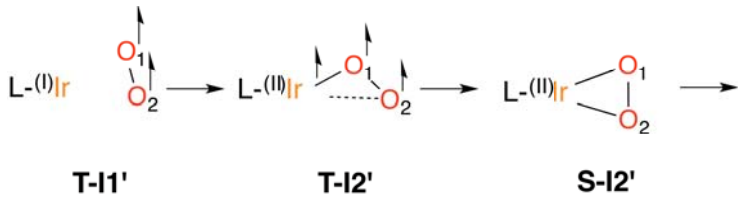


For the sake of completeness, the formation of the dinuclear 2-metallaoxetane, previously observed for the [Rh(PhN$_3$Ph)(cod)] species, was also investigated for the Ir system. However, in this case the dimerization

arises in the singlet PES, instead of in the triplet one. As it is shown in Figure 6.9, the singlet peroxide **S-I2'** species interacts with a second transition metal complex leading to the **S-I6'** intermediate. At this stage, the O–O bond breaking step occurs, involving an even higher transition state, **S-TS6'** (43.9 kcal $mol^{-1}$). In spite of the stability of the resulting product **S-I10',** the formation of the dinuclear 2-metallaoxetane can thus be excluded.

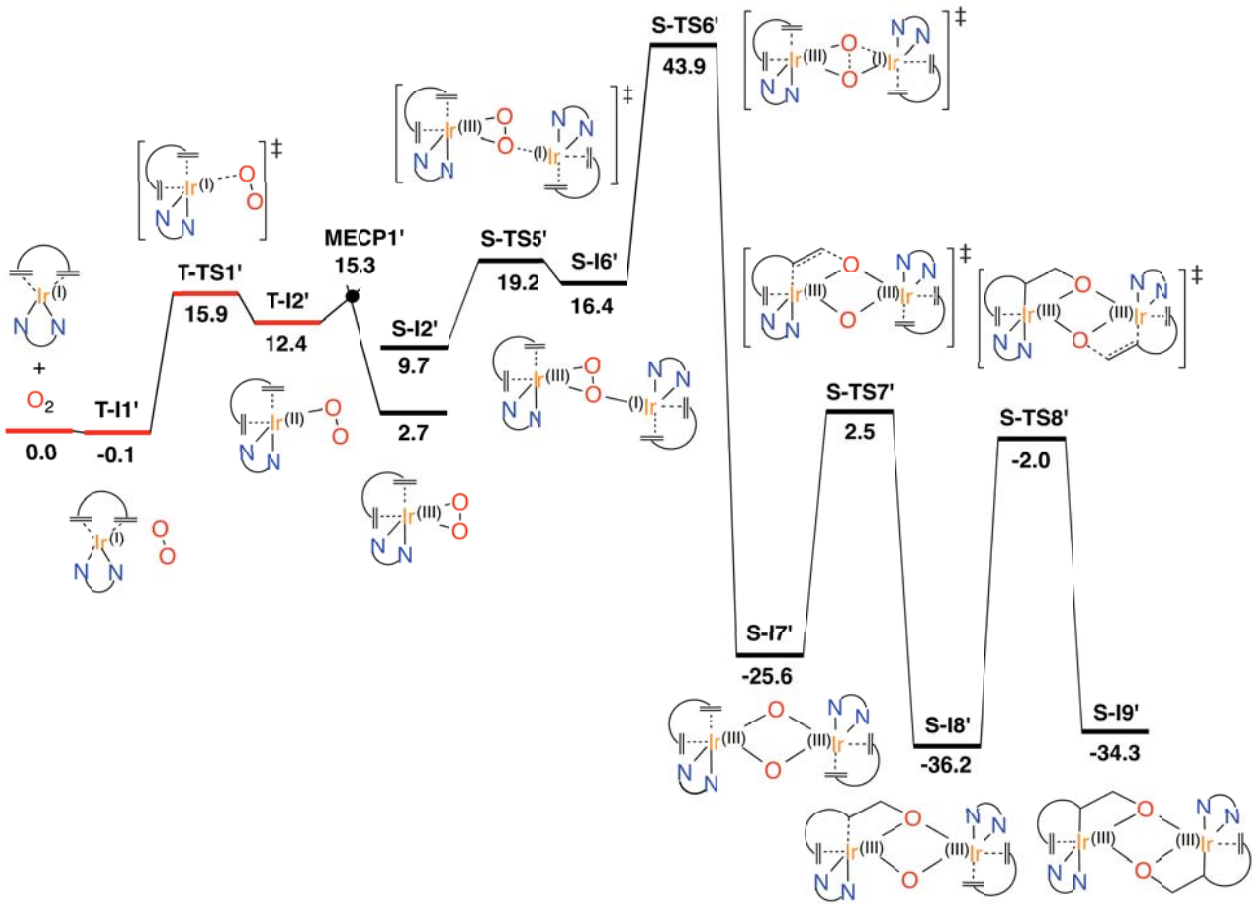


**Figure 6.9:** Gibbs energy profile in benzene, in kcal·mol$^{-1}$, for the formation of the dinuclear 2-iridametallaoxetane from [Ir(PhN=C(NMe$_2$)NPh)(cod)] and $O_2$. The different spin state of the stationary points is depicted in red (T) and black (S).

### 6.3.1.4. Effect of the Transition Metal

According to the lowest Gibbs energy profiles shown in Figures 6.2 and 6.6, the main difference between the Rh and Ir-mediated oxidations remains in the reversed stability of the superoxo and peroxo species generated upon $O_2$ insertion (**T-I2/S-I2** and **T-I2'/S-I2'**, respectively). This suggests that the reaction outcome might be governed by the energy difference between these two species. Thus, to gain a better understanding on the metal and ligand effects in these oxidation reactions, the corresponding peroxo and superoxo intermediates were optimized replacing the metal center in the [Rh(PhN$_3$Ph)(cod)] and [Ir(PhN=C(NMe$_2$)NPh)(cod)]) complexes by Ir and Rh, respectively. In this way, complexes with the same ligand set and differing only in the metal center allow to assess metal effects in the stabilization of peroxo and superoxo intermediates. Calculations show that the Rh-for-Ir metal exchange in [Rh(PhN$_3$Ph)(cod)] lowers the energy of both superoxo and peroxo intermediates regardless of the considered spin state (compare Figure 6.1 with Figure 6.9). Specifically, the peroxo adduct with Ir is stabilized to a greater extent, thus becoming 8.0 kcal·mol$^{-1}$ below the superoxo one. This contrasts with the initial Rh complex, where the superoxo adduct was 5.9 kcal·mol$^{-1}$ more stable than the peroxo species.

On the other hand, the effect of the ligand can be also evaluated by comparing the stability of the $O_2$-coordinated intermediates for the Ir-substituted [Ir(PhN$_3$Ph)(cod)] complex with the Rhode's one, [Ir(PhN=C(NMe$_2$)NPh)(cod)] (Figure 6.6). Energetics indicate that both superoxo and peroxo species are more stable with the (PhN$_3$Ph) ligand (Figure 6.9) than with (PhN=C(NMe$_2$)NPh). Therefore, the (PhN$_3$Ph) ligand favors electron transfer to the $O_2$ unit.

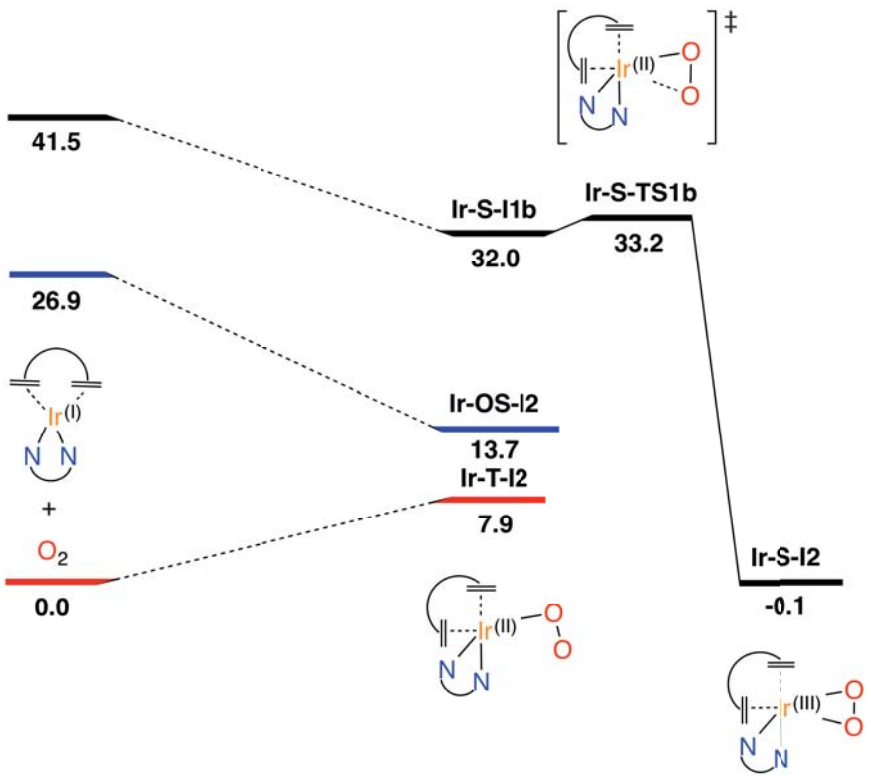


**Figure 6.9.** Gibbs energy profile in toluene, in kcal·mol$^{-1}$, for the $O_2$ coordination to [Ir(PhN$_3$Ph)(cod)]. The different spin state of the stationary points is depicted in red (T), blue (OSS) and black (S).

In contrast, when Ir is replaced by Rh in the [Ir(PhN=C(NMe$_2$)NPh)(cod)] complex, all the intermediates go up in energy, in particular the **Rh-S-I2'** peroxo species, when comparing the energy profiles in Figures 6.6 and 6.10. In this case, however, the energy difference between the more stable superoxo (**Rh-T-I2'**) and peroxo (**Rh-S-O2'**) species is only 1.6 kcal·mol$^{-1}$. As regards to the ligand, the superoxo and peroxo adducts are also more stable with the (PhN$_3$Ph) ligand, as previously observed with Ir.

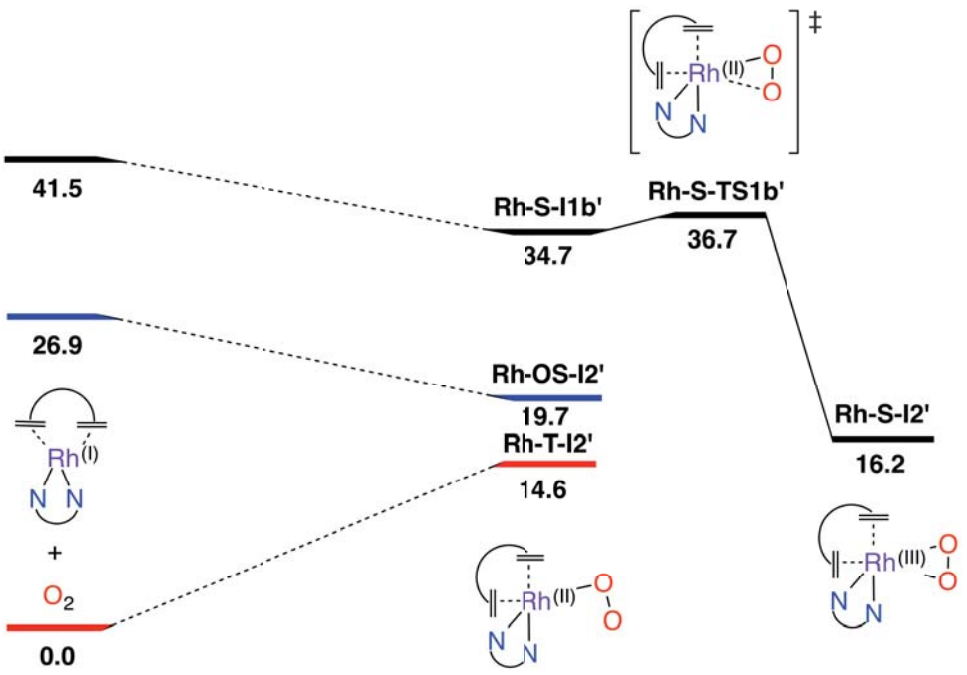


**Figure 6.10.** Gibbs energy profile in benzene, in kcal·mol$^{-1}$, for the $O_2$ coordination to [Rh(PhN=C(NMe$_2$)NPh)(cod)]. The different spin state of the stationary points is depicted in red (triplet), blue (open-shell singlet) and black (closed-shell singlet).

### 6.3.2. Factors Governing Alkene Oxidation

In order to gain insight into the different nature of the metal ligands and the metal center, we performed an activation-strain analysis[284–286] on the superoxo and peroxo species generated from the four Rh and Ir complexes (Figure 6.11). In this type of analysis, the energy ($\Delta E$) required to form [M(L)(cod)]-$O_2$ species from two interacting fragments, [M(L)(cod)] and $O_2$, is decomposed as $\Delta E = \Delta E_{dist} + \Delta E_{int}$, where $\Delta E_{dist}$ and $\Delta E_{int}$ are the distortion and interaction energies, respectively. The $\Delta E_{dist}$ term can be understood as the energy cost associated with the geometric distortion of the [M(L)(cod)] and $O_2$ fragments from their structure as isolated species to their "strained" geometries in the reaction intermediate. On the other hand, $\Delta E_{int}$ stands for the energy gain arising from the interaction of those fragments with each other in the intermediate species.

The values shown in Figure 6.11 reveal that the $\Delta E_{dist}$ terms for the $O_2$ fragment are much larger for the peroxo species than for the superoxo ones.

This is perfectly consistent with the more elongated O–O bond distances in the peroxo adducts. Conversely, the differences in the $\Delta E_{dist}$ for the [M(L)(cod)] fragments are much less pronounced. Figure 6.11 also shows that for both Rh and Ir, the $\Delta E_{int}$ in the peroxo species are significantly larger than in the superoxo ones, as expected from the number of electrons transferred from the metal to the $O_2$ in each adduct (peroxo: two; superoxo: one). For the Rh compounds, the energy gain is not enough to compensate the substantial energy penalty that mainly arises from the distortion of the $O_2$ fragment; as a result, peroxo intermediates becomes less stable than the superoxo ones. In contrast, for Ir compounds, even though the $\Delta E_{dist}$ terms are even higher, the $\Delta E_{int}$ are large enough to offset that energy cost and make the peroxo species more stable. Thus, regardless of the nature of the ligand, the Ir stabilizes more the superoxo and peroxo intermediates than Rh and in particular the latter species to a larger extent.

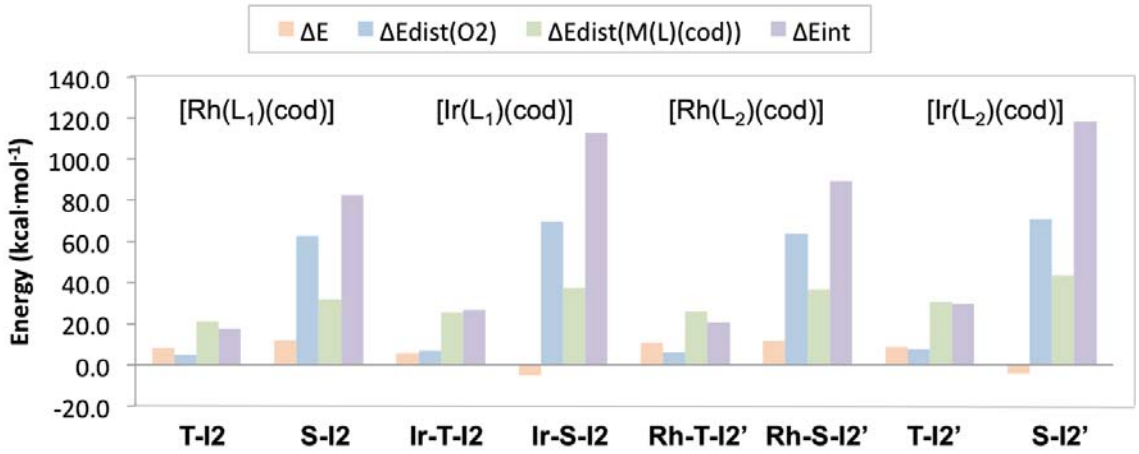


**Figure 6.11.** Activation-strain analysis for the superoxo and peroxo species formed from [M($L_1$)(cod)] and [M($L_2$)(cod)] complexes with M = Rh or Ir, and $L_1$ and $L_2$ [(PhN$_3$Ph)] and [(PhN=C(NMe$_2$)NPh)], respectively.

These results were further confirmed by performing a second order perturbation theory analysis of the Fock matrices in the natural bond orbital (NBO) basis,[277] which estimates the donor-acceptor interactions. Indeed, this analysis shows that the interactions, i.e. donation and backdonation, between the metal center and the ligands in the [M(PhN$_3$Ph)(cod)] and [M(PhN=C(NMe$_2$)NPh)(cod)] complexes are much stronger with M = Ir. This is mainly due to a more effective overlap between the Ir–$O_2$ and ligands

orbitals. This better overlap results in an increase of the electron density at the Ir center, which favors the stabilization of the higher oxidation state Ir(III) in the peroxo complex.

Tables 6.3 and 6.4 show the donor-acceptor interactions between the M–$O_2$ fragment and the ($PhN_3Ph$), ($PhN{=}C(NMe_2)NPh$) and cod ligands. In the case of $PhN_3Ph$, the antibonding orbitals of the peroxo adducts accept electron density from one bonding orbital of the cod ligand and from one lone pair of a nitrogen atom of the ($PhN_3Ph$) ligand (Figure 6.12), while in superoxo adducts the flow of electron density mainly comes from the cod fragment. On the other hand, with the ($PhN{=}C(NMe_2)NPh$) ligand, the peroxo species interact with two bonding orbitals, one from the cod and the other from the multidentate nitrogen ligand, and with one lone pair of a nitrogen atom, while the superoxo only with the cod. In all cases, the interaction between the different ligands and the M–$O_2$ results much stronger with Ir than with Rh, which hinders the stabilization of high oxidation states in the latter case.

**Table 6.3:** Donor-acceptor interactions in the second order perturbation analysis of NBO for the peroxo and superoxo species in the [M($PhN_3Ph$)(cod)] (M=Ir, Rh) complexes.

| Species | Donor | Orbitals | Acceptor | Orbitals | Energy |
|---|---|---|---|---|---|
| Ir-peroxo | BD C=C | C8 s(10%)p(90%)<br>C12 s(9%)p (90%) | BD* Ir-O2 | O s(9%)p(91%)<br>Ir s(14%)d(86%) | 186.61 |
| | LP N | s(33%)p(67%) | BD* Ir-O1 | O s(9%)p(91%)<br>Ir s(14%)d(86%) | 109.36 |
| Rh-peroxo | BD C=C | C9 s(5%) p(95%)<br>C13 s(5%) p(95%) | BD* Rh-O2 | Rh s(10%) d(90%)<br>O s(5%) p(95%) | 104.20 |
| | LP N | s(35%) p(65%) | BD* Rh-O1 | Rh s(9%) d(91%)<br>O s(6%) p(94%) | 72.91 |
| Ir-superoxo | BD C=C | C18 s(10%)p(90%)<br>C12 s(10%)p(90%) | BD* Ir-O1 | O s(10%)p(90%)<br>Ir s(17%)d(83%) | 95.68 |
| Rh-superoxo | BD C=C | C9 s(7%)p(93%)<br>C13 s(7%)p(93%) | BD* Rh-O1 | Rh s(15%)d(85%)<br>O s(5%)p(95%) | 60.55 |

**Table 6.4:** Donor-acceptor interactions in the second order perturbative analysis of NBO for the peroxo and superoxo species in the [M(PhN=C(NMe$_2$)NPh)(cod)] (M=Ir, Rh) complexes.

| Species | Donor | Orbitals | Acceptor | Orbitals | Energy |
|---|---|---|---|---|---|
| Ir-peroxo | BD C=C | C9 s(11%)p(89%)<br>C13 s(10%)p(90%) | BD* Ir-O2 | Ir s(33%)d(66%)<br>O s(9%)p(91%) | 192.01 |
| | BD N-C | N s(12%)p(88%)<br>C s(1%)p(99%) | BD* Ir-O1 | Ir s(36%)d(63%)<br>O s(9%)p(91%) | 78.42 |
| | LP N | s(20%)p(80%) | BD* Ir-O1 | Ir s(36%)d(63%)<br>O s(9%)p(91%) | 25.39 |
| Rh-peroxo | BD C=C | C8 s(7%)p(93%)<br>C12 s(6%)p(94%) | BD* Rh-O2 | O s(6%)p(94%)<br>Rh s(34%)d(66%) | 103.52 |
| | LP N | s(26%)p(74%) | BD* Rh-O1 | O s(6%)p(94%)<br>Rh s(36%)d(64%) | 27.95 |
| | BD N-C | N s(4%)p(96%)<br>C p(100%) | BD* Rh-O1 | O s(6%)p(94%)<br>Rh s(36%)d(63%) | 40.55 |
| Ir-superoxo | BD C=C | C9 s(11%)p(89%)<br>C13 s(11%)p(89%) | BD* Ir-O1 | Ir s(10%)d(90%)<br>O s(11%)p(89%) | 93.14 |
| Rh-peroxo | BD C=C | C8 s(8%)p(92%)<br>C12 s(8%)p(92%) | BD Rh-O1- | Rh s(15%)d(85%)<br>O s(6%)p(94%) | 64.03 |

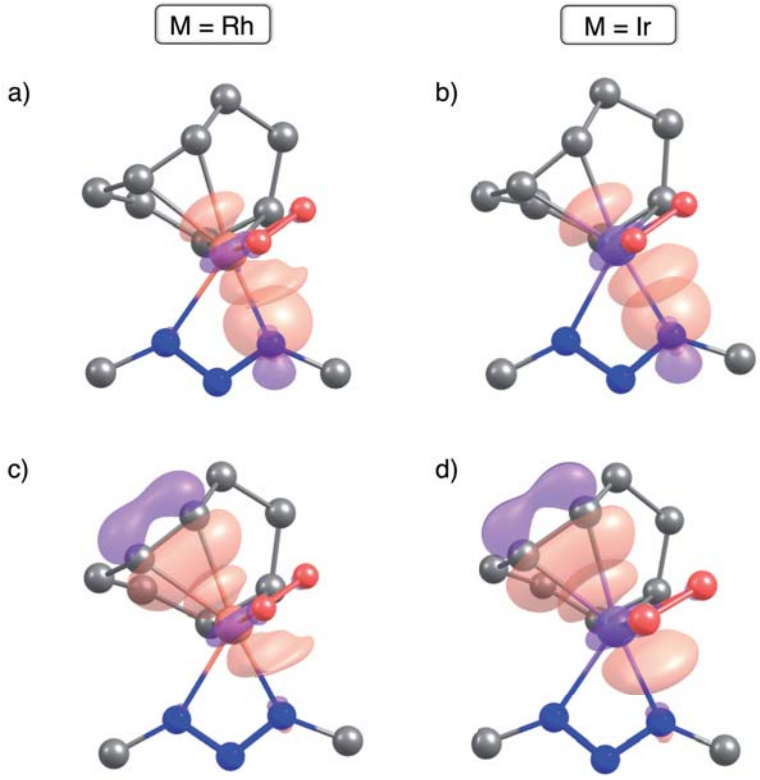


**Figure 6.12.** Representation of the NBOs involved in the electron donation from the (a), (b) N-ligands and (c), (d) cod ligand to the metal center in the peroxo species with [M(PhN$_3$Ph)(cod)]. For the sake of clarity, the H atoms have been omitted and the Ph groups have been simplified. Color code: C (gray), O (red), N (blue), Rh (orange), and Ir (purple).

## 6.4. Discussion and Conclusions

DFT calculations have been performed to shed light into the different reactivity reported for the partial oxidation with $O_2$ of the cod ligand in the similar [Rh(PhN$_3$Ph)(cod)] and [Ir(PhN=C(NMe$_2$)NPh)(cod)] complexes. In the case of the Rh complex, we found that the lowest energy reaction mechanism involves two metal units, which accounts for the experimental observation of a dinuclear 2-metallaoxetane compound. Conversely, for the Ir compound, our calculations indicate that the oxidation of the cod ligand takes place with a single metal center leading to the monomeric oxygenated product characterized experimentally. These two reaction mechanisms differ once $O_2$ binds to the metal complex, giving rise to either a superoxo or a peroxo adduct. Therefore, the reaction outcome may be dictated by the relative stabi-

lity of these species. Activation strain and NBO analyses suggest that favoring one or the other adduct mainly depend on the electronic properties of the metal center, although ligands with very different electron-donating abilities might also play a role. This might be particularly important for Rh-based complexes, for which we have shown that the superoxo and peroxo species are very close in energy. On the other hand, Ir-based complexes may only favor the formation of monooxygenated products, as they stabilize to a larger extent the peroxo adducts due to a better overlap between the metal and ligands orbitals.

Overall, this work provides a detailed picture of the reaction mechanisms involved in the oxidation of alkenes using $O_2$ as oxidant, as well as the main factors that govern this reactivity. The results obtained also account for the reaction products experimentally observed, and accordingly, they might be also useful for predicting the product distribution in other alkene oxidations. Therefore, this work may pave the way for the future design of new high-performance complexes for the selective functionalization of alkenes using molecular oxygen.

## Appendix

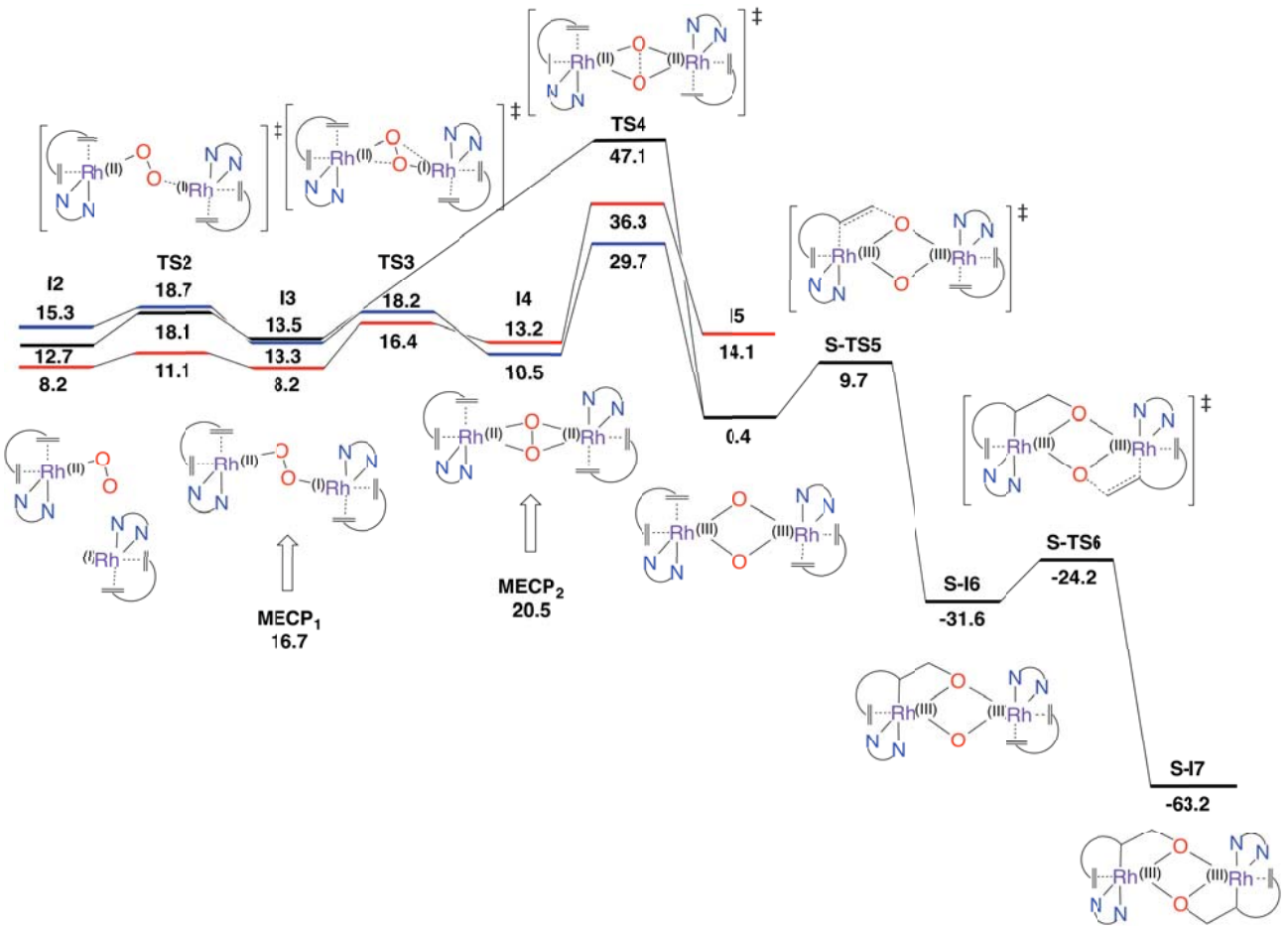


Figure A6.1: Gibbs energy profile in toluene, in kcal·mol$^{-1}$, for the intersystem crossing, O–O breaking and C=C oxidation catalyzed by [Rh(PhN$_3$Ph)(cod)]. The different spin state of the stationary points is depicted in red (triplet), blue (open-shell singlet) and black (closed-shell singlet).

Table A6.1: Selected bond distances (d), in Å, for some of the species involved in the triplet (T), open shell singlet (OS) and closed shell singlet (S) state pathways catalyzed by [Rh(PhN$_3$Ph)(cod)].

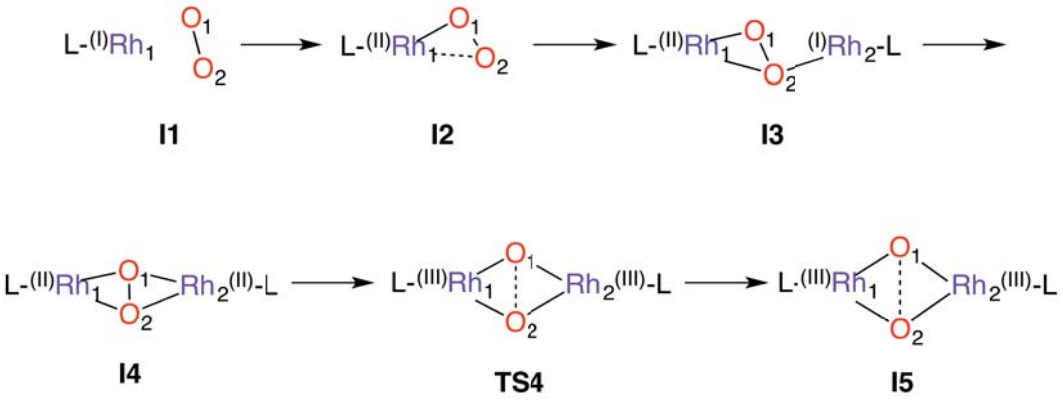


| Species | d(Rh$_1$–O$_1$) | d(Rh$_1$–O$_2$) | d(Rh$_2$–O$_1$) | d(Rh$_2$–O$_2$) | d(O$_1$–O$_2$) |
|---|---|---|---|---|---|
| **T-I1** | 3.380 | 3.471 | - | - | 1.179 |
| **T-I2** | 2.084 | 2.381 | - | - | 1.251 |
| **T-I3** | 2.074 | 2.405 | 3.005 | 2.128 | 1.281 |
| **T-4** | 2.017 | 2.359 | 2.423 | 1.997 | 1.424 |
| **T-TS4** | 2.025 | 2.328 | 2.343 | 1.994 | 1.991 |
| **T-I5** | 1.966 | 1.931 | 2.019 | 2.286 | 2.586 |
| **OS-I1** | | | - | - | 1.179 |
| **OS-I2** | 2.021 | 2.420 | - | - | 1.271 |
| **OS-I3** | 2.065 | 2.444 | 2.994 | 2.115 | 1.285 |
| **MECP1** | 2.025 | 2.141 | 3.001 | 2.179 | 1.319 |
| **OS-I4** | 2.031 | 2.290 | 2.290 | 2.031 | 1.423 |
| **OS-TS4** | 2.018 | 2.247 | 2.247 | 2.018 | 1.929 |
| **OS-I5** | 1.973 | 1.988 | 1.988 | 1.973 | 2.552 |
| **S-I1** | 3.056 | 3.753 | - | - | 1.190 |
| **S-I1b** | 2.337 | 3.071 | - | - | 1.214 |
| **S-I2** | 1.973 | 1.993 | - | - | 1.346 |
| **S-I3** | 1.969 | 1.997 | 3.037 | 2.172 | 1,374 |
| **S-TS4** | 1.966 | 1.977 | 2.166 | 2.038 | 1.834 |
| **S-I5** | 1.973 | 1.988 | 1.988 | 1.973 | 2.552 |

Table A6.2: Selected bond distances (d), in Å, for some of the species involved in the triplet (T), open shell singlet (OS) and closed shell singlet (S) state pathways catalyzed by [Ir(PhN=C(NMe$_2$)NPh )(cod)].

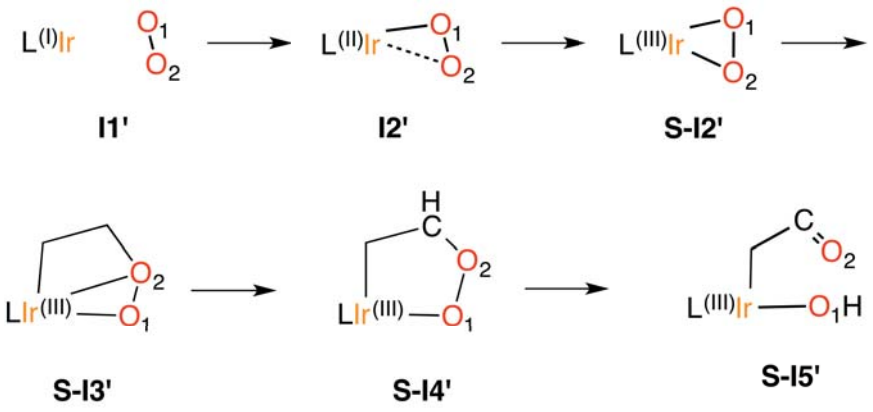


| Species | d($Ir_1$–$O_1$) | d($Ir_1$–$O_2$) | d($O_1$–$O_2$) |
|---|---|---|---|
| **T-I1'** | 3.478 | 3.769 | 1.179 |
| **T-I2'** | 2.075 | 2.484 | 1.271 |
| **OS-I1'** | 3.477 | 3.613 | 1.179 |
| **OS-I2'** | 2.040 | 2.579 | 1.284 |
| **S-I1'** | 3.056 | 3.753 | 1.190 |
| **S-I1b'** | 1.921 | 2.817 | 1.265 |
| **MECP1'** | 2.105 | 2.242 | 1.286 |
| **S-I2'** | 1.976 | 1.995 | 1.383 |
| **S-I3'** | 2.075 | 2.031 | 1.425 |
| **S-I4'** | 1.921 | 2.843 | 1.431 |
| **S-I5'** | 1.914 | 3.455 | 2.830 |

*"Nothing tends so much to the corruption of science as to suffer it to stagnate; these waters must be troubled before they can exert their virtues"*

Edmund Burke

# 7

# *Copper-Catalyzed Oxidation of Aromatic C-H Bonds*

This chapter results from a mixed experimental/computational study on the hydroxylation of benzene to phenol with hydrogen peroxide catalyzed by a family of copper(I) complexes bearing trispyrazolylborate ligands. The electronic nature of the active species and the hydroxylation reaction of benzene, by means of electrophilic aromatic substitution and rebound mechanisms, have been investigated.

All the experiments in the present study were performed in the research group of Prof. Pedro Pérez at the University of Huelva.

## 7.1.Introduction

Great efforts have been made into develop new strategies that enable the one-step process for the direct conversion of benzene into phenol. Nonetheless, efforts toward this end have usually failed because phenol is easier to oxidize than benzene, which entails the generation of over-oxidation products.[287,288]

Several green oxidation agents have been employed for this reaction such as $O_2$, $N_2O$ and $H_2O_2$.[289,290] The direct hydroxylation of benzene with molecular oxygen would meet economical as well as environmental criteria for an ideal process. Unfortunately, relative high temperatures are required to activate $O_2$, which entails the complete oxidation of benzene into carbon dioxide and water, thus decreasing the selectivity to phenol. However, the use of palladium membranes[291] or the activation of oxygen with carbon monoxide and metal heteropolyacids[292] have been proposed to reduce the cumbersome overoxidation. As regards the use of $N_2O$ as oxidant, it is widely employed in zeolite frameworks,[293,294] which allow to activate $N_2O$ and convert benzene to phenol with a low activation energy and high selectivity. However, the high cost of producing $N_2O$ as feedstock limits the application of this methodology. In contrast, the use of hydrogen peroxide as oxidant is highly desirable because it is relatively inexpensive compared with other organic peroxides and peracids. Further, it only yields water as byproduct.

An array of chemical systems have been described for the oxidation of benzene with $H_2O_2$,[295,296] although most of them requiring strong reaction conditions and acidic medium. In fact, the majority of reported examples do not improve the results obtained by means of the so-called Fenton-chemistry approach.[297,298] This consists of an Fe(II)/$H_2O_2$ system in water at pH = 2, that in addition to converting benzene into phenol also provides mixtures of other oxidation products, thus yielding low selectivities, due to the involvement of hydroxyl radicals. One of the best results reported to date employing $H_2O_2$ was described by Bianchi, Vignola and co-workers,[299] and correspond to a water-soluble iron catalyst that afford a phenol selectivity of 97% with a benzene conversion of 8-10%. However, this high selectivity was only achieved in the presence of trifluoroacetic acid as cocatalyst.

In 2011, Pedro Pérez *et al.* reported the oxidation of benzene with $H_2O_2$ in the presence of copper-based catalysts,[300] with the aim of developing an acid-free catalytic system at relatively mild conditions (T = 60°C and 0.5 mmol% catalyst load). A series of complexes of general formula $Tp^xCu(NCMe)$ ($Tp^x$ = trispyrazolylborate) (Scheme 7.1) were investigated as potential catalysts for this reaction, leading to conversions within the range of 14-30%. In all cases, phenol was obtained as the major product in the reaction mixture within a 67-85%. The rest of the reacted benzene accounted for 1,4-benzoquinone, which results from the overoxidation of phenol (Scheme 7.2).

**Scheme 7.1:** Hydrotrispyrazolylborate ligands.

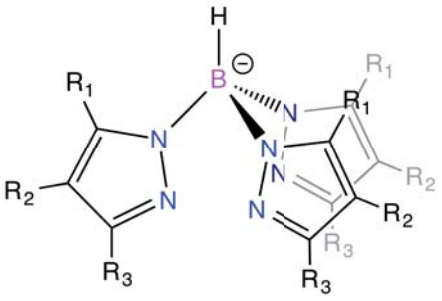


$Tp^{Br3}$: $R^1 = R^2 = R^3 = Br$

$Tp^{*Br}$: $R^1 = R^3 = Me$; $R^2 = Br$

$Tp^{*}$: $R^1 = R^2 = R^3 = Me$

$Tp^{Me2}$: $R^1 = R^3 = Me$ ; $R^2 = H$

$Tp^{Ph}$: $R^1 = R^2 = H$; $R^3 = Ph$

**Scheme 7.2:** Oxidation of benzene with hydrogen peroxide and $Tp^xCu(NCMe)$ as catalysts.

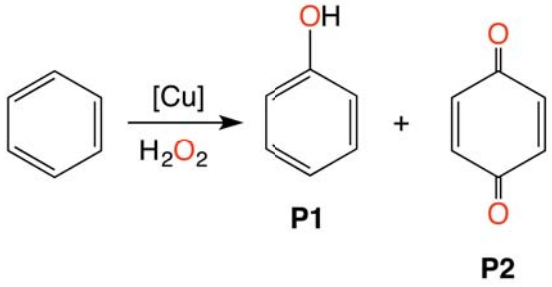


## 7.2. Experimental Results

Once demonstrated the capabilities of these copper complexes to catalyze the oxidation of the C–H bonds of benzene, Pedro Pérez *et al.* focused on finding out the mechanism of this reaction. More especially, particular attention was devoted to investigate whether radical species were involved in these catalyzed reactions. In fact, a well-known feature of transition metals is

their ability to promote the decomposition of $H_2O_2$, leading to hydroxyl radicals that further induce oxidation reactions in a non-selective way (Fenton chemistry).[15] Under these conditions, the oxidation of benzene would produce biphenyl derivatives as the result of the coupling of two phenyl radicals,[298] which were not detected in the product mixture. Therefore, to check whether other radical species were involved in the catalytic process, radical traps were added into the benzene oxidation reaction. Similar benzene conversion and selectivity toward phenol were obtained in the absence and in the presence of $CCl_4$ or $CBrCl_3$. However, minor but detectable amounts of chloro- or bromobenzene could be identified, demonstrating the formation of small amounts of the $C_6H_5^{\cdot}$ radical.

In order to get more acquainted with the reaction mechanism, hydrogen peroxide was replaced by oxone that contains $KHSO_5$ as oxidant. A mixture of phenol and benzoquinone was also achieved, with similar yields and selectivities to those observed with hydrogen peroxide, which suggests that the operating mechanism is similar in both cases. These results provide valuable information about the reaction process since the formation of peroxidic complexes is unlikely with oxone, which acts as a single-oxygen atom transfer agent. The formation of superoxo and hydroperoxo complexes as catalytic active species is thus unlikely. Moreover, in oxidation reactions involving oxone no hydroxyl radicals are detected,[302] which would be in agreement with the reaction products obtained in our experiments.

To reinforce the data obtained by benzene, Pérez *et al.* also studied the reaction of toluene and $H_2O_2$ with $Tp^{*,Br}Cu(NCMe)$ as catalyst, achieving a toluene conversion of 35%. The resulting mixture was analyzed by means of gas chromatography (GC) and gas chromatography - mass spectrometry (GC-MS) methods (Figure 7.1).

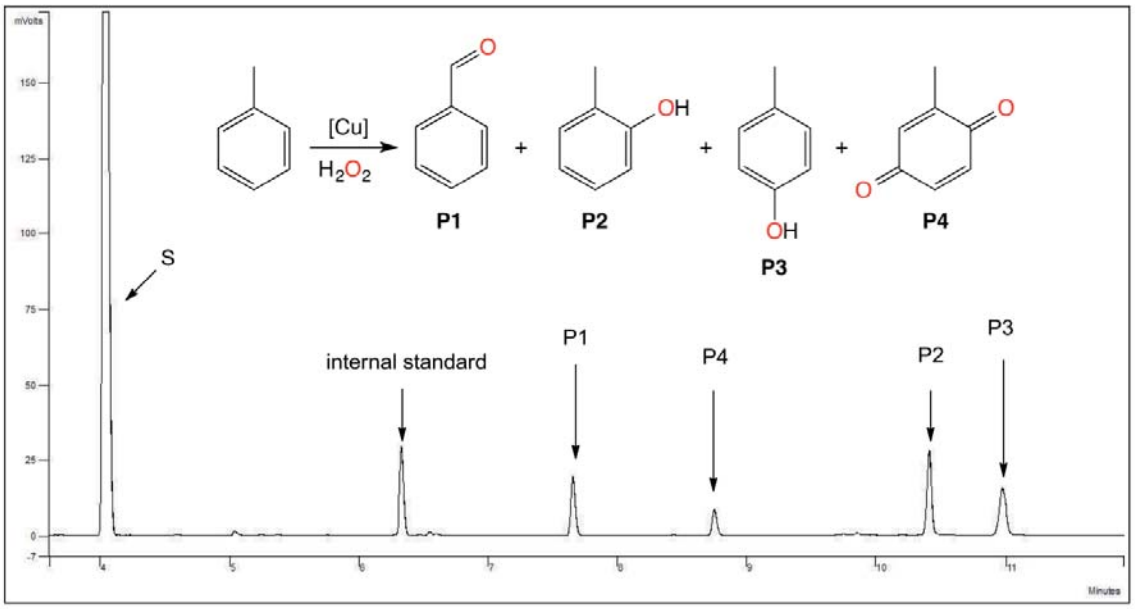


**Figure 7.1**: GC of toluene oxidation reaction with hydrogen peroxide and $Tp^{*,Br}Cu(NCMe)$ as catalyst. The internal standard employed corresponds to cycloheptanone.

The signals obtained were assigned to benzaldehyde, *ortho*- and *para*-cresols and 2-methyl-1,4-benzoquinone in a distribution of 26:34:29:11, whereas the product coupling derived from aryl radicals was not identified. This product distribution was similar to that found by Sawyer and coworkers,[303] where they proposed that some iron-based catalysts for these transformations did not operate throughout the HO· route. Aside from this, other groups have also found evidences against the involvement of hydroxyl radicals in this type of catalytic processes.[304,305] Therefore, data collected so far seemed to disfavor the involvement of HO· radicals as activating agents in the ongoing copper-catalyzed process.

A set of experiments were also carried out with other substituted benzenes containing groups with different electron donating and withdrawing character, to assess how the electronic nature of the substrate affects the $sp^2$ C–H bond oxidation reaction (Scheme 7.3).

**Scheme 7.3:** Substituted benzenes explored.

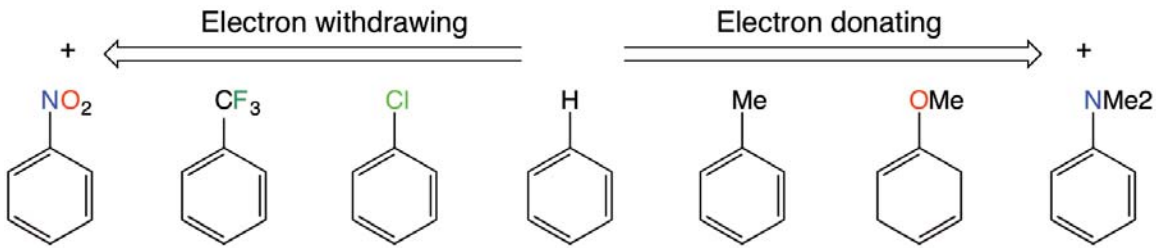


In Table 7.1 are listed the reaction yields and product distributions achieved for all of these substituted benzenes, under the same reaction conditions and by using $Tp^{*,Br}Cu(NCMe)$ and $Tp^{Br3}Cu(NCMe)$ as catalysts.

**Table 7.1:** Oxidation reaction using substituted benzenes. Yields and product distributions.

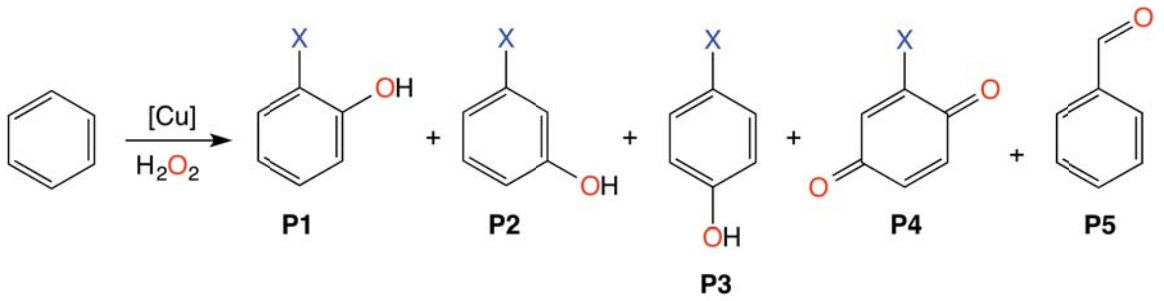


| Ph-X | % P1 | | % P2 | | % P3 | | % P4 | | % P5 | | % Yield | |
|---|---|---|---|---|---|---|---|---|---|---|---|---|
| -X | $Tp^{*,Br}$ | $Tp^{Br3}$ | $Tp^{*,Br}$ | $Tp^{Br3}$ | $Tp^{*,Br}$ | $Tp^{Br3}$ | $Tp^{*,Br}$ | $Tp^{Br3}$ | $Tp^{*,Br}$ | $Tp^{Br3}$ | $Tp^{*,Br}$ | $Tp^{Br3}$ |
| -$NMe_2$ | 73 | 48 | - | - | 27 | 52 | - | - | - | - | 22 | 31 |
| -OMe | 72 | 31 | 7 | 12 | 19 | 16 | 2 | 11 | - | - | 10 | 10 |
| -Me | 31 | 23 | - | - | 21 | 18 | 2 | 35 | 25 | 25 | 14 | 12 |
| -H | 52 | 33 | - | - | - | - | 48 | 67 | - | - | 8 | 10 |
| -Cl | 38 | 29 | - | - | 38 | 32 | 24 | 39 | - | - | 6 | 6 |
| -$CO_2Me$ | 28 | 18 | 31 | 36 | 42 | 46 | - | - | - | - | 5 | 2 |
| -$CF_3$ | 9 | 10 | 52 | 61 | 39 | 30 | - | - | - | - | 1 | 1 |
| -NO2 | 19 | 15 | 28 | 41 | 53 | 44 | - | - | - | - | 3 | 1 |

Yield values correspond to mmol of products/mmol of initial benzene.
Reaction conditions: 0.01 mmol catalyst; 1 mmol substrate; 5 mmol $H_2O_2$; 3 mL of $CH_3CN$; temp = 60°C; time = 4h.

Basically, these results indicate that substituted benzenes with electron-withdrawing groups are less reactive than those with electron-donating ones. In an attempt to evaluate precisely the electronic influence of the X groups, the Hammett equation[306,307] was employed:

$$logK = logK^0 + \sigma\rho \qquad [7.1]$$

where $K$ and $K^0$ represent the rate constants or equilibrium constants of the substituted and unsubstituted benzenes, $\sigma$ a substituent constant and $\rho$ a reaction constant.

In Figures 7.2 and 7.3 is plotted the ratio between the substituted and unsubstituted benzene conversions into the hydroxylated products against the σ constant. By using Tp$^{*,Br}$Cu, as well as Tp$^{Br3}$Cu as catalysts, a progressive trend with the nature of the substituent was observed. Furthermore, the fitting Hammett σρ correlation with a negative value for ρ (-0.71 and -1.1 for Tp$^{*,Br}$Cu and Tp$^{Br3}$Cu, respectively) support the presence of an electrophilic intermediate, positively charged, that would be stabilized by electron-donating substituents on the aromatic ring.

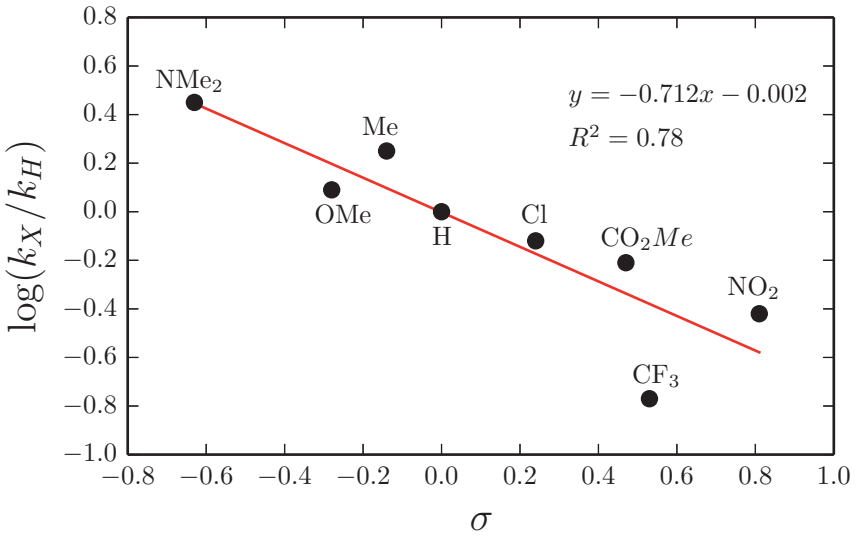


**Figure 7.2**: Linear regression Hammett plot for the C–H oxidation of substituted benzenes catalyzed by Tp$^{*,Br}$Cu.

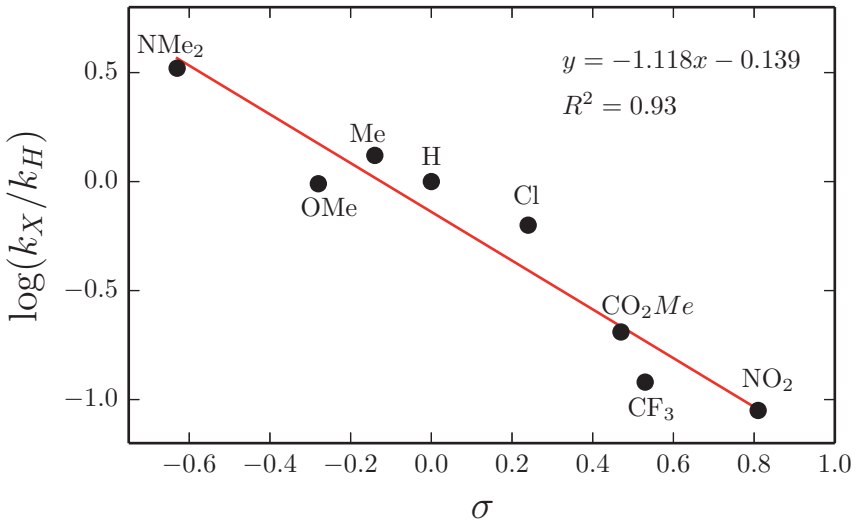


**Figure 7.3**: Linear regression Hammett plot for the C–H oxidation of substituted benzenes catalyzed by $Tp^{Br3}Cu$.

All reactions presented so far were performed in round-bottom flasks of 25 ml equipped by a reflux condenser and a magnetic bar. The reaction mixture, containing the catalyst, substrate, $H_2O_2$ and MeCN (exact quantities are indicated in Table 7.1), was stirred for 4h at 60°C. Sets of experiments at shorter reaction times (10, 30, 60 min) were also conducted to determine whether the reaction is kinetically or thermodynamically controlled. In some of these experiments, however, no oxidation products could be detected, which did not allow us to obtain a conclusive trend. Hence, in the next sections we will compare the reaction conversions obtained experimentally after 4h with the calculated energy barriers.

In summary, experiments suggest that mono-oxygenated copper species are the responsible for the direct hydroxylation of benzene into phenol, while hydroxyl radicals (Fenton-like chemistry) are not involved. The observation of trapped halo-benzenes in small amounts steams from the formation of phenyl radicals at some stage in the catalytic cycle. However, the Hammett plots are in accordance with a typical electrophilic aromatic substitution mechanism ($S_EAr$), which does not involve radical intermediates. Hence, with the aim of providing a better understanding of this oxidation process and accounting for all presented experimental data, a computational study of the reaction mechanism was performed.

## 7.3. Computational Details

All the calculations presented in this work were carried out at the Density Functional Theory (DFT) level using the BHLYP exchange-correlation functional[153,159] by means of the Gaussian09 software.[224] This functional was selected based on previous studies from Sodupe and Rodríguez-Santiago[160,185] on a series of copper-aqua complexes. Therein, the accuracy of several DFT functionals was assessed, giving the BHLYP functional the most accurate results compared to benchmark CCSD(T) calculations.

The H, B, C, N and O atoms were described with a double-ζ 6-31G(d,p) basis set, whereas for the Br and Cu atoms the Stuttgart-Bonn scalar relativistic ECP[194] was used, with its associated basis set. The structures of all the stationary points involved in the reaction were fully optimized in gas phase without any geometry or symmetry constraints. From these geometries, vibrational frequencies were computed analytically in order to characterize them as either energy minima (reactants, intermediates and products) or saddle points (transition states). The located transition states were further confirmed to connect the corresponding reactants and products by means of Intrinsic Reaction Coordinate (IRC) calculations. Frequency calculations were also used to determine the difference between the potential and Gibbs energies, $(G - E)_g$, which includes the zero-point energy and the thermal and entropy corrections. Solvent effects (acetonitrile, Ɛ = 35.688), $E_{sol}$, were introduced through single point calculations on the gas phase optimized structures using the SMD[203] solvation model with the larger triple-ζ 6-311+G** basis set for the H, B, C, N and O atoms. All the energies reported throughout this work correspond to Gibbs energies in acetonitrile, $G_{solv}$, calculated as follows:

$$G_{sol} = (G - E)_g + E_{sol} \qquad [7.2]$$

Local charges and spin densities were obtained from Natural Population Analysis (NPA) calculations.[308] The minimum energy crossing points (MECPs) were located with the program developed by Harvey *et al.*[199] In order to infer how the MECPs relate to the crossing potential energy surfaces, their structures were optimized for the two spin states involved.

The Gibbs energies in solution of the MECPs were obtained by using the energy corrections found for the stationary points on the reactants side.

## 7.4. Theoretical Results

In this section we will start by investigating which is the most feasible catalytic active specie involved in the oxidation process. Then, we will analyze the hydroxylation reaction for benzene, as well as several substituted benzenes, by means of an electrophilic aromatic substitution and rebound mechanisms.

### 7.4.1.Catalytic Active Species

Three oxidized copper complexes were proposed theoretically as potential active species upon the oxidation of the $Tp^{Br3}Cu$ catalyst precursor with $H_2O_2$: the oxo, superoxo and hydroperoxo copper species (Scheme 7.3).[309,310] These oxidized species feature tetrahedral coordination geometry around the metal center, with the trispyrazolylborate ligand coordinated in a $\eta^3$ fashion. Likewise, the catalyst precursor also presents a tetrahedral arrangement, with an acetonitrile molecule capping the vacant position, although this was not included in our theoretical model.

**Scheme 7.3:** Possible copper active species considered in this study, namely: oxo, superoxo and hydroperoxo, from left to right.

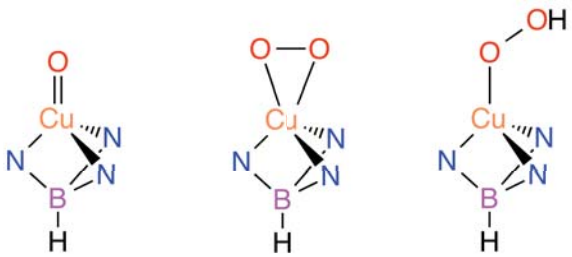


The stability of the oxo, superoxo and hydroperoxo copper species was calculated as well as their reactivity with benzene, outlined in the next sections, in order to clarify the nature of the active species. We started by investigating the stability and reactivity of the metal-oxo species since it has

been proposed as active species in several catalytic systems[125,311] and also characterized for a few metal-ligand combinations able to provide enough stability to the system. Moreover, as it has been discussed in the experimental section, no changes were observed when replacing the oxidant, hydrogen peroxide, by oxone, which does not yield peroxidic species. For these reasons, theoretical investigations gave preferential attention to the oxo complexes as potential active species than to the superoxo and hydroperoxo ones.

Figure 7.4 shows the reaction profile for the formation of the oxo species. The mechanism proposed starts with the coordination of $H_2O_2$ to the metal center, leading to the **O-S-I1** intermediate, which lies 7.0 kcal·mol$^{-1}$ above the separated reactants due to the unfavorable entropy factor. In order to oxidize the metal center from formal Cu(II) to Cu(III), **O-S-I1** undergoes spin crossover from the singlet to the triplet spin state through the minimum energy crossing point **MECP1**, which corresponds to the highest energy point in the reaction profile, 24.0 kcal·mol$^{-1}$. The relaxation of the **MECP1** in the triplet state entails the O–O bond cleavage and results in the formation of Cu(III) bis-hydroxo species, **O-T-I1**, which is similar to the catalytic species recently reported by Mayer and Golberg for the water oxidation reaction.[71] Subsequently, by intramolecular proton transfer from one hydroxo ligand to the other, **O-T-I1** is transformed into a copper-oxo-aqua intermediate, **O-T-I2,** through the low lying transition state **O-T-TS1**. At the end, the water molecule decoordinates from the metal center, giving rise to the oxo active species.

The copper-oxo active species, **cat-oxyl**, corresponds to a triplet in its ground state, since its reoptimization in the singlet state results in an increase of 27.2 kcal·mol$^{-1}$. Thus, it is more consistent to describe it as a radical Cu(II) $-O^{\cdot}$ species, referred to as oxyl, rather than as a closed shell oxo, Cu(III)=O. The oxyl configuration is well reflected by the spin density of **cat-oxyl**, with local spin densities of 0.80 and 1.11 a.u. on Cu and O, respectively.

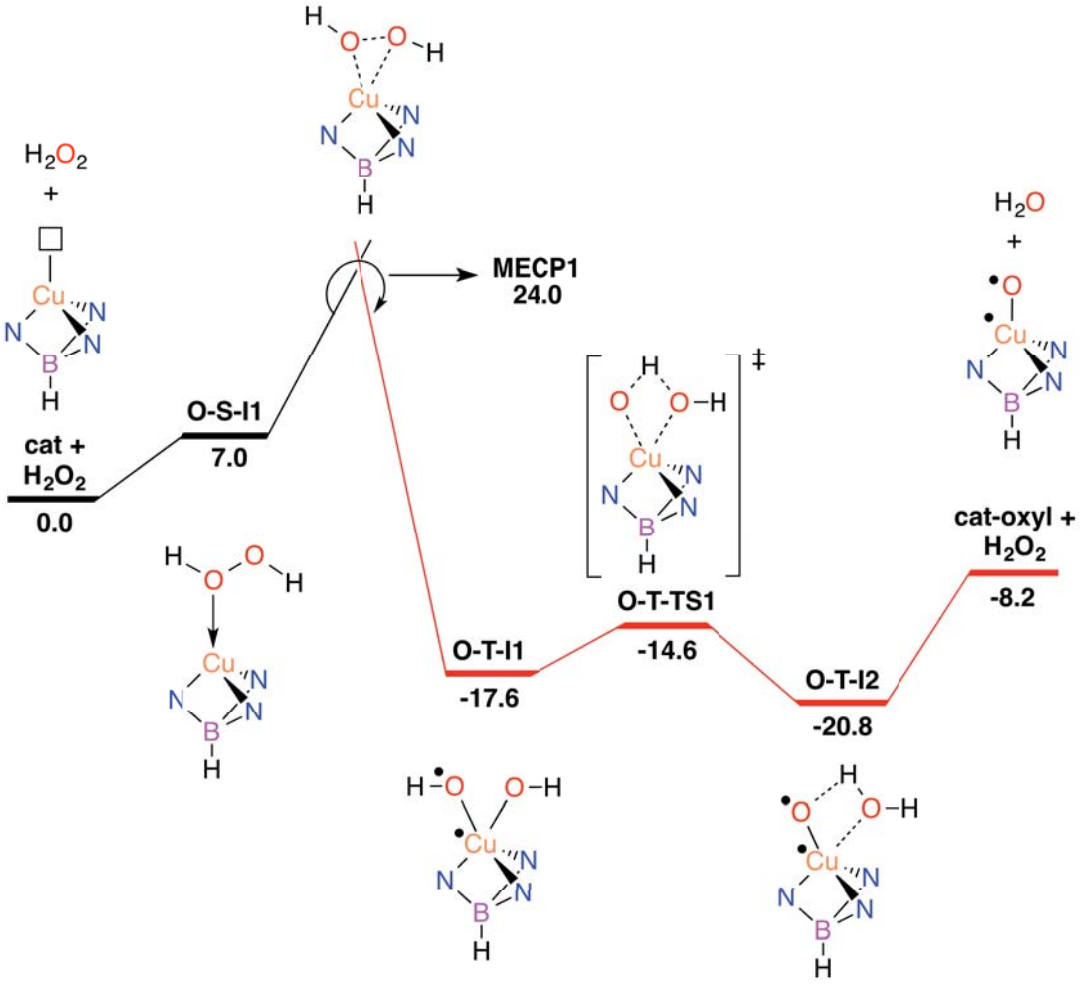


**Figure 7.4:** Gibbs energy ($\Delta G_{sol}$) profile, in kcal·mol$^{-1}$, for the generation of the oxo species in the singlet (black) and triplet (red) spin states. □ = vacant site.

### 7.4.2. Reaction Mechanisms

#### 7.4.2.1. Electrophilic Aromatic Substitution ($S_EAr$) on Benzene

Once the postulated active species has been characterized, we started by computing the reaction pathway associated to benzene oxidation by means of a $S_EAr$-like mechanism (Figure 7.5).

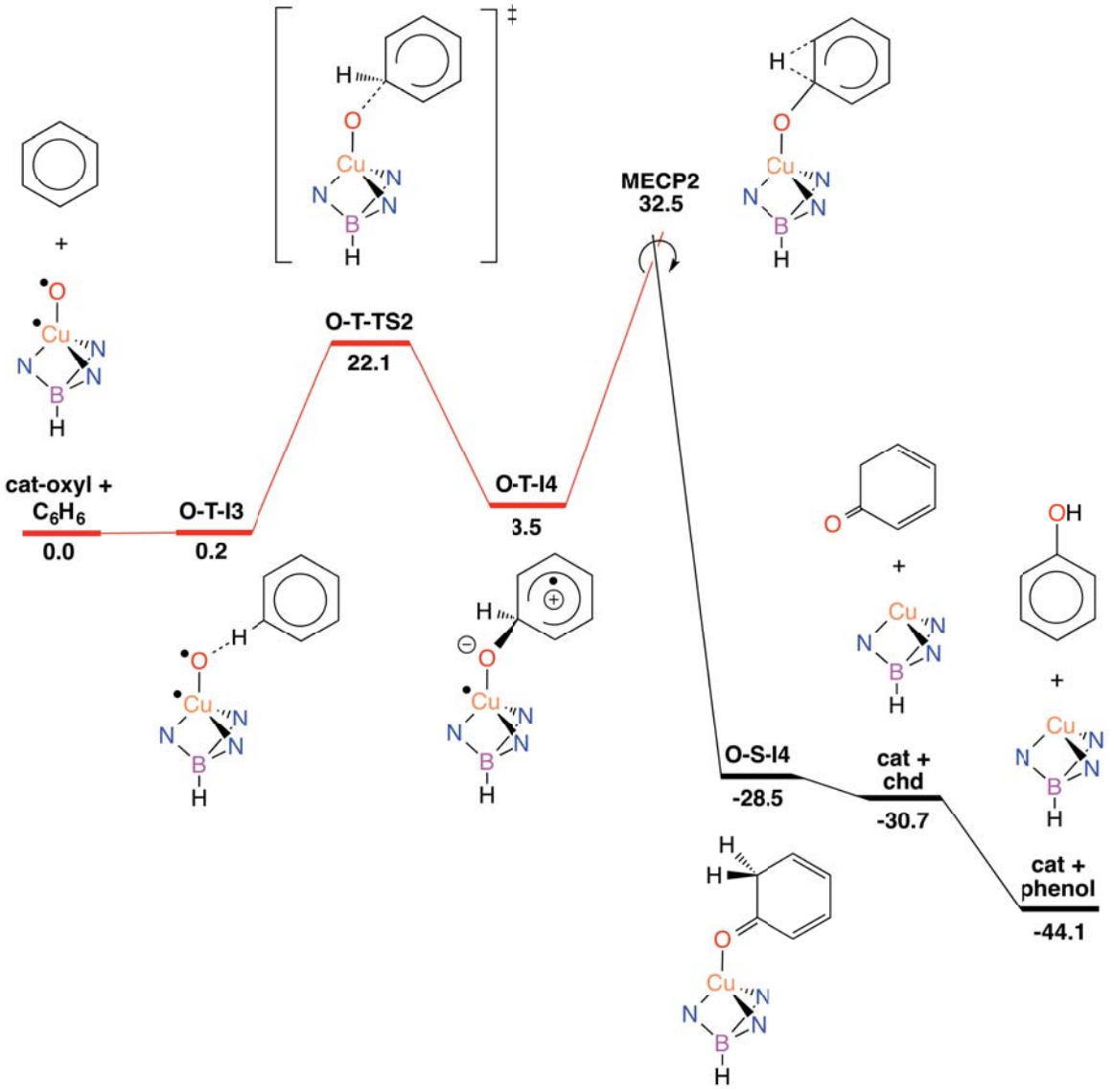


**Figure 7.5:** Gibbs energy ($\Delta G_{sol}$) profile, in kcal.mol$^{-1}$, of the S$_E$Ar mechanism in the triplet (red) and singlet (black) states.

The reaction starts with a weak H-bond interaction, d(CH···O) = 2.582 Å, between the substrate and the **cat-oxyl** species, **O-T-I3**, which is almost isoenergetic with respect to the separated reactants. This pre-reaction complex evolves through **O-T-TS2**, a significantly high transition state lying at 22.1 kcal·mol$^{-1}$ above the separated reactants in gas phase, in which the oxyl is starting to form a new C–O bond with benzene, d(C···O) = 1.889 Å (Figure 7.6). The relaxation of **O-T-TS2** by means of IRC calculations connects this transition state to intermediates **O-T-I3** and **O-T-I4**. In the products side, **O-T-I4,** the substrate appears bound to copper through the

oxyl leading to a Wheland-type intermediate[312]. This complex features a zwitterionic character, with the **cat-oxyl** and benzene fragments negatively and positively charged, respectively; $q(C_6H_6)= -q(CuOTp^{*,Br}) = 0.29$ a.u.

The generation of phenol from **O-T-I4** requires transferring the hydrogen atom from the *ipso* carbon to oxygen. In fact, in the typical $S_EAr$ mechanism the Wheland-type intermediate loses a proton to regenerate the aromatic stabilization, however, despite numerous attempts, no transition state could be located for this process. In contrast, the reoptimization of **O-T-I4** in the singlet state, **O-S-I4**, yielded 1,3-cyclohexadienone coordinated to the copper in a $\eta^1$-O fashion (Figure 7.6), which involves the migration of the hydrogen atom from the $sp^3$ to an $sp^2$ carbon atom. This suggested that triplet to singlet spin-crossover (**MECP2**) is needed to trigger the oxidation of the substrate and to recover the Cu(I) catalyst in its ground state (Figure 7.6). From now on, in order to simply the nomenclature we will refer to this mechanism simply as $S_EAr$.

Finally, 1,3-cyclohexadienone decoordination and isomerization to the most stable aromatic phenol make the overall reaction very exoergic by 44.1 kcal·mol$^{-1}$. The keto-enol tautomerization taking place in the last step has been well characterized experimentally as an extremely fast and exoergic process in polar solvents.[313,314]

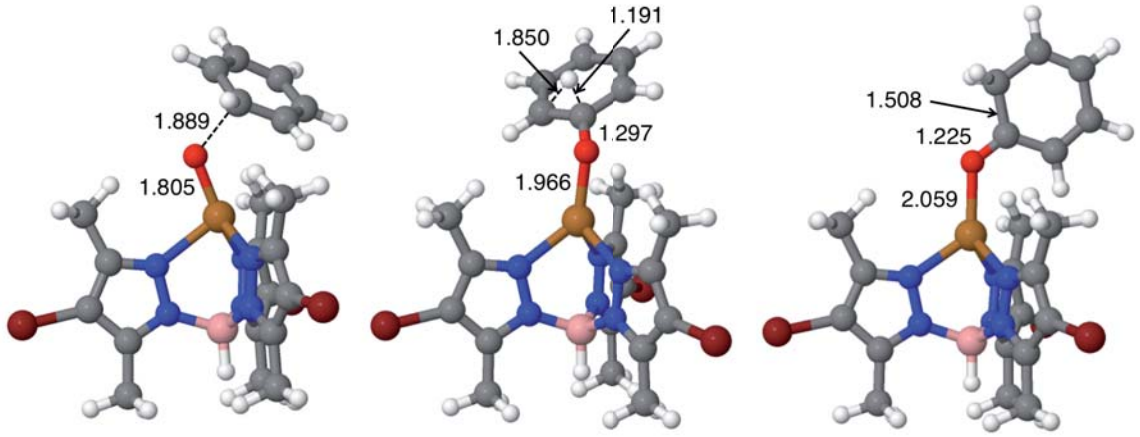


**Figure 7.6:** Optimized geometries of **O-T-TS2**(left) and **MECP2**(middle) and **O-S-I4**(right) on the $S_EAr$ pathway. Color code: orange = Cu, blue = N, red = O, pink = B, maroon = Br, gray = C, white = H. Selected bond distances for all the species involved in the $S_EAr$ reaction pathway are given in the Appendix (Table A7.1).

The **MECP2** is the highest energy point in the entire reaction profile (32.5 kcal·mol$^{-1}$), which could be slightly lowered by factors not considered in this model due to their complexity and computational cost, such as tunneling and explicit solvation of the H transferred. However, the involvement of high-energy reaction pathways is consistent with the low conversions obtained experimentally in the oxidation of benzene (8.0% in 4h at 60°C; see Table 7.1).

The data given in Tables 7.2 and 7.3 reflect the charge and spin density redistribution along the triplet-singlet spin states of the reaction pathway. In the initial addition step, the evolution of the local spin densities from **O-T-I3** ($\rho(O)$ = 1.11 a.u., $\rho(C_6H_6)$ = 0.00 a.u.) to **O-T-I4** ($\rho(O)$ = 0.14 a.u., $\rho(C_6H_6)$ = 0.95 a.u.) shows that one of the π electrons of benzene pairs with the single electron on oxygen (oxyl) yielding the C–O bond and a phenyl radical. The metal center does not participate in this electron rearrangement, as shown by the high but invariant values of ρ(Cu) on **O-T-I3**, **O-T-TS2** and **O-T-I4** (Table 7.3). A similar role is played by the $Tp^{*,Br}$ ligand, which has low but also invariant ρ values, consistent with a redox-innocent behavior.[300] Overall, as it is reflected in Table 7.3, electron density flows from the $C_6H_6$ fragment to the metal complex, as the system evolves from **O-T-I3** to **O-S-I4**. This charge redistribution and the nature of the **O-T-I4** intermediate are thus consistent with a typical $S_EAr$ mechanism,[315] in which the aromatic ring acts as the nucleophile, while the catalyst acts as an electrophile.

**Table 7.2:** Selected local charges (q), in a.u., for the species involved in the $S_EAr$ pathway.[a]

| Species | q(Cu) | q(O) | $q(C_6H_5)$ | $q(Tp^{*,Br})$ |
|---|---|---|---|---|
| **O-T-I3** | 1.08 | -0.59 | 0.00 | -0.49 |
| **O-T-TS2** | 1.11 | -0.75 | 0.18 | -0.54 |
| **O-T-I4** | 1.13 | -0.90 | 0.29 | -0.52 |
| **O-S-I4** | 0.59 | -0.64 | 0.74 | -0.69 |

[a]q are not given for **MECP2** due to different values obtained in the singlet and triplet states.

**Table 7.3:** Selected spin densities (ρ), in a.u., for the species involved in the $S_EAr$ pathway.[a]

| Species | ρ(Cu) | ρ(O) | $\rho(C_6H_5)$ | $\rho(Tp^{*,Br})$ |
|---|---|---|---|---|
| **O-T-I3** | 0.79 | 1.11 | 0.00 | 0.10 |
| **O-T-TS2** | 0.78 | 0.78 | 0.36 | 0.08 |
| **O-T-I4** | 0.81 | 0.14 | 0.95 | 0.10 |
| **O-S-I4** | 0.00 | 0.00 | 0.00 | 0.00 |

[a]ρ are not given for **MECP2** due to different values obtained in the singlet and triplet states.

### 7.4.2.2. Electrophilic Aromatic Substitution ($S_EAr$) on Substituted Benzenes

The $S_EAr$ mechanism was fully recomputed for *para*-substituted benzenes, Ph-X (X = $CF_3$, $NO_2$, Cl, Me, OMe, $NMe_2$). The Wheland-type intermediate found for benzene, **O-T-I4**, is also formed with all substituted Ph-X substrates. The local charges and spin densities on the $C_6H_5X$ fragment are in agreement with a radical-cation, with values of charge and spin density ranging from 0.26 to 0.30 a.u. and from 0.93 to 0.97 a.u., respectively. In the same way as benzene, the formation of **O-T-I4** is moderately endoergic for most X substituents, with the exception of X = $NO_2$, as shown the Gibbs energies of this intermediate relative to reactants (Table 7.4). Furthermore, these energy values show that the most demanding step is the triplet-to-singlet spin crossover, as in the case of benzene (**O-T-I4** → **MECP2** → **O-S-I4**), except for $NMe_2$. In this particular case the energy of the MECP2 decreases significantly so that, the **O-T-TS2** becomes the rate determining step. The energy barrier associated with the **MECP2** is therefore very sensitive to the nature of the substituent, ranging from a minimum of 16.4 kcal·mol$^{-1}$ (X = $NMe_2$) to a maximum of 35.4 kcal·mol$^{-1}$ (X = $NO_2$). Thus, the apparent trend point out that the reaction is accelerated by electron-donating groups ($\Delta G_{\mathbf{MECP2}}$ < 30 kcal·mol$^{-1}$ with X = Me, OMe and $NMe_2$) and slowed down by electron-releasing groups ($\Delta G_{\mathbf{MECP2}}$ > 30 kcal·mol$^{-1}$ with X = Cl, $NO_2$ and $CF_3$). This tendency is indeed a signature feature of a typical $S_EAr$ mechanism, in which there is an electronic flow from the substrate (nucleophile) to the catalyst (electrophile). In our catalytic system, this behavior is preserved, in spite of the unusual two-spin-states nature of the

reaction pathway.

**Table 7.4:** Gibbs energy in solution ($\Delta G_{sol}$), in kcal·mol$^{-1}$, of the $S_EAr$ mechanism for substituted benzenes. **O-S-I4** corresponds to 1,3-cyclohexadienone bound to the oxyl.

| Species | -$NMe_2$ | -OMe | -Me | -Cl | -$CF_3$ | -$NO_2$ |
|---|---|---|---|---|---|---|
| **O-T-I3** | -0.8 | -2.8 | 0.1 | 0.5 | 2.0 | 1.1 |
| **O-T-TS2** | 20.7 | 19.6 | 21.7 | 21.3 | 22.4 | 20.3 |
| **O-T-I4** | 2.5 | 0.9 | 1.6 | 0.6 | 3.2 | -1.9 |
| **MECP2** | 15.4 | 23.0 | 29.3 | 31.1 | 35.3 | 33.5 |
| **O-S-I4** | -24.4 | -29.9 | -25.7 | -23.9 | -23.9 | -25.1 |

It is noteworthy to mention, that the structure of **MECP2** depends strongly on the nature of the X substituent (Selected bond distances in Table A7.2). With X = $NO_2$, OMe and $NMe_2$, the spin crossover triggers the same chemical transformations observed for benzene (Figure 7.6), i.e. H-migration from the *ipso* to the *ortho* C atoms yielding 1,3-cyclohexadienone. In contrast, with X = Me, Cl and $CF_3$, the optimization of **MECP2** in the singlet state causes the addition of the O atom to the *ortho* C yielding benzene oxide, which is another tautomer of phenol (Figure 7.7). Nonetheless, these coordinated benzene oxide complexes are much less stable than their corresponding 1,3-cyclohexadienones bound to copper, around 30 kcal·mol$^{-1}$. In fact, it is well-known from the literature the rapid isomerization of arene oxides to phenols involving dienone intermediates.[316,317] Thus, for the sake of comparison, the energies of the **O-S-I4** intermediate with X = Me, Cl and $CF_3$ (Table 7.3) correspond to the reoptimization of **O-S-I4** with benzene by these groups.

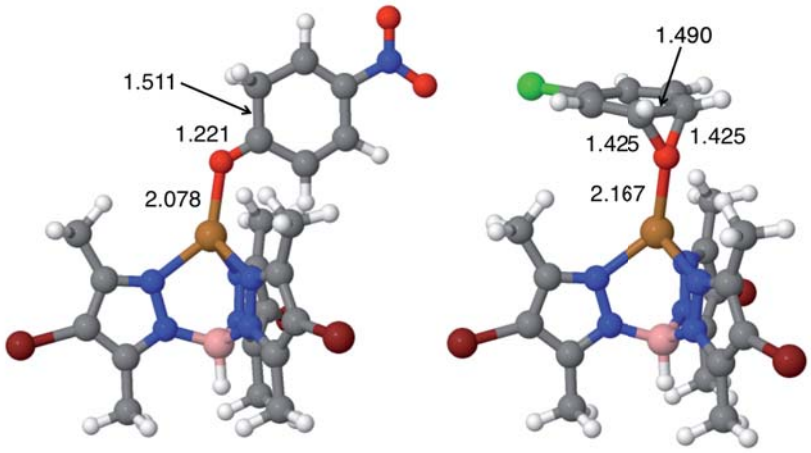


Figure 7.7: Optimized geometries of O-S-I4 for -$NO_2$ (left) and -Cl (right), which gave rise to 1,3-cyclohecadienone and benzene oxide respectively in the $S_EAr$ pathway. Color code: orange = Cu, blue = N, red = O, pink = B, maroon = Br, gray = C, white = H, green = Cl.

### 7.4.2.3. Rebound Mechanism on Benzene

The radical oxyl character of the Cu–O moiety in **O-T-I3** ($\rho$(O) = 1.11 a.u., Table 7.3) suggests that benzene may be also oxidized through a rebound mechanism initiated by H abstraction (Figure 7.8).[222] In this rebound mechanism the **cat-oxyl** species abstracts an H atom from benzene by following a single-step pathway in the triplet state, **O-T-I3** → **O-T-TS3** → **O-T-I5** (Figure 7.8). The C–H cleavage in the transition state **O-T-TS3** (Figure 7.9) yields **O-T-I5**, that corresponds to a phenyl fragment weakly bound to the [Cu(OH)(Tp*,Br)] complex, (d(O–H) = 0.95 Å). The $\Delta G$ for H abstraction, 5.3 kcal·mol$^{-1}$, shows that this step is more endoergic than the addition of benzene to the **cat-oxyl** moiety in the $S_EAr$ mechanism ($\Delta G$ = 3.5 kcal·mol$^{-1}$; Figure 7.5). In contrast, the energy barrier, $\Delta G^{\ddagger}$ = 17.0 kcal·mol$^{-1}$, is significantly lower than that of the benzene addition ($\Delta G^{\ddagger}$ = 22.1 kcal· mol$^{-1}$).

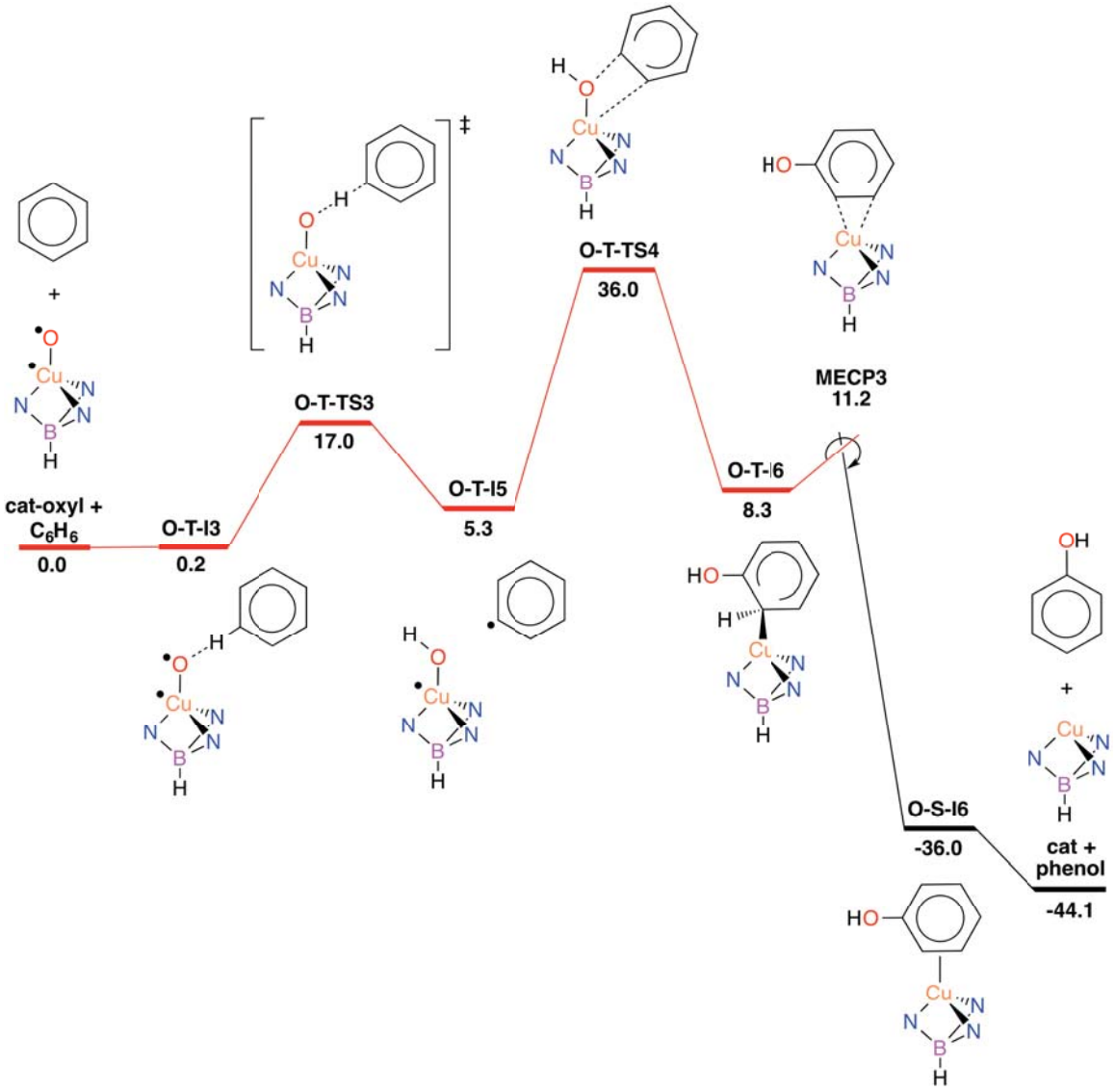


**Figure 7.8:** Gibbs energy ($\Delta G_{sol}$) profile, in kcal·mol$^{-1}$, of the Rebound mechanism in the singlet (black) and triplet (red) spin states.

H abstraction is followed by the rebound of the phenyl radical to the hydroxo ligand, **O-T-I5** → **O-T-TS4** → **O-T-I6** (Figure 7.8). In this transition state, the cleavage of the Cu–O bond is counterbalanced by the formation of the $C_{ipso}$–O bond, 1.79 Å (4.39 Å in **O-T-I5**). The full optimization of **O-T-TS4** (Figure 7.9) towards the products side yield intermediate **O-T-I6**, where the phenyl ring appears hydroxylated (d($C_{ipso}$–O) = 1.37 Å). This oxygen rebound step is endoergic and involves the highest energy barrier of the mechanism, with **O-T-I6** and **O-T-TS4** standing at 8.3 and 36.0 kcal·mol$^{-1}$ above the

separated reactants, respectively. The rebound mechanism is thus less favorable than the $S_EAr$, in which the most energy-demanding step involves an MECP at 32.5 kcal·mol$^{-1}$ above reactants (**MECP2** in Figure 7.5).

The intermediate yield by the rebound step, **O-T-I6**, showed an unexpected structural feature, i.e. the hydroxylated phenyl ring does not appear coordinated to the metal as a neutral phenol molecule. Instead, it coordinates as a formally anionic ligand through a single Cu–$C_{ortho}$ covalent bond (d = 2.03 Å), in which copper has a formal oxidation state of +2. This suggests that, likewise the $S_EAr$ mechanism, the reaction can only be completed by spin crossover to the singlet state. The MECP found for this process, **MECP3**, lies 11.2 kcal·mol$^{-1}$ above reactants (Figures 7.8). When the structure of **MECP3** is fully optimized in the singlet state, the system evolves towards the products side of the reaction by yielding the **O-S-I6** intermediate. The formation of this species is highly exoergic by 36 kcal·mol$^{-1}$ and corresponds to phenol coordinated in a $\eta^2$-fashion to the metal through the $C_{ortho}$=$C_{meta}$ moiety. Finally, the exoergic dissociation of **O-S-I6** leads to phenol and the catalyst precursor is recovered.

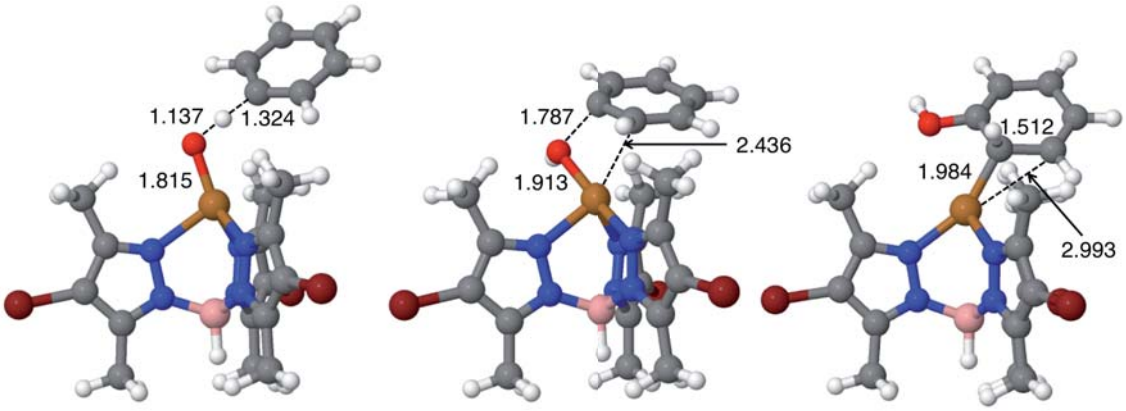


**Figure 7.9:** Optimized geometries of **O-T-TS3** (left), **O-T-TS4** (middle) and **MECP3** (right) on the rebound pathway. Color code: orange = Cu, blue = N, red = O, pink = B, maroon = Br, gray = C, white = H. Selected bond distances for all the species involved in the rebound reaction pathway are shown in the Appendix (Table A7.3).

The $C_6H_5^{\cdot}$ fragment in **O-T-I5** is well defined as a neutral phenyl radical by its local charge, $q(C_6H_5)$ = -0.01 a.u., and spin density, $\rho(C_6H_5)$ = 1.00 a.u. (Tables 7.5 and 7.6). The values of $\rho$(O) and $\rho(C_6H_5)$ in **O-T-TS3**, 0.62 and

0.56 a.u., respectively, show the homolytic nature of the C–H bond cleavage, with a single electron being transferred from the phenyl ring to the oxyl. In the rebound step, **O-T-I5 → O-T-TS4 → O-T-I6,** the spin density distribution does not change to any significant extent, thus one unpaired electron is located on copper and the other on the $C_6H_5$ fragment (Table 7.6). The ρ values for copper and the $Tp^{*,Br}$ ligand are almost constant along the reaction pathway, which indicate that these moieties are merely spectators in this process.

**Table 7.5:** Selected local charges (q), in a.u., for the species involved in the rebound pathway.[a]

| Species | q(Cu) | q(O) | q(H) | q($C_6H_5$) | q($Tp^{*,Br}$) |
|---|---|---|---|---|---|
| **O-T-I3** | 1.08 | -0.59 | 0.26 | -0.26 | -0.49 |
| **O-T-TS3** | 1.11 | -0.87 | 0.37 | -0.11 | -0.50 |
| **O-T-I5** | 1.13 | -1.10 | 0.48 | -0.01 | -0.50 |
| **O-T-TS4** | 1.15 | -0.94 | 0.50 | -0.20 | -0.51 |
| **O-T-I6** | 1.13 | -0.74 | 0.50 | -0.37 | -0.49 |
| **O-S-I6** | 0.64 | -0.72 | 0.51 | 0.25 | -0.68 |

[a]q are not given for **MECP3** due to different values obtained in the singlet and triplet states.

**Table 7.6:** Selected spin densities (ρ), in a.u. for the species involved in the rebound pathway.[a]

| Species | ρ(Cu) | ρ(O) | ρ(H) | ρ($C_6H_5$) | ρ($Tp^{*,Br}$) |
|---|---|---|---|---|---|
| **O-T-I3** | 0.79 | 1.11 | 0.00 | 0.00 | 0.10 |
| **O-T-TS3** | 0.80 | 0.62 | -0.07 | 0.56 | 0.09 |
| **O-T-I5** | 0.83 | 0.09 | 0.00 | 1.00 | 0.08 |
| **O-T-TS4** | 0.83 | 0.17 | 0.01 | 0.91 | 0.08 |
| **O-T-I6** | 1.00 | 0.03 | 0.00 | 0.90 | 0.07 |
| **O-S-I6** | 0.00 | 0.00 | 0.00 | 0.00 | 0.00 |

[a]ρ are not given for **MECP3** due to different values obtained in the singlet and triplet states.

### 7.4.2.4. Rebound Mechanism on Substituted Benzenes

The rebound pathway was also explored for all substituted Ph–X substrates (X = $CF_3$, $NO_2$, Cl, Me, OMe, $NMe_2$) (Table 7.7). The reaction pathway has the

same essential features observed with benzene, i.e. H abstraction yields a neutral phenyl radical, which undergoes rebound followed by triplet-to-singlet spin crossover. Furthermore, as for benzene, **O-T-TS4** involves the highest energy barrier ($\Delta G_{\mathbf{O\text{-}T\text{-}TS4}}$) of the rebound mechanism for all X substituents. Bond distances showed in Appendix (Table A7.4) show that these key transition states entail the rebound between the $C_{ipso}$ of the phenyl radical to the hydroxyl, accompanied by the binding of $C_{ortho}$ to copper.

Table 7.7: Gibbs energies in solution ($\Delta G_{sol}$), in kcal·mol$^{-1}$, with respect to separated reactants for the rebound mechanism with substituted benzenes.

| Species | -$NMe_2$ | -OMe | -Me | -Cl | -$CF_3$ | -$NO_2$ |
|---|---|---|---|---|---|---|
| **O-T-I3** | -0.8 | -2.8 | 0.1 | 0.5 | 2.0 | 1.1 |
| **O-T-TS3** | 16.9 | 14.5 | 16.9 | 16.9 | 17.2 | 16.8 |
| **O-T-I5** | 5.9 | 6.1 | 5.0 | 5.8 | 9.1 | 5.0 |
| **O-T-TS4** | 40.5 | 36.8 | 38.2 | 33.0 | 31.7 | 22.7 |
| **O-T-I6** | 10.8 | 6.5 | 9.8 | 5.6 | 5.5 | 10.0 |
| **MECP3** | 6.9 | 9.0 | 12.7 | 7.7 | 7.9 | 10.6 |
| **O-S-I6** | -36.1 | -35.8 | -34.3 | -34.7 | -33.3 | -41.2 |

It is important to realize that the dependence of $\Delta G_{\mathbf{O\text{-}T\text{-}TS4}}$ follows a trend opposite to that observed in the $S_EAr$ mechanism; i.e., the reaction is accelerated by electron-releasing groups and slowed down by electron-donating groups, which is not in agreement with the experimental data. These Gibbs energy barriers range from a minimum of 22.7 kcal·mol$^{-1}$ with X = $NO_2$ to a maximum of 40.5 kcal·mol$^{-1}$ with X = $NMe_2$. This trend is consistent with the local charges in the critical rebound step (Table 7.5), which grow for the phenyl radical (electrophile) and diminish for the oxyl radical (nucleophile). Indeed, the most electron-releasing groups of the series, X = $CF_3$ and $NO_2$, yield barriers even lower than those calculated for the $S_EAr$ mechanism. Therefore, theoretical results suggest that the operating mechanistic scheme ($S_EAr$ or rebound) might be conditioned by the electronic properties of the X substituent oriented in *para* position.

### 7.4.2.5. Benzene Oxidation by Superoxo and Hydroperoxo Species

In general, oxidized late transition metal complexes used to be extremely reactive and thus, difficult to isolate and characterize. Regarding to thermodynamics (Scheme 7.4), the formation of superoxo and hydroperoxo complexes turn out to be even more exergonic, -65.7 and -37.8 kcal·mol$^{-1}$, than the oxo, -8.2 kcal·mol$^{-1}$.

**Scheme 7.4:** Oxo, superoxo and hydroperoxo, from left to right. The vacant site in the coordination metal sphere is represented as □.The Gibbs energies are in kcal·mol$^{-1}$.

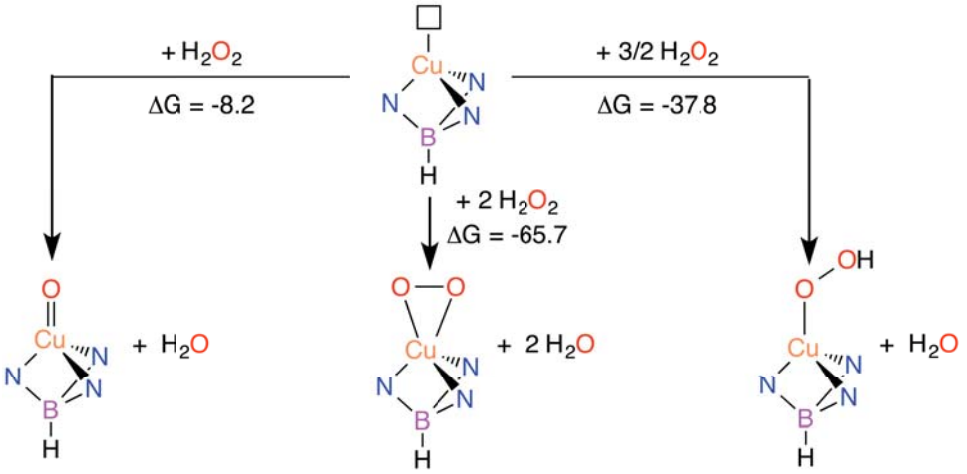


To explore the activity of superoxo and hydroperoxo species in benzene oxidation, we also computed the Gibbs energy profiles for these species. The superoxo species, which is a triplet in its ground state, can be added to one carbon atom of benzene ($S_EAr$) or abstract one hydrogen atom yielding the phenyl radical (rebound) (Figure 7.10). In contrast, the hydroperoxo species, which is a doubled in its ground state, evolves through a copper-oxygen addition into a C=C bond from benzene (Figure 7.11).

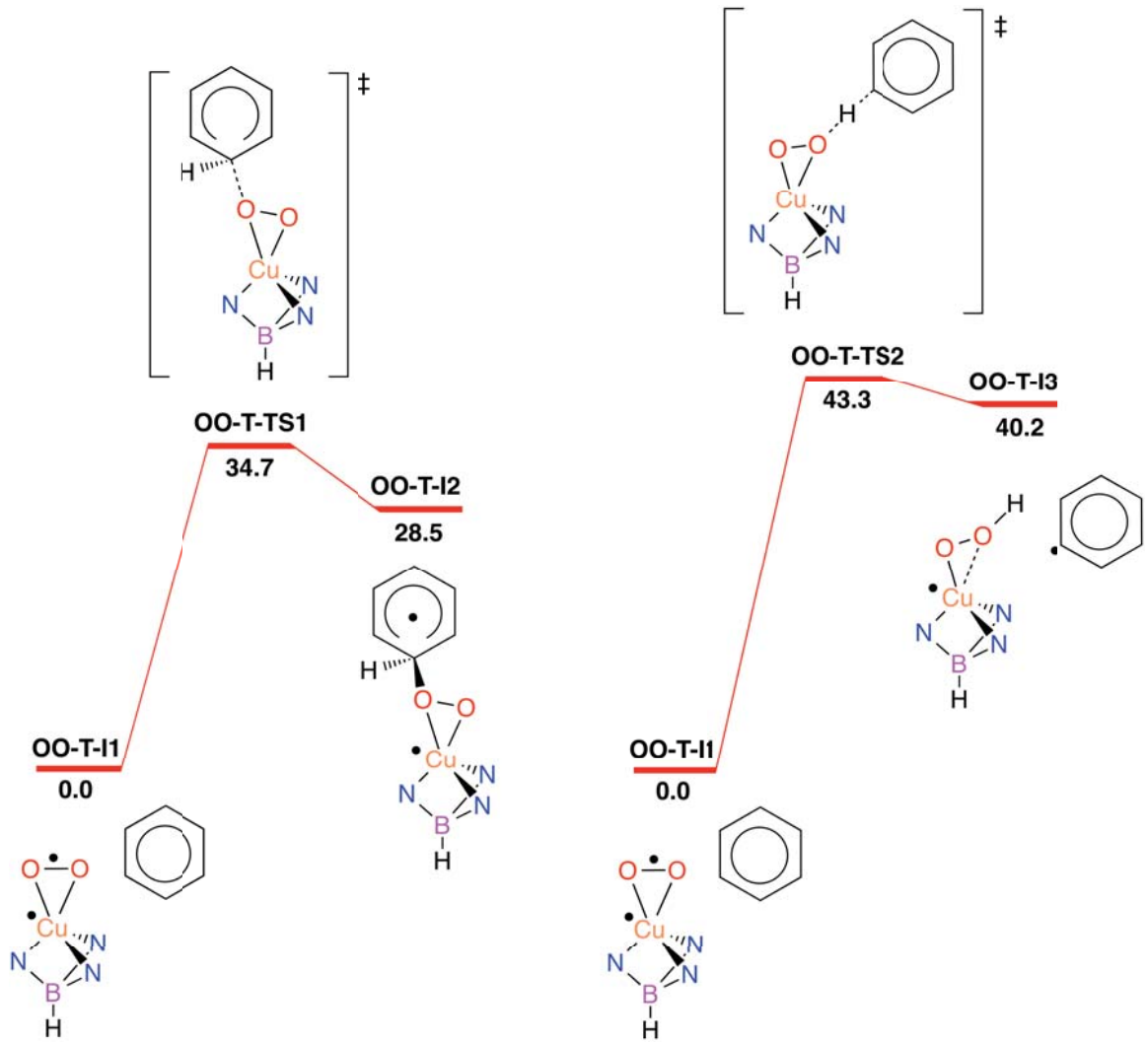


**Figure 7.10:** Gibbs energy ($G_{sol}$) profiles, in kcal·mol$^{-1}$, for the oxidation of benzene by superoxo species by means of $S_EAr$ (left) and rebound (right) mechanisms.

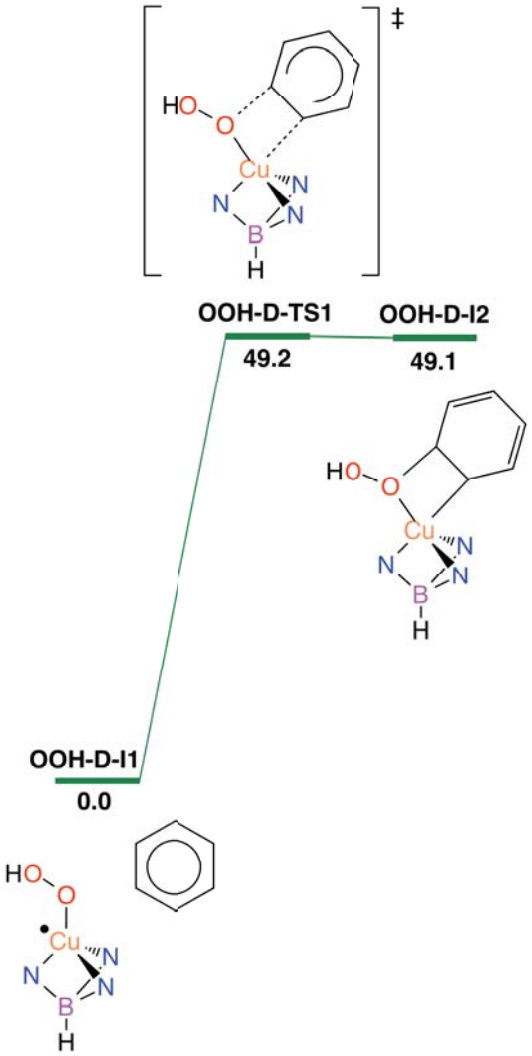


**Figure 7.11:** Gibbs energy ($G_{sol}$) profile, in kcal·mol$^{-1}$, for the oxidation of benzene by hydroperoxo species via copper-oxygen addition into the C=C bond.

The barriers associated to benzene oxidation by the superoxo (34.7 and 43.3 kcal·mol$^{-1}$) and hydroperoxo (49.2 kcal·mol$^{-1}$) species are all higher than that of the oxo (32.5 kcal·mol$^{-1}$; Figure 7.5). These results suggest that the superoxo and hydroperoxo complexes, although being thermodynamically more stable than the oxo, are less reactive in the C–H oxidation of benzene, which is in agreement with similar systems previously reported.[310,318]

## 7.5. Discussion and Conclusions

Experiments and theoretical calculations were carried out in parallel to propose a plausible mechanism for the copper-catalyzed $sp^2$ C–H oxidation of benzene. As a result, additional experiments and calculations along the course of this study were motivated by previous theoretical and experimental results, respectively.

Based on the same results obtained in the experiments replacing hydrogen peroxide by oxone, our experimental collaborators suggested a mono-oxygenated copper complex as catalytic active species. This was later confirmed by means of DFT calculations, since superoxo and hydroperoxo species proved to be less reactive towards benzene hydroxylation. Therefore, the **cat-oxyl** species was proposed to be the main responsible for the C–H bond oxidation of benzene.

In order to understand this oxidation process in terms of its reaction mechanism, several substituted benzenes were tested experimentally and theoretically. The experimental Hammett plot supported a typical electrophilic aromatic substitution mechanism, which does not involve radical intermediates. Nonetheless, the observation of small amounts of halobenzenes, after the addition of radical traps, puzzled the experimentalists. Hence, to gain insight into the hydroxylation reaction pathway, we explored computationally via an electrophilic aromatic substitution and rebound the reaction mechanism.

Based on the theoretical results, the $S_EAr$ mechanism proposed in this work is not the conventional one, since it requires spin crossover after the addition step. Nonetheless, it follows the expected trend of being accelerated by electron-donating groups and decelerated with electron-releasing groups, which is in line with the experimental reaction yields. Conversely, the rebound mechanism follows the opposite trend, although it accounts for the formation of halobenzenes derived from the $C_6H_5^{\cdot}$ radical intermediate. Indeed, the generation of this radical species in small amounts can be justified by the similar rate determining energy barriers achieved in both pathways for benzene (32.5 kcal·mol$^{-1}$ in the $S_EAr$ and 36.0 kcal·mol$^{-1}$ in the rebound).

It is important to realize that the $S_EAr$ mechanism involves the lower energy barriers for almost all substituted benzenes, except in the case of the most electron-releasing groups, $NO_2$ and $CF_3$, in which the rebound mechanism seems more favorable. This means that the operating mechanistic scheme is very susceptible to the electronic properties of the X substituent oriented in *para* position. Moreover, the fact that rebound mechanism becomes favorable in the case of $NO_2$ and $CF_3$ substituents indicates that the benzyl radical content should be higher than for the unsubstituted benzene. It was tested experimentally by adding radical traps, although no clear evidences were extract due to the lower yields of the hydroxylated product obtained in these cases.

## Appendix

**Table A7.1:** Selected bond distances, in Å, for the species involved in the EAS pathway.

| Species | Cu–O | $C_{ipso}$–O | $C_{ipso}$–H | $C_{ortho}$–H | $C_{ipso}$–$C_{ortho}$ | $C_{ortho}$–O |
|---|---|---|---|---|---|---|
| **O-T-I3** | 1.807 | 3.387 | 1.078 | 2.138 | 1.388 | 4.468 |
| **O-T-TS2** | 1.805 | 1.889 | 1.075 | 2.151 | 1.421 | 2.557 |
| **O-T-I4** | 1.810 | 1.398 | 1.102 | 2.105 | 1.501 | 2.385 |
| **MECP2** | 1.966 | 1.297 | 1.191 | 1.827 | 1.471 | 2.404 |
| **O-S-I4** | 2.059 | 1.225 | 2.109 | 1.091 | 1.508 | 2.358 |

**Table A7.2:** Selected bond distances, in Å, for **MECP2** in the EAS pathway with PhX.

| -X | Cu–O | $C_{ipso}$–O | $C_{ipso}$–H | $C_{ortho}$–H | $C_{ipso}$–$C_{ortho}$ | $C_{ortho}$–O |
|---|---|---|---|---|---|---|
| **-$NMe_2$** | 1.947 | 1.347 | 1.122 | 2.049 | 1.493 | 2.390 |
| **-OMe** | 1.977 | 1.317 | 1.155 | 1.933 | 1.483 | 2.408 |
| **-Me** | 1.935 | 1.410 | 1.088 | 2.184 | 1.467 | 1.907 |
| **-Cl** | 1.942 | 1.413 | 1.086 | 2.187 | 1.467 | 1.856 |
| **-$CF_3$** | 1.934 | 1.417 | 1.085 | 2.191 | 1.469 | 1.832 |
| **-$NO_2$** | 1.918 | 1.290 | 1.281 | 1.447 | 1.460 | 2.420 |

**Table A7.3:** Selected bond distances, in Å, for the species involved in the Rebound pathway.

| Species | Cu–O | $C_{ipso}$–H | O–H | $C_{ipso}$–O | Cu–$C_{ortho}$ | Cu–$C_{meta}$ |
|---|---|---|---|---|---|---|
| **O-T-I3** | 1.807 | 1.078 | 2.574 | 3.386 | 4.128 | 5.125 |
| **O-T-TS3** | 1.815 | 1.324 | 1.137 | 2.457 | 4.042 | 5.378 |
| **O-T-I5** | 1.807 | 4.092 | 0.952 | 4.391 | 6.561 | 6.669 |
| **O-T-TS4** | 1.913 | 2.302 | 0.958 | 1.787 | 2.436 | 3.333 |
| **O-T-I6** | 3.137 | 1.911 | 0.955 | 1.365 | 2.032 | 2.951 |
| **MECP3** | 2.870 | 1.923 | 0.956 | 1.376 | 1.984 | 2.993 |
| **O-S-I6** | 3.902 | 1.906 | 0.954 | 1.349 | 2.363 | 2.488 |

**Table A7.4:** Selected bond distances, in Å, for **O-T-TS4** in the Rebound pathway with Ph-X.

| -X | Cu–O | $C_{ipso}$–H | O–H | $C_{ipso}$–O | Cu–$C_{ortho}$ | Cu–$C_{meta}$ |
|---|---|---|---|---|---|---|
| **-$NMe_2$** | 1.924 | 2.307 | 0.958 | 1.787 | 2.385 | 3.301 |
| **-OMe** | 1.921 | 2.307 | 0.958 | 1.785 | 2.388 | 3.306 |
| **-Me** | 1.916 | 2.308 | 0.958 | 1.790 | 2.414 | 3.318 |
| **-Cl** | 1.906 | 2.288 | 0.958 | 1.766 | 2.569 | 3.484 |
| **-$CF_3$** | 1.901 | 2.308 | 0.957 | 1.786 | 2.630 | 3.506 |
| **-$NO_2$** | 1.883 | 2.306 | 0.955 | 1.818 | 2.629 | 3.771 |

*"If you want to go fast, go alone. If you want to go far, go together "*

African proverb

# 8

# *Copper-Catalyzed Hydroxylation & Dehydrogenation of Alkanes*

The previous chapter showed the efficiency of copper complexes bearing trispyrazolylborate ligands in the direct hydroxylation of benzene to phenol. By using the same type of catalysts and hydrogen peroxide as stoichiometric oxidant, the oxidation of inert alkanes was also achieved. Specifically, the current computational investigation attempts to provide a detailed picture of the cyclohexane oxidation reaction pathway, explaining the hydroxilated/ dehydrogenated product mixtures observed experimentally.[319]

All the experiments in the present study were performed in the research group of Prof. Pedro Pérez at the University of Huelva.

## 8.1. Introduction

Among the catalysts described to date for dehydrogenation reactions, those based on iridium are the most active by far. Nevertheless, other transition metals complexes mimicking the desaturase enzymes have been also described. Que and co-workers[320] reported the stoichiometric reaction of a dinuclear iron-complex with cumene to yield α-methylstyrene as dehydrogenated product (Scheme 8.1a).[320] On the other hand, Crabtree, Eisenstein and co-workers first described the catalytic use of a manganese-based system for the dehydrogenation of dihydrophenanthrene with PhIO or oxone as oxidants, in a transformation driven by the aromatization of the final products (Scheme 8.1b).[125,321] Since then, other groups such as Yin and co-workers[322] employed manganese-based catalyst with oxone as oxidant to dehydrogenate dihydroanthracene (Scheme 8.1c).

**Scheme 8.1:** Dehydrogenated reactions previously reported in literature.

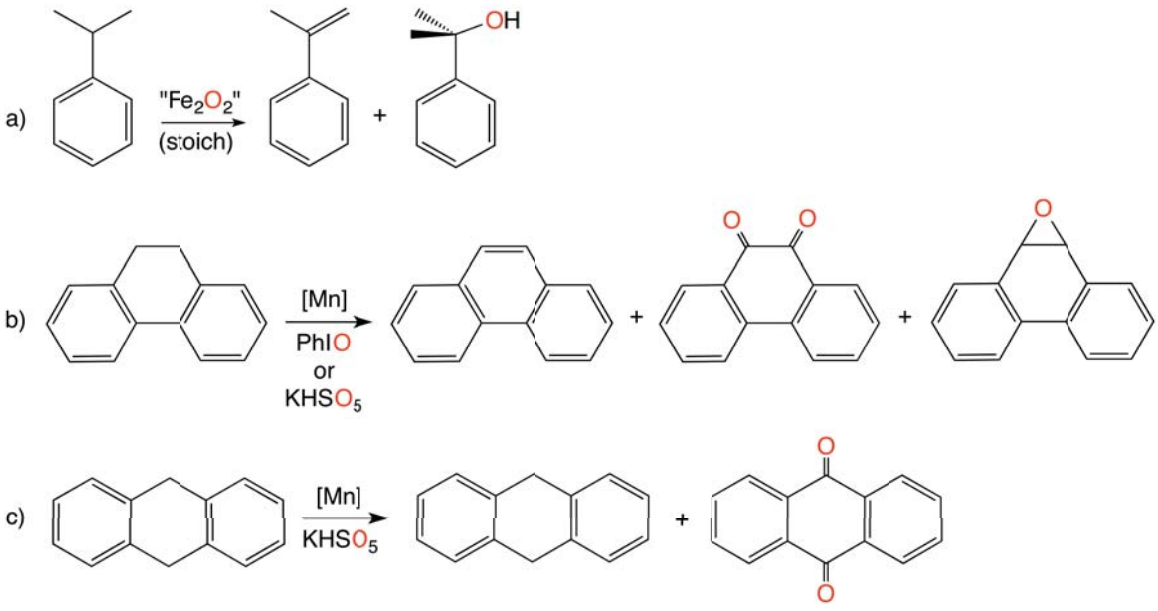


All the above-catalyzed reactions take place onto benzylic C–H bonds, which is an activated reaction site (bond dissociation energy of *ca.* 90 kcal·mol$^{-1}$)[323] and, additionally, in both manganese systems, aromatic products are finally formed. The dehydrogenation process is therefore more challenging in

substrates like cyclohexane or liner alkanes with non-activated C–H bonds (bond dissociation energies in the range of 96-100 kcal·mol$^{-1}$).[323]

Due to the catalytic potential of Tp$^x$Cu (Tp$^x$ = hydrotrispyrazolylborate) complexes[300] (Scheme 7.1) for the direct oxidation of benzene into phenol, the same system was used in the oxidation of alkanes. Although several hydrocarbons were investigated experimentally, theoretical calculations were performed only in the case of cyclohexane, as it provides a higher reaction yield and the best selectivities toward dehydrogenation products.

## 8.2. Experimental Results

In the first set of experiments, the cyclohexane oxidation reaction was tested using five copper complexes differing in the Tp$^x$ ligands (Table 8.1). Although with different ratios, cyclohexanol as well as cyclohexanone, derived from overoxidation of the former, were obtained in all cases as major products. Interestingly, two minor products were also identified by means of gas chromatography (GC) and gas chromatography - mass spectrometry (GC-MS) methods, which were assigned to cyclohexene and cyclohexene oxide (Figure 8.1).

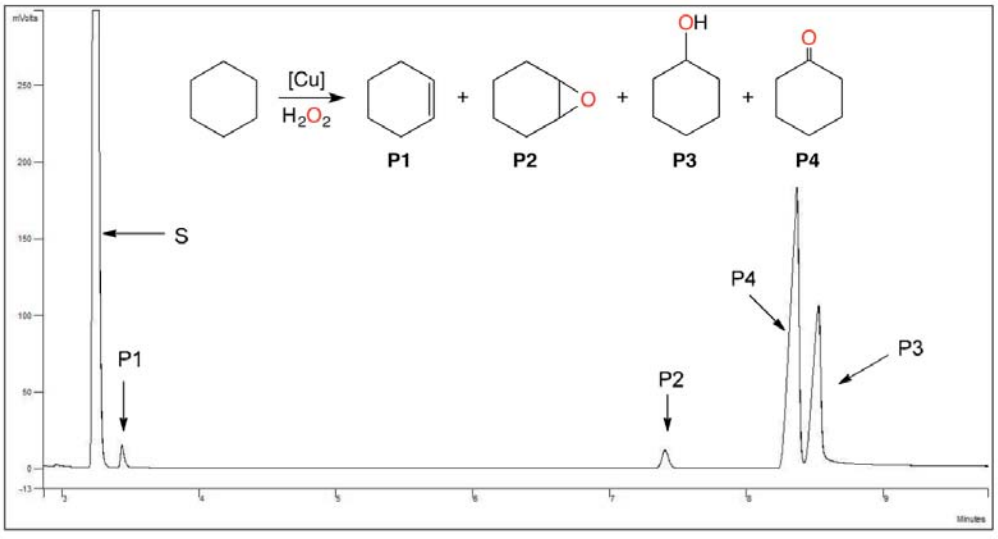


**Figure 8.1:** GC chromatogram of the product mixture in the Tp$^x$Cu catalyzed cyclohexane oxidation reaction.

**Table 8.1:** Yields and product distributions obtained in the cyclohexane oxidation with $H_2O_2$ using $Tp^xCu$ as catalysts. General conditions: 1 mmol of cyclohexane, 10 mmol of $H_2O_2$, 0.01 mmol of catalyst and 3 ml MeCN; reaction time = 1 h and temp = 60 °C. See Scheme 7.1 for ligand labels.

| | | | Dehydrog. prod.(%) | | Hydrox. prod. (%) | |
|---|---|---|---|---|---|---|
| Entry | Catalyst | Yield (%) | P1 | P2 | P3 | P4 |
| 1 | $Tp^{Br3}Cu$ | 22 | 4 | 3 | 45 | 48 |
| 2 | $Tp^{*,Br}Cu$ | 11 | 4 | 4 | 27 | 65 |
| 3 | $Tp^{*}Cu$ | 22 | 2 | 3 | 43 | 52 |
| 4 | $Tp^{Me2}$ | 21 | 1 | 3 | 43 | 53 |
| 5 | $Tp^{Ph}Cu$ | 13 | 4 | 2 | 39 | 55 |
| 6 | $Tp^{Br3}Cu^{a}$ | 24.5 | 3 | 2 | 38 | 57 |
| 7 | $Tp^{Br3}Cu^{b}$ | 20 | <1 | 2 | 56 | 41 |
| 8 | $Tp^{Br3}Cu^{c}$ | 11 | nd | 2 | 54 | 44 |
| 9 | $Tp^{Br3}Cu^{d}$ | 9 | 1 | 7 | 27 | 65 |

Yield values correspond to mmol of products/mmol of initial hydrocarbon.
Other conditions employed: [a]rt, 7h, [b]rt, 12h, [c]rt, 24h and [d]80°C, 1h.

From the ligands tested, $Tp^{Br3}Cu$ (entry 1) was chosen as the most suitable catalyst, since it provides the highest yields and amounts of dehydrogenation products. Additionally, for the $Tp^{Br3}Cu$ catalyst was observed that yield values decreased by increasing the reaction time from 7h to 12h and 24h (entries 6-8). This surprising trend was attributed to cyclohexane loss by diffusion into the vapor phase. In the same way, the reaction carried out at higher temperatures (entry 9) resulted in a decrease of the yield (entry 1).

The same protocol employed for cyclohexane oxidation was also applied for cyclooctane. Similarly, cyclooctene and cyclooctene oxide were obtained in small quantities, although only cyclooctanone appeared as major product with a reaction yield of 11% (Scheme 8.2).

**Scheme 8.2:** Product distribution obtained using the $Tp^{x}Cu$ catalytic system.

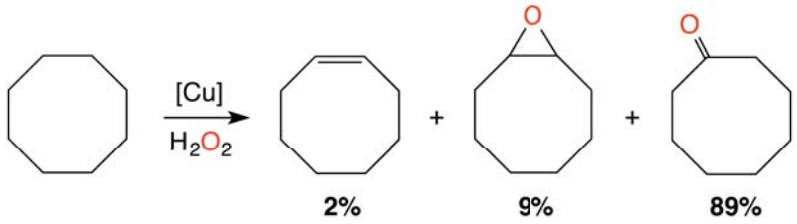


Even a much more challenging transformation is the dehydrogenation reaction of linear alkanes due to the low control over selectivity of these hydrocarbons. In particular, the oxidation of n-hexane was analyzed, following the same procedure as before and by using the same catalytic system, to infer whether n-hexene is formed in this reaction (Scheme 8.3). Indeed, the main outcome of the process concerned the functionalization of internal C–H bonds leading to hydroxylation products (P1 and P2) and their corresponding overoxidation derivatives (P3 and P4). Further, primary sites were also oxidized and thus 1-hexanal (P5) was detected as the result of 1-hexanol overoxidation. As regards the dehydrogenation reaction, 1-hexene (P6) was formed as the sole olefin in most experiments, although only in small amounts (Table 8.2).

**Scheme 8.3:** Detected Products in the oxidation of n-hexane with $H_2O_2$ and $Tp^{Br3}Cu$ as catalyst.

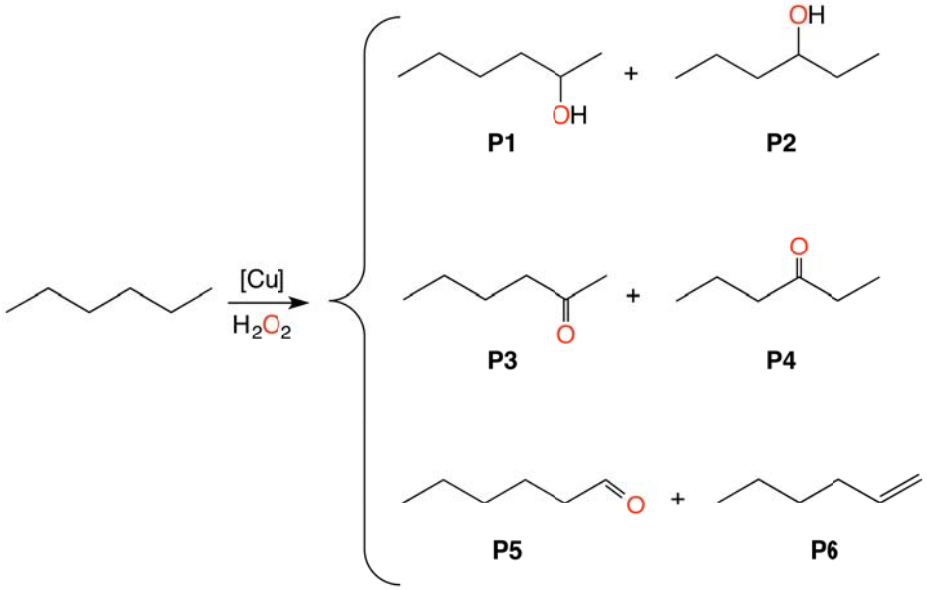

**Table 8.2:** Yields and product distributions obtained in the oxidation of n-hexane with $H_2O_2$ and $Tp^{Br3}Cu$ as catalyst. General conditions: 1 mmol of hexane, 0.01 mmol of catalyst and 3 ml MeCN; reaction time = 1 h and temp = 60°C. See Scheme 8.1 for ligand labels.

| Entry | mmol $H_2O_2$ | Yield (%) | P1 | P2 | P3 | P4 | P5 | P6 |
|---|---|---|---|---|---|---|---|---|
| 1 | 5 | 6.5 | - | - | 42 | 41 | 12 | 5 |
| 2 | 10 | 7 | - | - | 36 | 45 | 8 | 10 |
| 3[a] | 10 | 8.5 | 9 | 8 | 34 | 33 | 7 | 9 |
| 4[b] | 10 | 6.5 | - | 1 | 38 | 41 | 9 | >9 |
| 5[c] | 10 | 5 | - | 3 | 41 | 46 | 5 | 5 |

Yield values correspond to mmol of products/mmol of initial hydrocarbon. Other conditions employed: [a]rt, 3.5h, [b]rt, 5h and [c]rt, 12h.

Finally, for the sake of completeness, the oxidation of dihydroaromatic substrates previously described by Crabtree[125,321] and Yin[322] with manganese-based catalysts (Scheme 8.1b and 8.1c), was also evaluated with the $Tp^{Br3}Cu$ catalyst (Scheme 8.4). Both dihydrophenantrene and dihydroanthracene were dehydrogenated to give phenantrene (in 10% yield) and anthracene (in 27% yield) respectively, in addition to alcohol and ketone products.

**Scheme 8.4:** Distribution of products in the dihydrophenanthrene (top) and dihydroanthracene (bottom) oxidation reactions.

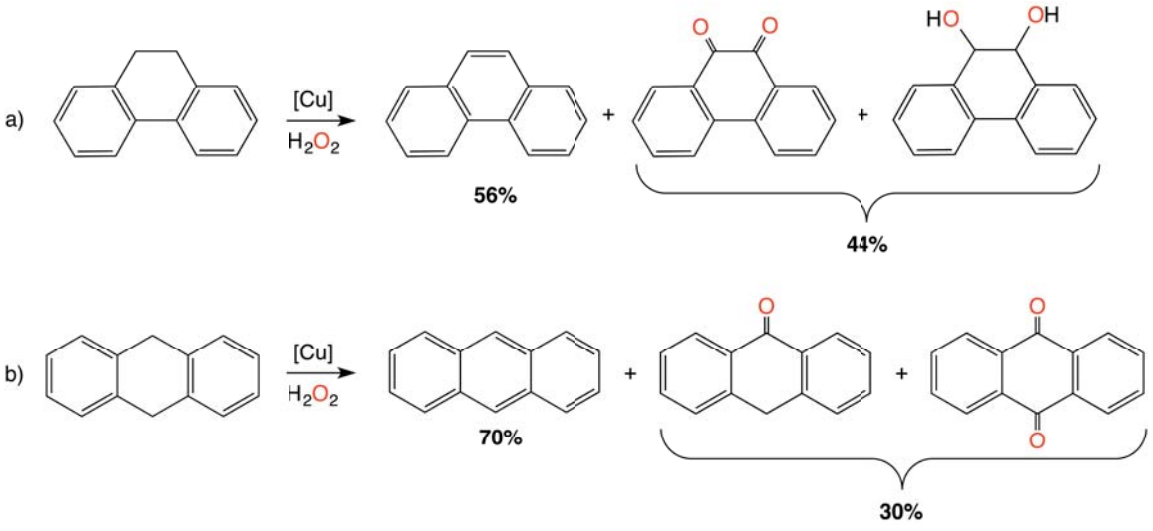

A series of experiments were carried out to get insight into the mechanism of these oxidation processes. A particular attention was given to investigate whether hydroxyl radical species were involved in our catalyzed reactions. In fact, the participation of these radicals, which abstract a hydrogen atom from the substrate in the key step of the mechanism, was previously proposed for the copper-catalyzed hydroxylation of cycloalkanes with other ligands (Scheme 8.5).[324,325] Subsequently, the cyclohexyl radical is trapped by molecular oxygen yielding the alkylperoxide radical, from which cyclohexanol and cyclohexanone are formed after several steps. Moreover, cyclohexylperoxide is also obtained under these conditions, giving rise to cyclohexanol upon the addition of $PPh_3$.[326]

**Scheme 8.5:** Previously proposed mechanism for the copper-catalyzed hydroxylation of cyclohexane.

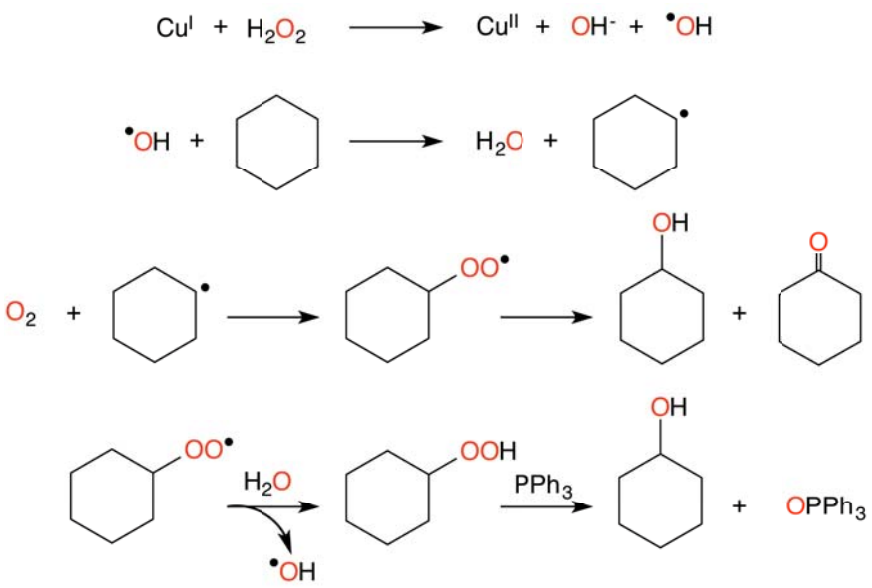


However, with the trispyrazolylborate ligand, no changes were observed upon varying the atmosphere from air to nitrogen, which should decrease the yield into oxidation products since $O_2$ is required for cycloalkylperoxide formation.[327] Moreover, the presence or absence of $PPh_3$ did not alter the catalytic results, which implies that no cycloalkylperoxides derived from the participation of the $OH^{\cdot}$ radicals are formed in our system. Thus, these data do not support the proposal of $OH^{\cdot}$ radicals as activating agents in the ongoing process.

Crucial information concerning the reaction mechanism was found when radical inhibitors were employed. When the cyclohexane oxidation reaction was carried out in presence of $CCl_4$, some cyclohexyl chloride was detected at the end of the reaction, which indicates the presence of cyclohexyl radicals in the oxidation reaction.

Overall, radical trapping experiments are in accordance with the participation of copper-oxyl complexes (Figure 7.4) in the oxidation of cyclohexane, which are the same active species proposed for the benzene to phenol conversion (see Chapter 7). In these experiments, the reaction of copper-oxyl with cyclohexane leads to the formation of cyclohexyl radicals, which are trapped by the addition of $CCl_4$. Hence, the current computational investigation attempts to provide a detailed picture of the cyclohexane oxidation reaction pathway that could explain the product mixtures observed experimentally.

## 8.3. Computational Details

All the calculations presented in this study were carried at the same level of theory employed in the previous chapter, i.e. DFT(BHLYP)[159,153] using the Gaussian09 program,[224] on the basis of the good agreement between theory and experiments obtained. However, MPWB1K[184] and M06-2X[170] functionals were also used to refine the critical energy difference between the minimum energy crossing points. These functionals have an amount of HF exchange (44% in MPWB1K and 54% in M06-2X) similar to that of BHLYP (50%) and were designed for an accurate description of dispersion forces.

Br and Cu atoms were described using the Stuttgard-Drensen effective core potential for the inner shell electrons and its associated triple-ζ basis set for the valence shell ones. The all-electron double-ζ 6-31G(d,p) basis set was used for H, B, C, N and O.

All stationary points were fully optimized in gas phase without any geometry or symmetry constrains. Harmonic frequencies were computed analytically at these optimized geometries to characterize them as either minima (reactants, intermediates and products) or saddle points (transition states). The latter were confirmed by having one imaginary frequency in the

Hessian matrix and by means of IRC calculations. These frequency calculations were also employed to determine the difference between the Gibbs and potential energies, $(G - E)_g$, which includes the zero-point, thermal and entropy corrections.

The effect of the solvent, acetonitrile (ε = 35.688), was estimated by means of CPCM[202] single-point calculations on the gas-phase optimized geometries, $E_{sol}$, with a larger triple-ζ 6-311+G(d,p) basis set on H, B, C, N and O. Therefore, the energies showed throughout this chapter correspond to Gibbs energies at 298 K in acetonitrile, $G_{sol}$, obtained by employing the following equation:

$$G_{sol} = (G - E)_g + E_{sol} \qquad [8.1]$$

Local charges and spin densities were obtained from Natural Population Analysis (NPA) calculations.[308] The minimum energy crossing points (MECPs) were located with the program developed by J. N. Harvey *et al.*[199] The nature of these points was confirmed by their full optimization in each of the two spin states involved in the crossing. The thermodynamic and solvent corrections associated with the MECP were evaluated by averaging the values found for each spin state minimum connected to it.

## 8.4. Theoretical Results

### 8.4.1. Reaction Mechanisms

As mentioned above, we focused on investigating the cyclohexane oxidation reaction pathway involving the copper-oxyl complex. Moreover, we also analyzed the catalytic potential of superoxo and hydroperoxo complexes for H abstraction from cyclohexane, which is discussed at the end of this section.

#### 8.4.1.1. Hydroxylation and Dehydrogenation of Cyclohexane with the Cu-Oxo Species

A plausible oxidation mechanism involving copper-oxyl as active species (Figure 7.4) is depicted in Figure 8.2. In the first step cyclohexane approaches to the copper-oxyl yielding intermediate **O-T-I1**, in which a C–H bond of the

substrate forms a weak H-bond to the oxygen ligand, d(H···O) = 2.562 Å.[311] The local spin densities (Figure 8.4 and Table 8.3) of this species show that the two unpaired electrons are localized on the copper and oxygen atoms, ρ(Cu) = 0.80 a.u. and ρ(O) = 1.11 a.u. This strong radical character localized on the oxygen atom[83,328] in **O-T-I1,** referred to as oxyl, may promote the homolytic cleavage of one C–H bond of cyclohexane.[125] In fact, in the transition state, **O-T-TS1** (Figure 8.3), located at a relative energy of 3.0 kcal·mol$^{-1}$ above the separated reactants, a C–H bond is broken, d(C···H) = 1.247 Å, and the hydrogen atom is transferred to the oxyl ligand, d(H···O) = 1.252 Å. The oxyl spin density is reduced to 0.68 a.u. due to its polarization toward the activated C–H bond, which gains radical character on its carbon atom, 0.47 a.u. This is consistent with the pairing of two electrons to form the new O–H bond, one coming from the oxyl and the other from the homolytic cleavage of the C–H bond. The relaxation of the **O-T-TS1** towards products converged into intermediate **O-T-I2,** which corresponds to a copper-hydroxo complex weakly associated with the $C_6H_{11}^{\cdot}$ organic fragment.

As it is reflected in the local charges and spin densities (Table 8.3), the $C_6H_{11}^{\cdot}$ moiety corresponds to a neutral cyclohexyl radical, with the spin density concentrated upon the carbon involved in the C–H cleavage, ρ(C) = 0.96 a.u. The generation of this radical species is consistent with the experimental formation of $C_6H_{11}Cl$ in the presence of $CCl_4$. Interestingly, concerning the metal and the $Tp^{Br3}$ ligand, they seem to play a spectator role, since their local charges and spin densities remain almost constant throughout the reaction.

A previous work by Crabtree, Eisenstein and co-workers[125] established the existence of two competing pathways involving the formation of a carbon-radical species, such as our cyclohexyl radical, which yield hydroxylation and dehydrogenated products. To put it briefly, the hydroxylation pathway was based on the coupling between the OH ligand and the organic radical, following a typical rebound mechanism, whereas the dehydrogenation pathway underwent a second H abstraction from the vicinal C–H bond. Thus, we tried to determine both pathways from the cyclohexyl radical to generate the corresponding hydroxilated and dehydrogenated products.

In order to obtain the hydroxylated product, a coupling between the OH

ligand and cyclohexyl radical should exist. Nonetheless, all attempts to optimize the transition state of this transformation in the triplet state led to high-energy non-converged geometries. To overcome this issue, the spin state of the **O-T-I2** intermediate was switched from triplet to singlet. The **O-T-I2** geometry was reoptimized to the singlet spin state obtaining the closed-shell **O-S-I2** Cu(I) $d^{10}$ species. The minimum energy crossing point associated with this spin crossover, **MECP1** (Figure 8.3), has a geometry very similar to that of the classical OH rebound transition state.[329,330] Specifically, in **MECP1** a carbon atom from the cyclohexyl radical approaches to the O atom of the OH ligand, d(C···O) = 2.361 Å, which results in an elongation of the Cu–O bond, d(Cu···O) = 1.823 Å (1.779 Å in **O-T-I2**). In the **O-S-I2** intermediate, the C–O bond is formed, d(C–O) = 1.432 Å, but the oxygen atom remains coordinated to the metal center, d(Cu–O) = 2.060 Å. In the last step, the cyclohexanol product is released and the catalyst precursor, $Tp^{Br3}Cu$, is regenerated.

Due to the presence of some radical character on the oxygen atom of the **O-T-I2** intermediate, ρ(O) = 0.10 a.u., dehydrogenation of cyclohexane may be promoted by means of a second H abstraction from the cyclohexyl ligand. This prompted the location of an alternative MECP leading to the formation of cyclohexene, **MECP2** (Figure 8.3). Indeed, the geometrical parameters of the new crossing point are consistent with the cleavage of the C–H bond, d(C···H) = 1.191 Å (1.093 Å in **O-T-I2**), and with the transfer of H to O, d(H···O) = 1.539 Å (2.663 Å in **O-T-I2**). Furthermore, this rearrangement also implies an elongation of the Cu–O bond to 1.86 (1.779 Å in **O-T-I2**) and the shortening of the C–C bond distance to 1.426 Å (1.493 Å in **O-T-I2**). The full optimization of **MECP2** onto the singlet spin state yield the **O-S-I3** intermediate, which corresponds to the decoordinated cyclohexene product, d(C=C) = 1.331 Å, and the catalyst precursor with a water molecule capping the vacant site.

Both hydroxylation and dehydrogenation reactions are very exergonic, -65.1 and -65.5 kcal·$mol^{-1}$, respectively. The energy landscape depicted in Figure 8.2 suggests that the reaction becomes irreversible after the spin crossover, which is determining the final reaction outcome. The rather small energy difference between **MECP1** and **MECP2**, 3.2 kcal $mol^{-1}$,

suggested that the reaction may yield mixtures of cyclohexanol and cyclohexene, with the former being the major product. Further energy refinement with the MPWB1K and M06-2X dispersion-corrected DFT functionals gave narrower energy differences of only 1.0 and 1.3 kcal·mol$^{-1}$, respectively, between the MECPs. These values are consistent with the hydroxylation:dehydrogenation ratio observed in the experiments, 93:7 at 60°C, which would correspond to an energy difference around 1.7 kcal·mol$^{-1}$. Dispersion forces thus play a role in the selectivity of this reaction. These forces may be related to weak non-covalent interactions between the C–H bonds of the cyclohexyl fragment and the bromide atoms of the trispyrazolylborate ligand.

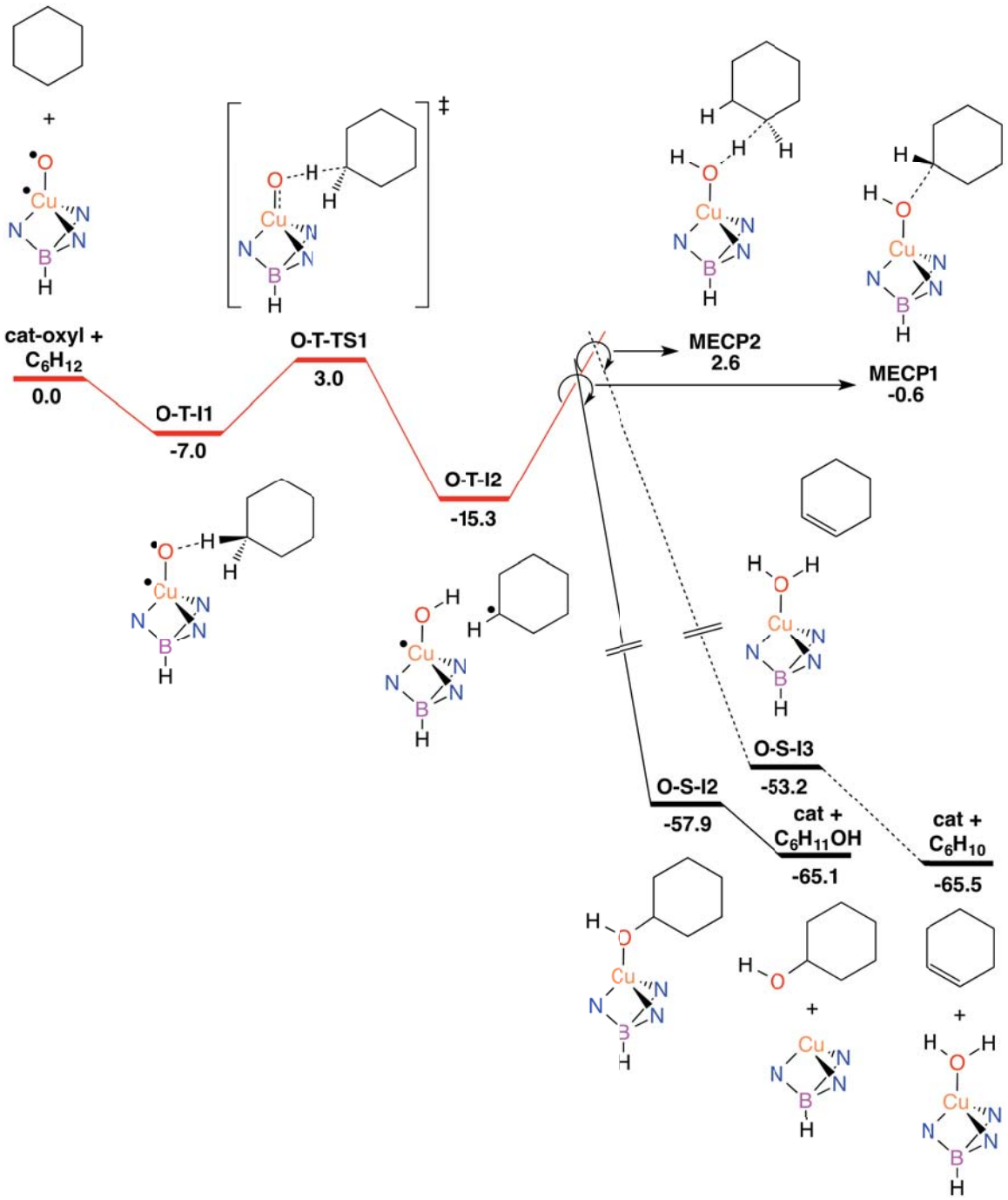


**Figure 8.2:** Gibbs energy ($G_{sol}$) profile, in kcal·mol$^{-1}$, for the hydroxylation (solid line) and dehydrogenation (dashed line) of cyclohexane. In black is represented the singlet spin state and in red the triplet.

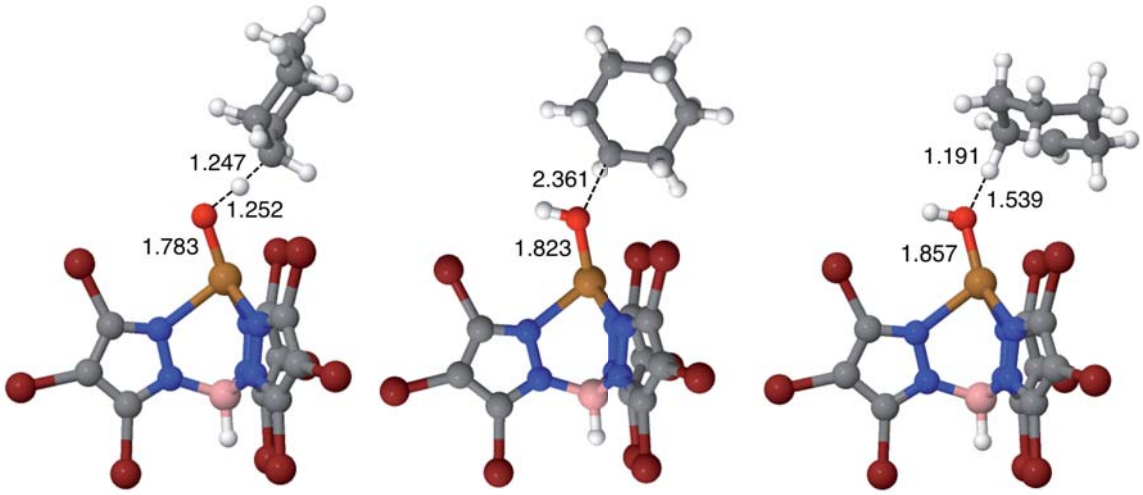


**Figure 8.3:** Optimized geometries of **O-T-TS1** (left), **MECP1** (middle), **MECP2** (right). Elements color code: orange = Cu, red = O, white = H, gray = C, blue = N, maroon = Br, pink = B.

**Table 8.3:** Local spin densities (ρ)[a] and charges (q), in a. u., of the stationary points involved in the hydrogen abstraction step.

| | **O-T-I1** | **O-T-TS1** | **O-T-I2** |
|---|---|---|---|
| ρ(Cu) | 0.80 | 0.81 | 0.84 |
| ρ(O) | 1.11 | 0.68 | 0.10 |
| ρ(C)[b] | 0.00 | 0.47 | 0.96 |
| ρ(H)[b] | 0.00 | -0.06 | -0.01 |
| ρ($C_6H_{11}$) | 0.00 | 0.48 | 0.97 |
| ρ($Tp^{Br3}$) | 0.09 | 0.09 | 0.10 |
| q(Cu) | 1.13 | 1.17 | 1.18 |
| q(O) | -0.65 | -0.94 | -1.14 |
| q(C)[b] | -0.38 | -0.23 | -0.09 |
| q(H)[b] | 0.21 | 0.29 | 0.47 |
| q($C_6H_{11}$) | -0.21 | -0.01 | 0.00 |
| q($Tp^{Br3}$) | -0.48 | -0.51 | -0.51 |

[a] Positive and negative spin densities are α and β.
[b] C and H belong to the activated C–H bond.

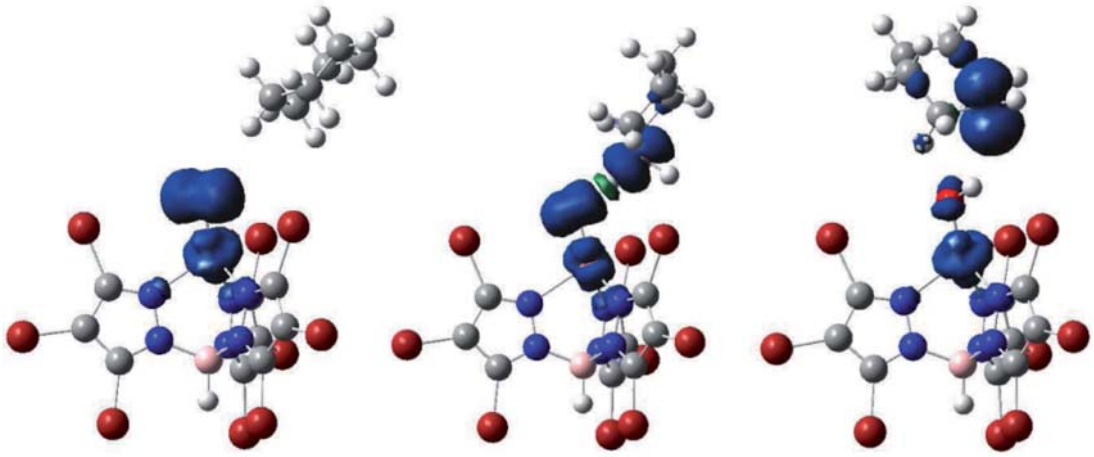

**Figure 8.4:** Spin densities of **O-T-I1** (left), **O-T-TS1** (middle) and **O-T-I2** (right). Spin density colors: blue = alpha, green = beta. Elements color code: orange = Cu, red = O, white = H, gray = C, blue = N, maroon = Br, pink = B

### 8.4.1.2. Hydroxylation and Dehydrogenation of Cyclohexane with Cu-Superoxo and Cu-Hydroperoxo Species

In order to confirm the validity of the copper-oxyl as active specie, we also computed the Gibbs energy profiles for the hydrogen abstraction of cyclohexane by the superoxo and hydroperoxo complexes (Figure 8.5). The superoxo species, which is a triplet in its ground state, abstracts one hydrogen atom from cyclohexane yielding cyclohexyl radical. In contrast, the hydroperoxo species, that is a doublet, promotes the reaction through a direct oxygen insertion concerted mechanism, inconsistent with the formation of the cyclohexyl radical suggested by the experiments. The barriers associated to the hydrogen abstraction from cyclohexane are considerably higher for the superoxo and hydroperoxo species, 32.4 and 27.3 kcal·mol$^{-1}$ (Figure 8.5), than for the oxyl one, 10.0 kcal·mol$^{-1}$ (Figure 8.2). These results suggest that the superoxo and hydroperoxo species, while being thermodynamically more stable than the oxyl (Scheme 7.3), are less reactive towards C–H oxidation, which is in agreement with other studies on similar systems previously reported.[310,318]

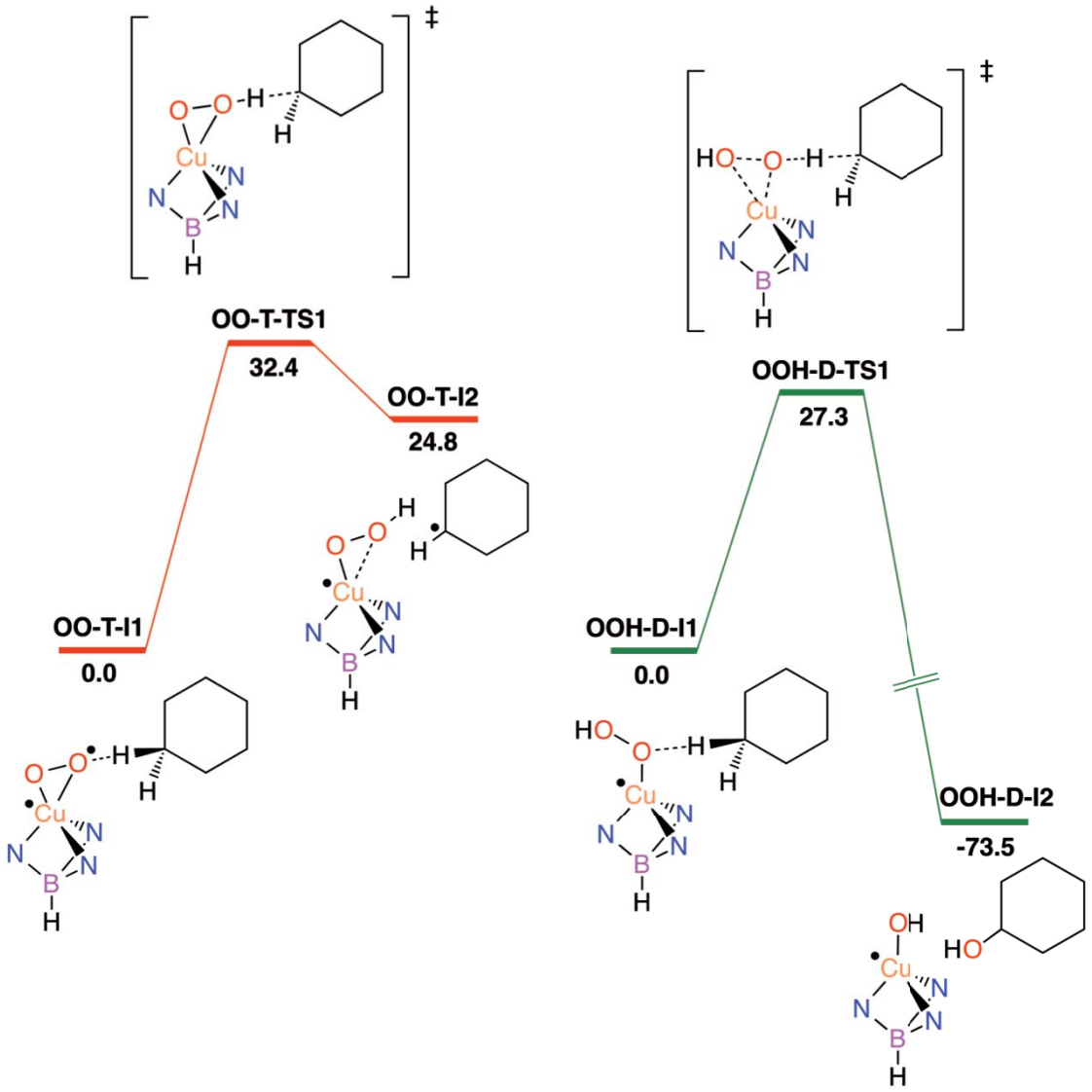


**Figure 8.5:** Gibbs energy ($G_{sol}$) profile, in kcal·mol$^{-1}$, for the oxidation of cyclohexane by superoxo (left) and hydroperoxo (right) species.

## 8.5. Discussion and Conclusions

On the basis of the experimental and theoretical data, a plausible mechanistic proposal for cyclohexane oxidation, in the presence of copper complexes bearing trispyrazolylborate ligands, has been presented. Despite the experimental data were presented first in the chapter, experiments and theoretical calculations were performed alongside each other. In fact, it is

noteworthy to mention that the dehydrogenated product was first proposed computationally before being detected experimentally in small quantities.

The catalytic capability of the copper-oxyl species has been attributed to the strong radical character in the oxygen atom. It enables an accessible hydrogen abstraction energy pathway yielding cyclohexyl radical and $Tp^xCu–OH$ intermediate. From here, two competitive pathways that involve spin crossover through MECPs of similar energy may occur, namely the hydroxylation and dehydrogenation of cyclohexane. This is consistent with the product mixture observed experimentally, that provides alcohols and the unprecedented dehydrogenated substrate.

In the hydroxylation pathway, the cyclohexyl radical adds to the $Tp^xCu–OH$ intermediate leading to cyclohexanol formation, whereas in the dehydrogenation pathway, a second hydrogen abstraction from the α C–H of the cyclohexyl radical gives rise to cyclohexene formation. In the latter case, the oxidant itself acts as hydrogen acceptor, with the net reaction providing two molecules of water from one molecule of hydrogen peroxide and cyclohexene. The hydroxylation pathway evolves through the lowest-energy MECP, which results in the formation of cyclohexanol as the major reaction product in agreement with the experiments.

The distribution of products obtained in the current study is similar to that found by Sawyer and co-workers,[331] with an iron-based catalyst, who also exclude the participation of hydroxyl radicals derived from Fenton-like reaction mechanisms. Moreover, other groups have already found evidence against the involvement of hydroxyl radicals in this catalytic process.[304,305]

The greatest strength of this work lies in the fact that dehydrogenation of non-activated C–H bonds has been accomplished under mild reaction conditions and without any driving force such as aromatization. Moreover, calculations reported in this thesis account for the mixtures of hydroxylated and dehydrogenated products experimentally obtained.

*"Nature's music is never over; her silences are pauses but not conclusions."*

Mary Webb

# 9

# *General Conclusions*

This thesis shows how computational methods, namely DFT calculations, can provide a molecular insight into complex catalytic oxidation reactions and give valuable information on the key factors governing reactivity and selectivity. Since a broad discussion has been carried out at the end of each chapter, only the general remarks drawn from the investigated reactions are presented herein.

Water Oxidation Reaction

The water oxidation reaction has been studied considering the Bernhard molecular catalyst $[Ir(O)(X)(phpy)_2]^n$ with X = $OH_2$ (n = +1), $OH^-$ (n = 0) or $O^{2-}$ (n = -1) and a model hybrid-type system, which consists in anchoring an iridium complex on the $IrO_2(110)$ surface. These studies have allowed to broaden the outlook of this process and to provide a clearer picture for further improvements.

- Incorporating internal Brønsted bases, which accept a proton from the attacking water molecule, can improve catalytic efficiency.
- The pH media, as well as the potential applied, determines the nature of the active species.
- An intramolecular nucleophilic attack mechanism operates in the $[Ir(O)(X)(phpy)_2]^n$-catalyzed water oxidation.
- Hybrid-type catalysts are viable and may benefit from the activity of the homogeneous and the stability of the heterogeneous ones.
- The performance of these combined catalytic systems can be improved by fine-tuning the ligands of the homogeneous part and the electronic properties of the heterogeneous part.

Oxygenation of C=C bonds

This work has provided a feasible mechanistic landscape for the functionalization of alkenes using molecular oxygen. It gives useful insight for the future design of new high-performance complexes for the selective

oxidation of C=C bonds.

- These reactions involve a complex mechanistic scheme, since potential energy surfaces of different spin states participate in the overall energy pathway.
- The reaction outcome is dictated by the relative stability of the closed-shell peroxo and the open-shell superoxo species resulting from initial coordination of dioxygen to the metal complex.
- Superoxo species leads to a dinuclear 2-metallaoxetane compound, whereas peroxo species gives rise to a monomeric oxygenated product.
- Compared to Rh, Ir-based catalysts stabilize to a larger extent the peroxo species, due to a better overlap between the metal and ligands orbitals.
- More electron-donating ligands favor the peroxo adduct due to a higher stabilization of the M(III) oxidation state over M(II).

Oxidation of C-H bonds

The selective hydroxylation of $sp^2$ and $sp^3$ C-H bonds has been achieved with $H_2O_2$ as oxidizing agent and a Cu-base catalyst.

- Calculations support a Cu-oxo complex as catalytically active species, which has both electrophilic and radical oxyl character.
- The hydroxylation of benzene evolves mainly through an $S_EAr$-like mechanism, although in the presence of strong electron withdrawing substituents the rebound pathway opens lower energy pathways.
- For the cyclohexane oxidation, two competing reactions have been characterized: hydroxylation and dehydrogenation. The hydroxylation path is preferred over the dehydrogenation one, which accounts for the high cyclohexanol/cyclohexene ratio (93:7) observed experimentally.

# *Bibliography*

1. Jordan, B. *Reaction Mechanisms of Inorganic and Organometallic Systems*, 3rd ed.; Oxford University Press: New York, 2007.
2. Grossman, R. B. *The Art of Writing Reasonable Organic Reaction Mechanisms*; Springer: New York, 1999.
3. Morokuma, K.; Musaev, D. G. *Computational Modeling for Homogeneous and Enzymatic Catalysis: A Knowledge-Base for Designing Efficient Catalysis*; John Wiley & Sons, 2008.
4. Maseras, F.; Lledós, A. *Computational Modeling of Homogeneous Catalysis*; Springer Science & Business Media, 2002.
5. Cundari, T. R. *Computational Organometallic Chemistry*; CRC Press, 2001.
6. Kozuch, S.; Shaik, S. How to Conceptualize Catalytic Cycles? The Energetic Span Model. *Acc. Chem. Res.* **2011**, *44* (2), 101–110.
7. Evans, M. G.; Polanyi, M. Some Applications of the Transition State Method to the Calculation of Reaction Velocities, Especially in Solution. *Trans. Faraday Soc.* **1935**, *31* (0), 875–894.
8. Eyring, H. The Activated Complex in Chemical Reactions. *J. Chem. Phys.* **1935**, *3* (2), 107–115.
9. García-Mota, M.; Vojvodic, A.; Metiu, H.; Man, I. C.; Su, H.-Y.; Rossmeisl, J.; Nørskov, J. K. Tailoring the Activity for Oxygen Evolution Electrocatalysis on Rutile $TiO_2$(110) by Transition-Metal Substitution. *ChemCatChem* **2011**, *3* (10), 1607–1611.
10. Astruc, D. *Organometallic Chemistry and Catalysis*; Springer: Berlin, 2007.
11. Elschenbroich, C.; Salzer, A. *Organometallics: A Concise Introduction*, 2nd ed.; Wiley-VCH: Weinheim, 1992.
12. Beller, M.; Blaser, H.-U. (Eds.). *Organometallics as Catalysts in the Fine Chemical Industry*; Springer: Berlin, 2012; Vol. 42.
13. Bozec, H.; Guerchais, V. (Eds). *Molecular Organometallic Materials for Optics*; Springer: Berlin, 2010; Vol. 28.
14. Fourmigué, M.; Ouahab, L. (Eds). *Conducting and Magnetic Organometallic Molecular Materials*; Springer: Berlin, 2009; Vol. 27.
15. Simonneaux, G. (Ed). *Bioorganometallic Chemistry*; Springer: Berlin, 2006; Vol. 17.
16. Fernández-García, M.; Martínez-Arias, A.; Hanson, J. C.; Rodriguez, J. A. Nanostructured Oxides in Chemistry: Characterization and Properties. *Chem. Rev.* **2004**, *104* (9), 4063–4104.
17. Hu, J.; Odom, T. W.; Lieber, C. M. Chemistry and Physics in One Dimension: Synthesis and Properties of Nanowires and Nanotubes. *Acc. Chem. Res.* **1999**, *32* (5), 435–445.

18. Van Leeuwen, P. W. N. M.; Claver, C. *Rhodium Catalyzed Hydroformylation*; Springer Science & Business Media, 2002.
19. Beller, M.; Cornils, B.; Frohning, C. D.; Kohlpaintner, C. W. Progress in Hydroformylation and Carbonylation. *J. Mol. Catal. Chem.* **1995**, *104* (1), 17–85.
20. Ziegler, K.; Holzkamp, E.; Breil, H.; Martin, H. Das Mülheimer Normaldruck-Polyäthylen-Verfahren. *Angew Chem* **1955**, *67*, 541-547.
21. Natta, G.; Pasquon, I. The Kinetics of the Stereospecific Polymerization of α-Olefins. *Adv. Catal.* **1959**, *11*, 1–66.
22. Jira, R. Acetaldehyde from Ethylene-A Retrospective on the Discovery of the Wacker Process. *Angew. Chem. Int. Ed.* **2009**, *48* (48), 9034–9037.
23. Stirling, A.; Nair, N. N.; Lledós, A.; Ujaque, G. Challenges in Modelling Homogeneous Catalysis: New Answers from Ab Initio Molecular Dynamics to the Controversy over the Wacker Process. *Chem. Soc. Rev.* **2014**, *43* (14), 4940–4952.
24. Dry, M. E. The Fischer–Tropsch Process: 1950–2000. *Catal. Today* **2002**, *71* (3-4), 227–241.
25. Mills, G.A.; Steffgen, F.W. Catalytic Methanation. *Catal Rev* **1973**, *8*, 159-210.
26. Goeppert, A.; Czaun, M.; Jones, J.-P.; Prakash, G. K. S.; Olah, G. A. Recycling of Carbon Dioxide to Methanol and Derived Products – Closing the Loop. *Chem. Soc. Rev.* **2014**, *43* (23), 7995–8048.
27. Satterfield, C. N. *Heterogeneous Catalysis in Practice*; McGraw-Hill: New York, 1980.
28. Thomas, C. L. Chemistry of Cracking Catalysts. *Ind. Eng. Chem.* **1949**, *41* (11), 2564–2573.
29. Corma, A.; Grande, M. S.; Gonzalez-Alfaro, V.; Orchilles, A. V. Cracking Activity and Hydrothermal Stability of MCM-41 and Its Comparison with Amorphous Silica-Alumina and a USY Zeolite. *J. Catal.* **1996**, *159* (2), 375–382.
30. Farnetti, E.; Di Monte, R.; Kašpar, J. Homogeneous and Heterogeneous Catalysis. In *Inorganic and bio-inorganic chemistry*; Eolss Publishers: Oxford, UK, 2007; Vol. II.
31. Savini, A.; Bucci, A.; Nocchetti, M.; Vivani, R.; Idriss, H.; Macchioni, A. Activity and Recyclability of an Iridium–EDTA Water Oxidation Catalyst Immobilized onto Rutile $TiO_2$. *ACS Catal.* **2015**, *5* (1), 264–271.
32. Sheehan, S. W.; Thomsen, J. M.; Hintermair, U.; Crabtree, R. H.; Brudvig, G. W.; Schmuttenmaer, C. A. A Molecular Catalyst for Water Oxidation That Binds to Metal Oxide Surfaces. *Nat. Commun.* **2015**, *6*. DOI:10.1038/ncomms7469.

33. Lewis, N. S.; Nocera, D. G. Powering the Planet: Chemical Challenges in Solar Energy Utilization. *Proc. Natl. Acad. Sci.* **2006**, *103* (43), 15729–15735.
34. Gust, D.; Moore, T. A.; Moore, A. L. Solar Fuels via Artificial Photosynthesis. *Acc. Chem. Res.* **2009**, *42* (12), 1890–1898.
35. Jacobson, M. Z. Review of Solutions to Global Warming, Air Pollution, and Energy Security. *Energy Environ. Sci.* **2009**, *2* (2), 148–173.
36. Yang, Z.; Zhang, J.; Kintner-Meyer, M. C. W.; Lu, X.; Choi, D.; Lemmon, J. P.; Liu, J. Electrochemical Energy Storage for Green Grid. *Chem. Rev.* **2011**, *111* (5), 3577–3613.
37. Wadsworth, E.; Duke, F. R.; Goetz, C. A. Present Status of Cerium(IV)-Cerium(III) Potentials. *Anal. Chem.* **1957**, *29* (12), 1824–1825.
38. Parent, A. R.; Crabtree, R. H.; Brudvig, G. W. Comparison of Primary Oxidants for Water-Oxidation Catalysis. *Chem. Soc. Rev.* **2013**, *42* (6), 2247–2252.
39. Weavers, L. K.; Hua, I.; Hoffmann, M. R. Degradation of Triethanolamine and Chemical Oxygen Demand Reduction in Wastewater by Photoactivated Periodate. *Water Environ. Res.* **1997**, *69* (6), 1112–1119.
40. Hetterscheid, D. G. H.; Reek, J. N. H. Periodate as an Oxidant for Catalytic Water Oxidation: Oxidation via Electron Transfer or O-Atom Transfer? *Eur. J. Inorg. Chem.* **2014**, *2014* (4), 742–749.
41. Trasatti, S. Electrocatalysis of Hydrogen Evolution: Progress in Cathode Activation. In *Advances in Electrochemical Science and Engineering*; Gerischer, H., Tobias, C. W., Eds.; Wiley-VCH Verlag GmbH, 1991; pp 1–85.
42. Li, Y.; Wang, H.; Xie, L.; Liang, Y.; Hong, G.; Dai, H. $MoS_2$ Nanoparticles Grown on Graphene: An Advanced Catalyst for the Hydrogen Evolution Reaction. *J. Am. Chem. Soc.* **2011**, *133* (19), 7296–7299.
43. Zouni, A.; Witt, H.-T.; Kern, J.; Fromme, P.; Krauss, N.; Saenger, W.; Orth, P. Crystal Structure of Photosystem II from Synechococcus Elongatus at 3.8 Å Resolution. *Nature* **2001**, *409* (6821), 739–743.
44. Blakemore, J. D.; Schley, N. D.; Balcells, D.; Hull, J. F.; Olack, G. W.; Incarvito, C. D.; Eisenstein, O.; Brudvig, G. W.; Crabtree, R. H. Half-Sandwich Iridium Complexes for Homogeneous Water-Oxidation Catalysis. *J. Am. Chem. Soc.* **2010**, *132* (45), 16017–16029.
45. Duan, L.; Bozoglian, F.; Mandal, S.; Stewart, B.; Privalov, T.; Llobet, A.; Sun, L. A Molecular Ruthenium Catalyst with Water-

Oxidation Activity Comparable to that of Photosystem II. *Nat. Chem.* **2012**, *4* (5), 418–423.
46. Shimazaki, Y.; Nagano, T.; Takesue, H.; Ye, B.-H.; Tani, F.; Naruta, Y. Characterization of a Dinuclear MnVO Complex and Its Efficient Evolution of $O_2$ in the Presence of Water. *Angew. Chem. Int. Ed.* **2004**, *43* (1), 98–100.
47. Limburg, J.; Vrettos, J. S.; Liable-Sands, L. M.; Rheingold, A. L.; Crabtree, R. H.; Brudvig, G. W. A Functional Model for O-O Bond Formation by the $O_2$-Evolving Complex in Photosystem II. *Science* **1999**, *283* (5407), 1524–1527.
48. Rotzinger, F. P.; Munavalli, S.; Comte, P.; Hurst, J. K.; Graetzel, M.; Pern, F. J.; Frank, A. J. A Molecular Water-Oxidation Catalyst Derived from Ruthenium Diaqua bis(2,2'-Bipyridyl-5,5'-Dicarboxylic Acid). *J. Am. Chem. Soc.* **1987**, *109* (22), 6619–6626.
49. Deng, Z.; Tseng, H.-W.; Zong, R.; Wang, D.; Thummel, R. Preparation and Study of a Family of Dinuclear Ru(II) Complexes that Catalyze the Decomposition of Water. *Inorg. Chem.* **2008**, *47* (6), 1835–1848.
50. Sens, C.; Romero, I.; Rodríguez, M.; Llobet, A.; Parella, T.; Benet-Buchholz, J. A New Ru Complex Capable of Catalytically Oxidizing Water to Molecular Dioxygen. *J. Am. Chem. Soc.* **2004**, *126* (25), 7798–7799.
51. Yin, Q.; Tan, J. M.; Besson, C.; Geletii, Y. V.; Musaev, D. G.; Kuznetsov, A. E.; Luo, Z.; Hardcastle, K. I.; Hill, C. L. A Fast Soluble Carbon-Free Molecular Water Oxidation Catalyst Based on Abundant Metals. *Science* **2010**, *328* (5976), 342–345.
52. Lv, H.; Geletii, Y. V.; Zhao, C.; Vickers, J. W.; Zhu, G.; Luo, Z.; Song, J.; Lian, T.; Musaev, D. G.; Hill, C. L. Polyoxometalate Water Oxidation Catalysts and the Production of Green Fuel. *Chem. Soc. Rev.* **2012**, *41* (22), 7572–7589.
53. Rossmeisl, J.; Qu, Z.-W.; Kroes, G.-J.; Nørskov, J.K. Electrolysis of Water on Oxide Surfaces. *J. Electroanal. Chem.* **2007**, *607* (1-2), 83–89.
54. Man, I. C.; Su, H.-Y.; Calle-Vallejo, F.; Hansen, H. A.; Martínez, J. I.; Inoglu, N. G.; Kitchin, J.; Jaramillo, T. F.; Nørskov, J. K.; Rossmeisl, J. Universality in Oxygen Evolution Electrocatalysis on Oxide Surfaces. *ChemCatChem* **2011**, *3* (7), 1159–1165.
55. Luna, M. A.; Moyano, F.; Sereno, L.; D'Eramo, F. Spectroscopic and Electrochemical Studies of High-Valent Water Soluble Manganese Porphyrine. Electrocatalytic Water Oxidation. *Electrochimica Acta* **2014**, *135*, 301–310.
56. Concepcion, J. J.; Jurss, J. W.; Templeton, J. L.; Meyer, T. J. One Site Is Enough. Catalytic Water Oxidation by

[Ru(tpy)(bpm)(OH$_2$)]$^{2+}$ and [Ru(tpy)(bpz)(OH$_2$)]$^{2+}$. *J. Am. Chem. Soc.* **2008**, *130* (49), 16462–16463.
57. Zong, R.; Thummel, R. P. A New Family of Ru Complexes for Water Oxidation. *J. Am. Chem. Soc.* **2005**, *127* (37), 12802–12803.
58. Kärkäs, M. D.; Åkermark, T.; Chen, H.; Sun, J.; Åkermark, B. A Tailor-Made Molecular Ruthenium Catalyst for the Oxidation of Water and Its Deactivation through Poisoning by Carbon Monoxide. *Angew. Chem.* **2013**, *125* (15), 4283–4287.
59. Fang, Y.-H.; Liu, Z.-P. Mechanism and Tafel Lines of Electro-Oxidation of Water to Oxygen on RuO$_2$(110). *J. Am. Chem. Soc.* **2010**, *132* (51), 18214–18222.
60. Concepcion, J. J.; Jurss, J. W.; Brennaman, M. K.; Hoertz, P. G.; Patrocinio, A. O. T.; Murakami Iha, N. Y.; Templeton, J. L.; Meyer, T. J. Making Oxygen with Ruthenium Complexes. *Acc. Chem. Res.* **2009**, *42* (12), 1954–1965.
61. McDaniel, N. D.; Coughlin, F. J.; Tinker, L. L.; Bernhard, S. Cyclometalated Iridium(III) Aquo Complexes: Efficient and Tunable Catalysts for the Homogeneous Oxidation of Water. *J. Am. Chem. Soc.* **2008**, *130* (1), 210–217.
62. Hull, J. F.; Balcells, D.; Blakemore, J. D.; Incarvito, C. D.; Eisenstein, O.; Brudvig, G. W.; Crabtree, R. H. Highly Active and Robust Cp* Iridium Complexes for Catalytic Water Oxidation. *J. Am. Chem. Soc.* **2009**, *131* (25), 8730–8731.
63. Savini, A.; Bellachioma, G.; Ciancaleoni, G.; Zuccaccia, C.; Zuccaccia, D.; Macchioni, A. Iridium(III) Molecular Catalysts for Water Oxidation: The Simpler the Faster. *Chem. Commun.* **2010**, *46* (48), 9218–9219.
64. Minguzzi, A.; Lugaresi, O.; Achilli, E.; Locatelli, C.; Vertova, A.; Ghigna, P.; Rondinini, S. Observing the Oxidation State Turnover in Heterogeneous Iridium-Based Water Oxidation Catalysts. *Chem. Sci.* **2014**, *5* (9), 3591–3597.
65. Du, P.; Eisenberg, R. Catalysts Made of Earth-Abundant Elements (Co, Ni, Fe) for Water Splitting: Recent Progress and Future Challenges. *Energy Environ. Sci.* **2012**, *5* (3), 6012–6021.
66. Chen, G.; Chen, L.; Ng, S.-M.; Lau, T.-C. Efficient Chemical and Visible-Light-Driven Water Oxidation Using Nickel Complexes and Salts as Precatalysts. *ChemSusChem* **2014**, *7* (1), 127–134.
67. Codolà, Z.; Garcia-Bosch, I.; Acuña-Parés, F.; Prat, I.; Luis, J. M.; Costas, M.; Lloret-Fillol, J. Electronic Effects on Single-Site Iron Catalysts for Water Oxidation. *Chem. – Eur. J.* **2013**, *19* (25), 8042–8047.
68. Acuña-Parés, F.; Codolà, Z.; Costas, M.; Luis, J. M.; Lloret-Fillol, J. Unraveling the Mechanism of Water Oxidation Catalyzed by

Nonheme Iron Complexes. *Chem. – Eur. J.* **2014**, *20* (19), 5696–5707.

69. Ellis, W. C.; McDaniel, N. D.; Bernhard, S.; Collins, T. J. Fast Water Oxidation Using Iron. *J. Am. Chem. Soc.* **2010**, *132* (32), 10990–10991.
70. Wang, D.; Groves, J. T. Efficient Water Oxidation Catalyzed by Homogeneous Cationic Cobalt Porphyrins with Critical Roles for the Buffer Base. *Proc. Natl. Acad. Sci.* **2013**, *110* (39), 15579–15584.
71. Barnett, S. M.; Goldberg, K. I.; Mayer, J. M. A Soluble Copper–bipyridine Water-Oxidation Electrocatalyst. *Nat. Chem.* **2012**, *4* (6), 498–502.
72. Sala, X.; Maji, S.; Bofill, R.; García-Antón, J.; Escriche, L.; Llobet, A. Molecular Water Oxidation Mechanisms Followed by Transition Metals: State of the Art. *Acc. Chem. Res.* **2014**, *47* (2), 504–516.
73. Yang, X.; Baik, M.-H. The Mechanism of Water Oxidation Catalysis Promoted by $[tpyRu(IV)=O]_2L_3^+$: A Computational Study. *J. Am. Chem. Soc.* **2008**, *130* (48), 16231–16240
74. Wang, L.-P.; Wu, Q.; Van Voorhis, T. Acid−Base Mechanism for Ruthenium Water Oxidation Catalysts. *Inorg. Chem.* **2010**, *49* (10), 4543–4553.
75. Chen, Z.; Concepcion, J. J.; Hu, X.; Yang, W.; Hoertz, P. G.; Meyer, T. J. Concerted O Atom–proton Transfer in the O—O Bond Forming Step in Water Oxidation. *Proc. Natl. Acad. Sci.* **2010**, *107* (16), 7225–7229.
76. Yang, X.; Baik, M.-H. Cis,cis-[(bpy)2RuVO]2O4+ Catalyzes Water Oxidation Formally via in Situ Generation of Radicaloid RuIV−O•. *J. Am. Chem. Soc.* **2006**, *128* (23), 7476–7485.
77. Romain, S.; Bozoglian, F.; Sala, X.; Llobet, A. Oxygen−Oxygen Bond Formation by the Ru-Hbpp Water Oxidation Catalyst Occurs Solely via an Intramolecular Reaction Pathway. *J. Am. Chem. Soc.* **2009**, *131* (8), 2768–2769.
78. Bozoglian, F.; Romain, S.; Ertem, M. Z.; Todorova, T. K.; Sens, C.; Mola, J.; Rodríguez, M.; Romero, I.; Benet-Buchholz, J.; Fontrodona, X.; et al. The Ru−Hbpp Water Oxidation Catalyst. *J. Am. Chem. Soc.* **2009**, *131* (42), 15176–15187.
79. Wang, L.-P.; Van Voorhis, T. Direct-Coupling $O_2$ Bond Forming a Pathway in Cobalt Oxide Water Oxidation Catalysts. *J. Phys. Chem. Lett.* **2011**, *2* (17), 2200–2204.
80. Romain, S.; Vigara, L.; Llobet, A. Oxygen−Oxygen Bond Formation Pathways Promoted by Ruthenium Complexes. *Acc. Chem. Res.* **2009**, *42* (12), 1944–1953.

81. Ertem, M. Z.; Gagliardi, L.; Cramer, C. J. Quantum Chemical Characterization of the Mechanism of an Iron-Based Water Oxidation Catalyst. *Chem. Sci.* **2012**, *3* (4), 1293–1299.
82. Sameera, W. M. C.; McKenzie, C. J.; McGrady, J. E. On the Mechanism of Water Oxidation by a Bimetallic Manganese Catalyst: A Density Functional Study. *Dalton Trans.* **2011**, *40* (15), 3859–3870.
83. Lundberg, M.; Blomberg, M. R. A.; Siegbahn, P. E. M. Oxyl Radical Required for O−O Bond Formation in Synthetic Mn-Catalyst. *Inorg. Chem.* **2004**, *43* (1), 264–274.
84. Hill, C. L.; Weinstock, I. A. Homogeneous Catalysis: On the Trail of Dioxygen Activation. *Nature* **1997**, *388* (6640), 332–333.
85. Smidt, J.; Hafner, W.; Jira, R.; Sedlmeier, J.; Sieber, R.; Rüttinger, R.; Kojer, H. *Angew Chem* **1959**, *71*, 176–182.
86. Van Santen, R. A.; Kuipers, H. P. C. E. The Mechanism of Ethylene Epoxidation. In *Advances in Catalysis*; D.D. Eley, H. P. and P. B. W., Ed.; Academic Press, 1987; Vol. 35, pp 265–321.
87. Tejel, C.; Ciriano, M. A.; Sola, E.; del Río, M. P.; Ríos-Moreno, G.; Lahoz, F. J.; Oro, L. A. Dimetallic Dioxygen Activation Leading to a Doubly Oxygen-Bridged Dirhodium Complex. *Angew. Chem. Int. Ed.* **2005**, *44* (21), 3267–3271.
88. Kelley, M. R.; Rohde, J.-U. Guanidinato Complexes of Iridium: Ligand-Donor Strength, $O_2$ Reactivity, and (Alkene)peroxo-iridium(III) Intermediates. *Inorg. Chem.* **2013**, *52* (5), 2564–2580.
89. Kelley, M. R.; Rohde, J.-U. Evidence for a Reactive (alkene)-peroxoiridium(III) Intermediate in the Oxidation of an Alkene Complex with $O_2$. *Chem. Commun.* **2012**, *48* (23), 2876–2878.
90. De Bruin, B.; Budzelaar, P. H. M.; Gal, A. W. Functional Models for Rhodium-Mediated Olefin-Oxygenation Catalysis. *Angew. Chem. Int. Ed.* **2004**, *43* (32), 4142–4157.
91. De Bruin, B.; Peters, T. P. J.; Wilting, J. B. M.; Thewissen, S.; Smits, J. M. M.; Gal, A. W. Dioxygenation of Sterically Hindered (Ethene)RhI and -IrI Complexes to (Peroxo)RhIII and (Ethene) (peroxo)IrIII Complexes. *Eur. J. Inorg. Chem.* **2002**, *2002* (10), 2671–2680.
92. De Bruin, B.; Boerakker, M. J.; Brands, J. A.; Donners, J. J. J. M.; Donners, M. P. J.; de Gelder, R.; Smits, J. M. M.; Gal, A. W.; Spek, A. L. Selective Oxidation of [RhI(cod)]+ by $H_2O_2$ and $O_2$. *Chem. – Eur. J.* **1999**, *5* (10), 2921–2936.
93. Van der Ent, A.; Onderdelinden, A.L. Some Addition Compounds of chlorobis(triphenylphospine)iridium(I). *Inorganica Chim. Acta* **1973**, *7*, 203–208.
94. Igersheim, F.; Mimoun. H. Activation and transfer of molecular oxygen. Oxidation of terminal olefins to methyl ketones by

rhodium dioxygen complexes. *J Chem Soc Chem Commun* **1978**, 559-560.

95. Krom, M.; Coumans, R. G. E.; Smits, J. M. M.; Gal, A. W. 3-Rhoda-1,2-Dioxolanes through Dioxygenation of a Rhodium–Ethene Complex by Air. *Angew. Chem. Int. Ed.* **2001**, *40* (11), 2106–2108.
96. Krom, M.; Peters, T. P. J.; Coumans, R. G. E.; Sciarone, T. J. J.; Hoogboom, J.; Beek, S. I. ter; Schlebos, P. P. J.; Smits, J. M. M.; de Gelder, R.; Gal, A. W. 3-Metalla-1,2-Dioxolanes and Their Reactivity. *Eur. J. Inorg. Chem.* **2003**, *2003* (6), 1072–1087.
97. Day, V. W.; Klemperer, W. G.; Lockledge, S. P.; Main, D. J. Oxygen Atom Transfer from $O_2$ to a Coordinated Olefin: A New Route to Oxametallacyclobutanes. *J. Am. Chem. Soc.* **1990**, *112* (5), 2031–2033.
98. Li, J.; Schreckenbach, G.; Ziegler, T. Relativistic Effects on Metal-Ligand Bond Strengths in .pi.-Complexes: Quasi-Relativistic Density Functional Study of $M(PH_3)_2X_2$ (M = Ni, Pd, Pt; $X_2 = O_2$, $C_2H_2$, $C_2H_4$) and $M(CO)_4(C_2H_4)$ (M = Fe, Ru, Os). *Inorg. Chem.* **1995**, *34* (12), 3245–3252.
99. De Bruin, B.; Verhagen, J. A. W.; Schouten, C. H. J.; Gal, A. W.; Feichtinger, D.; Plattner, D. A. Enhanced Reactivity of 2-Rhodaoxetanes through a Labile Acetonitrile Ligand. *Chem. – Eur. J.* **2001**, *7* (2), 416–422.
100. Flood, T. C.; Iimura, M.; Perotti, J. M.; Rheingold, A. L.; Concolino, T. E. Oxidation of [(cyclic triamine)(1,5-Cyclooctadiene)iridium]$^+$ Cations by Hydrogen Peroxide Forms Metallaoxetanes. *Chem. Commun.* **2000**, No. 17, 1681–1682.
101. Newhouse, T.; Baran, P. S. If C-H Bonds Could Talk: Selective C-H Bond Oxidation. *Angew. Chem. Int. Ed.* **2011**, *50* (15), 3362–3374.
102. Roduner, E.; Kaim, W.; Sarkar, B.; Urlacher, V. B.; Pleiss, J.; Gläser, R.; Einicke, W.-D.; Sprenger, G. A.; Beifuß, U.; Klemm, E.; et al. Selective Catalytic Oxidation of C-H Bonds with Molecular Oxygen. *ChemCatChem* **2013**, *5* (1), 82–112.
103. Mayer, J. M. Hydrogen Atom Abstraction by Metal−Oxo Complexes: Understanding the Analogy with Organic Radical Reactions. *Acc. Chem. Res.* **1998**, *31* (8), 441–450.
104. Mayer, J. M. *Biomimetic Oxidations Catalyzed by Transition Metal Complexes*; Meunier, B., Ed.; Imperial College Press, 1999.
105. Balcells, D.; Clot, E.; Eisenstein, O. C-H Bond Activation in Transition Metal Species from a Computational Perspective. *Chem. Rev.* **2010**, *110* (2), 749–823.
106. Shilov, A. E.; Shul'pin, G. B. Activation of C−H Bonds by Metal Complexes. *Chem. Rev.* **1997**, *97* (8), 2879–2932.

107. Vanelderen, P.; Hadt, R. G.; Smeets, P. J.; Solomon, E. I.; Schoonheydt, R. A.; Sels, B. F. Cu-ZSM-5: A Biomimetic Inorganic Model for Methane Oxidation. *J. Catal.* **2011**, *284* (2), 157-164.
108. Hammond, C.; Jenkins, R. L.; Dimitratos, N.; Lopez-Sanchez, J. A.; ab Rahim, M. H.; Forde, M. M.; Thetford, A.; Murphy, D. M.; Hagen, H.; Stangland, E. E.; et al. Catalytic and Mechanistic Insights of the Low-Temperature Selective Oxidation of Methane over Cu-Promoted Fe-ZSM-5. *Chem. – Eur. J.* **2012**, *18* (49), 15735–15745.
109. Alayon, E. M. C.; Nachtegaal, M.; Bodi, A.; van Bokhoven, J. A. Reaction Conditions of Methane-to-Methanol Conversion Affect the Structure of Active Copper Sites. *ACS Catal.* **2013**, *4* (1), 16–22.
110. Yoshizawa, K.; Yumura, T. A Non-Radical Mechanism for Methane Hydroxylation at the Diiron Active Site of Soluble Methane Monooxygenase. *Chem. – Eur. J.* **2003**, *9* (10), 2347–2358.
111. Mirica, L. M.; Vance, M.; Rudd, D. J.; Hedman, B.; Hodgson, K. O.; Solomon, E. I.; Stack, T. D. P. Tyrosinase Reactivity in a Model Complex: An Alternative Hydroxylation Mechanism. *Science* **2005**, *308* (5730), 1890–1892.
112. Ozaki, S.; Roach, M. P.; Matsui, T.; Watanabe, Y. Investigations of the Roles of the Distal Heme Environment and the Proximal Heme Iron Ligand in Peroxide Activation by Heme Enzymes via Molecular Engineering of Myoglobin. *Acc. Chem. Res.* **2001**, *34* (10), 818–825.
113. Wu, A. J.; Penner-Hahn, J. E.; Pecoraro, V. L. Structural, Spectroscopic, and Reactivity Models for the Manganese Catalases. *Chem. Rev.* **2004**, *104* (2), 903–938.
114. Murahashi, S.-I.; Zhang, D. Ruthenium Catalyzed Biomimetic Oxidation in Organic Synthesis Inspired by Cytochrome P-450. *Chem. Soc. Rev.* **2008**, *37* (8), 1490–1501.
115. Wender, I. Reactions of Synthesis Gas. *Fuel Process. Technol.* **1996**, *48* (3), 189–297.
116. Hall, C.; Perutz, R. N. Transition Metal Alkane Complexes. *Chem. Rev.* **1996**, *96* (8), 3125–3146.
117. Bernskoetter, W. H.; Schauer, C. K.; Goldberg, K. I.; Brookhart, M. Characterization of a Rhodium(I) σ-Methane Complex in Solution. *Science* **2009**, *326* (5952), 553–556.
118. Dedieu, A. Theoretical Studies in Palladium and Platinum Molecular Chemistry. *Chem. Rev.* **2000**, *100* (2), 543–600.
119. Zhenyang Lin. Current Understanding of the σ-Bond Metathesis Reactions of LnMR + R′–H → LnMR′ + R–H. *Coord. Chem. Rev.* **2007**, *251* (17-20), 2280–2291.
120. Slaughter, L. M.; Wolczanski, P. T.; Klinckman, T. R.; Cundari, T. R. Inter- and Intramolecular Experimental and Calculated

Equilibrium Isotope Effects for $(silox)_2(tBu_3SiND)TiR + RH$ (silox = $tBu_3SiO$): Inferred Kinetic Isotope Effects for RH/D Addition to Transient $(silox)_2TiNSitBu_3$. *J. Am. Chem. Soc.* **2000**, *122* (33), 7953–7975.

121. Cundari, T. R.; Klinckman, T. R.; Wolczanski, P. T. Carbon−Hydrogen Bond Activation by Titanium Imido Complexes. Computational Evidence for the Role of Alkane Adducts in Selective C−H Activation. *J. Am. Chem. Soc.* **2002**, *124* (7), 1481–1487.
122. Gunay, A.; Theopold, K. H. C−H Bond Activations by Metal Oxo Compounds. *Chem. Rev.* **2010**, *110* (2), 1060–1081.
123. De Visser, S. P.; Oh, K.; Han, A.-R.; Nam, W. Combined Experimental and Theoretical Study on Aromatic Hydroxylation by Mononuclear Nonheme Iron(IV)−Oxo Complexes. *Inorg. Chem.* **2007**, *46* (11), 4632–4641.
124. John T. Groves; Gary A. McClusky. Aliphatic Hydroxylation via Oxygen Rebound. Oxygen Transfer Catalyzed by Iron. *J. Am. Chem. Soc.* **1976**, *98* (3), 859–861.
125. Hull, J. F.; Balcells, D.; Sauer, E. L. O.; Raynaud, C.; Brudvig, G. W.; Crabtree, R. H.; Eisenstein, O. Manganese Catalysts for C−H Activation: An Experimental/Theoretical Study Identifies the Stereoelectronic Factor that Controls the Switch beta Hydroxylation and Desaturation Pathways. *J. Am. Chem. Soc.* **2010**, *132* (22), 7605–7616.
126. Lam, W. W. Y.; Yiu, S.-M.; Lee, J. M. N.; Yau, S. K. Y.; Kwong, H.-K.; Lau, T.-C.; Liu, D.; Lin, Z. $BF_3$-Activated Oxidation of Alkanes by $MnO_4^-$. *J. Am. Chem. Soc.* **2006**, *128* (9), 2851–2858.
127. Seok, W. K.; Dobson, J. C.; Meyer, T. J. Mechanisms of Oxidation of Phenol and Cyclohexene by an Oxo Complex of ruthenium(IV). *Inorg. Chem.* **1988**, *27* (1), 3–5.
128. Michel, C.; Belanzoni, P.; Gamez, P.; Reedijk, J.; Baerends, E. J. Activation of the C−H Bond by Electrophilic Attack: Theoretical Study of the Reaction Mechanism of the Aerobic Oxidation of Alcohols to Aldehydes by the $Cu(bipy)^{2+}$/2,2,6,6-Tetramethyl-piperidinyl-1-Oxy Cocatalyst System. *Inorg. Chem.* **2009**, *48* (24), 11909–11920
129. Ensing, B.; Buda, F.; Blöchl, P. E.; Baerends, E. J. A Car–Parrinello Study of the Formation of Oxidizing Intermediates from Fenton's Reagent in Aqueous Solution. *Phys. Chem. Chem. Phys.* **2002**, *4* (15), 3619–3627.
130. Cussó, O.; Garcia-Bosch, I.; Ribas, X.; Lloret-Fillol, J.; Costas, M. Asymmetric Epoxidation with $H_2O_2$ by Manipulating the Electronic Properties of Non-Heme Iron Catalysts. *J. Am. Chem. Soc.* **2013**, *135* (39), 14871–14878.

131. Starokon, E. V.; Parfenov, M. V.; Pirutko, L. V.; Abornev, S. I.; Panov, G. I. Room-Temperature Oxidation of Methane by α-Oxygen and Extraction of Products from the FeZSM-5 Surface. *J. Phys. Chem. C* **2011**, *115* (5), 2155–2161.
132. Biermann, U.; Bornscheuer, U.; Meier, M. A. R.; Metzger, J. O.; Schäfer, H. J. Oils and Fats as Renewable Raw Materials in Chemistry. *Angew. Chem. Int. Ed.* **2011**, *50* (17), 3854–3871.
133. Haibach, M. C.; Kundu, S.; Brookhart, M.; Goldman, A. S. Alkane Metathesis by Tandem Alkane-Dehydrogenation–Olefin-Metathesis Catalysis and Related Chemistry. *Acc. Chem. Res.* **2012**, *45* (6), 947–958.
134. Findlater, M.; Choi, J.; Goldman, A. S.; Brookhart, M. *Alkane C-H Activation by Single-Site Metal Catalysis*; Peŕez, P.J., Ed.; Springer: Dordrecht, 2012.
135. Caspary, K. J.; Gehrke, H.; Heinritz-Adrian, M.; Schwefer, M. *Handbook of Heterogeneous Catalysis*, Wiley.; Ertl, G., Knözinger, H., Schütz, F., Weitkamp, F., Eds.; Weinheim, 2008.
136. Macomber, R. S. *Organic Chemistry Vol. II: Chemical Behavior of Organic Compounds and Multi-Step Organic Synthesis*; University Science Books: Mill Valley, CA, 1996.
137. Sankararaman, S. *Pericyclic Reactions: A Textbook: Reactions, Applications and Theory*; Wiley-VCH: London, 2005.
138. García-Melchor, M.; Bellarosa, L.; López, N. Unique Reaction Path in Heterogeneous Catalysis: The Concerted Semi-Hydrogenation of Propyne to Propene on $CeO_2$. *ACS Catal.* **2014**, *4* (11), 4015–4020.
139. Baudry, D.; Ephritikhine, M.; Felkin, H. The selective conversion of n-pentane into pent-1-ene *via* trihydrido(*trans*-penta-1,3-diene)bis(triarylphosphine)rhenium. *J Chem Soc Chem Commun* **1982**, 606, 1235-1236.
140. Crabtree, R. H.; Mihelcic, J. M.; Quirk, J. M. Iridium Complexes in Alkane Dehydrogenation. *J. Am. Chem. Soc.* **1979**, *101* (26), 7738–7740.
141. Burk, M. J.; Crabtree, R. H. Selective Catalytic Dehydrogenation of Alkanes to Alkenes. *J. Am. Chem. Soc.* **1987**, *109* (26), 8025–8032.
142. Maguire, J. A.; Goldman, A. S. Efficient Low-Temperature Thermal Functionalization of Alkanes. Transfer Dehydrogenation Catalyzed by $Rh(PMe_3)_2Cl(CO)$ in Solution under a High-Pressure Hydrogen Atmosphere. *J. Am. Chem. Soc.* **1991**, *113* (17), 6706–6708.
143. Choi, J.; MacArthur, A. H. R.; Brookhart, M.; Goldman, A. S. Dehydrogenation and Related Reactions Catalyzed by Iridium Pincer Complexes. *Chem. Rev.* **2011**, *111* (3), 1761–1779.

144. Gupta, M.; Hagen, C.; Flesher, R. J.; Kaska, W. C.; Jensen, C. M. A Highly Active Alkane Dehydrogenation Catalyst: Stabilization of Dihydrido Rhodium and Iridium Complexes by a P–C–P Pincer Ligand. *Chem. Commun.* **1996**, No. 17, 2083–2084.
145. Xu, W.; Rosini, G. P.; Krogh-Jespersen, K.; Goldman, A. S.; Gupta, M.; Jensen, C. M.; Kaska, W. C. Thermochemical Alkane Dehydrogenation Catalyzed in Solution without the Use of a Hydrogen Acceptor. *Chem. Commun.* **1997**, No. 23, 2273–2274.
146. Szabo, A.; Ostlund, N. S. *Modern Quantum Chemistry: Introduction to Advanced Electronic Structure Theory*; Dover Publications: New York, 1982.
147. Koch, W.; Holthausen, M. C. *A Chemist's Guide to Density Functional Theory, Wiley- VCH*, 2nd ed.; Wiley- VCH: Weinheim, 2001.
148. Hohenberg, P.; Kohn, W. Inhomogeneous Electron Gas. *Phys Rev B* **1964**, *136*, 864–871.
149. Burke, K. Perspective on Density Functional Theory. *J. Chem. Phys.* **2012**, *136* (15), 150901-150909.
150. Becke, A. D. Perspective: Fifty Years of Density-Functional Theory in Chemical Physics. *J. Chem. Phys.* **2014**, *140* (18), 18A301-18A318.
151. W. Kohn; L. J. Sham. Self-Consistent Equations Including Exchange and Correlation Effects. *Phys Rev A* **1965**, *140*, 1133–1138.
152. Becke, A. D. Density Functional Calculations of Molecular Bond Energies. *J. Chem. Phys.* **1986**, *84* (8), 4524–4529.
153. Lee, C.; Yang, W.; Parr, R. G. Development of the Colle-Salvetti Correlation-Energy Formula into a Functional of the Electron Density. *Phys. Rev. B* **1988**, *37* (2), 785–789.
154. Perdew, J. P.; Burke, K.; Ernzerhof, M. Generalized Gradient Approximation Made Simple [Phys. Rev. Lett. 77, 3865 (1996)]. *Phys. Rev. Lett.* **1997**, *78* (7), 1396–1396.
155. Perdew, J. P.; Kurth, S.; Zupan, A.; Blaha, P. Accurate Density Functional with Correct Formal Properties: A Step Beyond the Generalized Gradient Approximation. *Phys. Rev. Lett.* **1999**, *82* (12), 2544–2547.
156. Tao, J.; Perdew, J. P.; Staroverov, V. N.; Scuseria, G. E. Climbing the Density Functional Ladder: Nonempirical Meta–Generalized Gradient Approximation Designed for Molecules and Solids. *Phys. Rev. Lett.* **2003**, *91* (14), 146401-146404.
157. Voorhis, T. V.; Scuseria, G. E. A Novel Form for the Exchange-Correlation Energy Functional. *J. Chem. Phys.* **1998**, *109* (2), 400–410.

158. Becke, A. D. A New Mixing of Hartree–Fock and Local Density-functional Theories. *J. Chem. Phys.* **1993**, *98* (2), 1372–1377.
159. Becke, A. D. Density-Functional Exchange-Energy Approximation with Correct Asymptotic Behavior. *Phys. Rev. A* **1988**, *38* (6), 3098–3100.
160. Poater, J.; Solà, M.; Rimola, A.; Rodríguez-Santiago, L.; Sodupe, M. Ground and Low-Lying States of $Cu^{2+}$–$H_2O$. A Difficult Case for Density Functional Methods. *J. Phys. Chem. A* **2004**, *108* (28), 6072–6078.
161. Rimola, A.; Rodríguez-Santiago, L.; Sodupe, M. Cation–π Interactions and Oxidative Effects on $Cu^+$ and $Cu^{2+}$ Binding to Phe, Tyr, Trp, and His Amino Acids in the Gas Phase. Insights from First-Principles Calculations. *J. Phys. Chem. B* **2006**, *110* (47), 24189–24199.
162. Rimola, A.; Constantino, E.; Rodríguez-Santiago, L.; Sodupe, M. Binding Properties of $Cu^{+/2+}$-(glycyl)nglycine Complexes (n = 1–3). *J. Phys. Chem. A* **2008**, *112* (15), 3444–3453.
163. Becke, A. D. Density-functional Thermochemistry. III. The Role of Exact Exchange. *J. Chem. Phys.* **1993**, *98* (7), 5648–5652.
164. Stephens, P. J.; Devlin, F. J.; Chabalowski, C. F.; Frisch, M. J. Ab Initio Calculation of Vibrational Absorption and Circular Dichroism Spectra Using Density Functional Force Fields. *J. Phys. Chem.* **1994**, *98* (45), 11623–11627.
165. Zhao, Y.; Truhlar, D. G. Density Functionals with Broad Applicability in Chemistry. *Acc. Chem. Res.* **2008**, *41* (2), 157–167.
166. Gonzales, J. M.; Cox, R. S.; Brown, S. T.; Allen, W. D.; Schaefer, H. F. Assessment of Density Functional Theory for Model SN2 Reactions: $CH_3X + F^-$ (X = F, Cl, CN, OH, SH, $NH_2$, $PH_2$). *J. Phys. Chem. A* **2001**, *105* (50), 11327–11346.
167. Zhao, Y.; Schultz, N. E.; Truhlar, D. G. Exchange-Correlation Functional with Broad Accuracy for Metallic and Nonmetallic Compounds, Kinetics, and Noncovalent Interactions. *J. Chem. Phys.* **2005**, *123* (16), 161103-161106.
168. Zhao, Y.; Schultz, N. E.; Truhlar, D. G. Design of Density Functionals by Combining the Method of Constraint Satisfaction with Parametrization for Thermochemistry, Thermochemical Kinetics, and Noncovalent Interactions. *J. Chem. Theory Comput.* **2006**, *2* (2), 364–382.
169. Zhao, Y.; Truhlar, D. G. A New Local Density Functional for Main-Group Thermochemistry, Transition Metal Bonding, Thermochemical Kinetics, and Noncovalent Interactions. *J. Chem. Phys.* **2006**, *125* (19), 194101-194118.
170. Zhao, Y.; Truhlar, D. G. The M06 Suite of Density Functionals for Main Group Thermochemistry, Thermochemical Kinetics,

Noncovalent Interactions, Excited States, and Transition Elements: Two New Functionals and Systematic Testing of Four M06-Class Functionals and 12 Other Functionals. *Theor. Chem. Acc.* **2007**, *120* (1-3), 215–241.
171. Grimme, S. Accurate Description of van Der Waals Complexes by Density Functional Theory Including Empirical Corrections. *J. Comput. Chem.* **2004**, *25* (12), 1463–1473.
172. Lynch, B. J.; Fast, P. L.; Harris, M.; Truhlar, D. G. Adiabatic Connection for Kinetics. *J. Phys. Chem. A* **2000**, *104* (21), 4811–4815.
173. Langreth, D. C.; Perdew, J. P. Theory of Nonuniform Electronic Systems. I. Analysis of the Gradient Approximation and a Generalization That Works. *Phys. Rev. B* **1980**, *21* (12), 5469–5493.
174. Lein, M.; Gross, E. K. U.; Perdew, J. P. Electron Correlation Energies from Scaled Exchange-Correlation Kernels: Importance of Spatial versus Temporal Nonlocality. *Phys. Rev. B* **2000**, *61* (20), 13431–13437.
175. Pitarke, J. M.; Eguiluz, A. G. Jellium Surface Energy beyond the Local-Density Approximation: Self-Consistent-Field Calculations. *Phys. Rev. B* **2001**, *63* (4), 045116-045127.
176. Fuchs, M.; Gonze, X. Accurate Density Functionals: Approaches Using the Adiabatic-Connection Fluctuation-Dissipation Theorem. *Phys. Rev. B* **2002**, *65* (23), 235109-235112.
177. Seidl, M.; Perdew, J. P.; Kurth, S. Simulation of All-Order Density-Functional Perturbation Theory, Using the Second Order and the Strong-Correlation Limit. *Phys. Rev. Lett.* **2000**, *84* (22), 5070–5073.
178. Schwabe, T.; Grimme, S. Theoretical Thermodynamics for Large Molecules: Walking the Thin Line between Accuracy and Computational Cost. *Acc. Chem. Res.* **2008**, *41* (4), 569–579.
179. Reiher, M.; Salomon, O.; Hess, B. A. Reparameterization of Hybrid Functionals Based on Energy Differences of States of Different Multiplicity. *Theor. Chem. Acc.* **2001**, *107* (1), 48–55.
180. Harvey, J. N. On the Accuracy of Density Functional Theory in Transition Metal Chemistry. *Annu. Rep. Sect. C Phys. Chem.* **2006**, *102* (0), 203–226.
181. Lewars, E. G. *Computational Chemistry: Introduction to the Theory and Applications of Molecular and Quantum Mechanics*; Springer Science & Business Media, 2010.
182. Cramer, C. J. *Essentials of Computational Chemistry: Theories and Models*; John Wiley & Sons, 2013.

183. Young, D. *Computational Chemistry: A Practical Guide for Applying Techniques to Real World Problems*; John Wiley & Sons, 2004.
184. Zhao, Y.; Truhlar, D. G. Hybrid Meta Density Functional Theory Methods for Thermochemistry, Thermochemical Kinetics, and Noncovalent Interactions: The MPW1B95 and MPWB1K Models and Comparative Assessments for Hydrogen Bonding and van Der Waals Interactions. *J. Phys. Chem. A* **2004**, *108* (33), 6908–6918.
185. Rios-Font, R.; Sodupe, M.; Rodríguez-Santiago, L.; Taylor, P. R. The Role of Exact Exchange in the Description of $Cu^{2+}$–$(H_2O)_n$ (n = 1–6) Complexes by Means of DFT Methods. *J. Phys. Chem. A* **2010**, *114* (40), 10857–10863.
186. Huff, G. S.; Doncheva, I. S.; Brinkley, D. W.; Angeles-Boza, A. M.; Mukherjee, A.; Cramer, C. J.; Roth, J. P. Experimental and Computational Investigations of Oxygen Reactivity in a Heme and Tyrosyl Radical-Containing Fatty Acid α-(Di)oxygenase. *Biochemistry (Mosc.)* **2011**, *50* (34), 7375–7389.
187. Lingwood, M.; Hammond, J. R.; Hrovat, D. A.; Mayer, J. M.; Borden, W. T. MPW1K Performs Much Better than B3LYP in DFT Calculations on Reactions That Proceed by Proton-Coupled Electron Transfer (PCET). *J. Chem. Theory Comput.* **2006**, *2* (3), 740–745.
188. Gong, X.-Q.; Liu, Z.-P.; Raval, R.; Hu, P. A Systematic Study of CO Oxidation on Metals and Metal Oxides: Density Functional Theory Calculations. *J. Am. Chem. Soc.* **2004**, *126* (1), 8–9.
189. Meyer, B.; Marx, D.; Dulub, O.; Diebold, U.; Kunat, M.; Langenberg, D.; Wöll, C. Partial Dissociation of Water Leads to Stable Superstructures on the Surface of Zinc Oxide. *Angew. Chem. Int. Ed.* **2004**, *43* (48), 6641–6645.
190. Ehrenreich, H.; Cohen, M. H. Self-Consistent Field Approach to the Many-Electron Problem. *Phys. Rev.* **1959**, *115* (4), 786–790.
191. Roothaan, C. C. J. Self-Consistent Field Theory for Open Shells of Electronic Systems. *Rev. Mod. Phys.* **1960**, *32* (2), 179–185.
192. Roothaan, CCJ. New Developments in Molecular Orbital Theory. *Rev Mod Phys* **1951**, *23*, 69.
193. Hay, P. J.; Wadt, W. R. Ab Initio Effective Core Potentials for Molecular Calculations. Potentials for the Transition Metal Atoms Sc to Hg. *J. Chem. Phys.* **1985**, *82* (1), 270–283.
194. Andrae, D.; Häußermann, U.; Dolg, M.; Stoll, H.; Preuß, H. Energy-Adjustedab Initio Pseudopotentials for the Second and Third Row Transition Elements. *Theor. Chim. Acta* **1990**, *77* (2), 123–141.

195. Bergner, A.; Dolg, M.; Küchle, W.; Stoll, H.; Preuß, H. Ab Initio Energy-Adjusted Pseudopotentials for Elements of Groups 13–17. *Mol. Phys.* **1993**, *80* (6), 1431–1441.
196. Kittel C. *Introduction to Solid State Physics*, 8th ed.; Wiley, John & Sons, 2004.
197. Blöchl, P. E. Projector Augmented-Wave Method. *Phys. Rev. B* **1994**, *50* (24), 17953–17979.
198. Kresse, G.; Joubert, D. From Ultrasoft Pseudopotentials to the Projector Augmented-Wave Method. *Phys. Rev. B* **1999**, *59* (3), 1758–1775.
199. Harvey, J. N.; Aschi, M.; Schwarz, H.; Koch, W. The Singlet and Triplet States of Phenyl Cation. A Hybrid Approach for Locating Minimum Energy Crossing Points between Non-Interacting Potential Energy Surfaces. *Theor. Chem. Acc.* **1998**, *99* (2), 95–99.
200. Marx, D.; Hutter, J. *Ab Initio Molecular Dynamics: Basic Theory and Advanced Methods*; Cambridge University Press, 2009.
201. Tomasi, J.; Persico, M. Molecular Interactions in Solution: An Overview of Methods Based on Continuous Distributions of the Solvent. *Chem. Rev.* **1994**, *94* (7), 2027–2094.
202. Miertuš, S.; Scrocco, E.; Tomasi, J. Electrostatic Interaction of a Solute with a Continuum. A Direct Utilizaion of AB Initio Molecular Potentials for the Prevision of Solvent Effects. *Chem. Phys.* **1981**, *55* (1), 117–129.
203. Marenich, A. V.; Cramer, C. J.; Truhlar, D. G. Universal Solvation Model Based on Solute Electron Density and on a Continuum Model of the Solvent Defined by the Bulk Dielectric Constant and Atomic Surface Tensions. *J. Phys. Chem. B* **2009**, *113* (18), 6378–6396.
204. Díez, J.; Gimeno, J.; Lledós, A.; Suárez, F. J.; Vicent, C. Imidazole Based Ruthenium(IV) Complexes as Highly Efficient Bifunctional Catalysts for the Redox Isomerization of Allylic Alcohols in Aqueous Medium: Water as Cooperating Ligand. *ACS Catal.* **2012**, *2* (10), 2087–2099.
205. Ortuño, M. A.; Lledós, A.; Maseras, F.; Ujaque, G. The Transmetalation Process in Suzuki–Miyaura Reactions: Calculations Indicate Lower Barrier via Boronate Intermediate. *ChemCatChem* **2014**, *6* (11), 3132–3138.
206. Sunoj, R. B.; Anand, M. Microsolvated Transition State Models for Improved Insight into Chemical Properties and Reaction Mechanisms. *Phys. Chem. Chem. Phys.* **2012**, *14* (37), 12715–12736.
207. Fattebert, J.-L.; Gygi, F. First-Principles Molecular Dynamics Simulations in a Continuum Solvent. *Int. J. Quantum Chem.* **2003**, *93* (2), 139–147.

208. Scherlis, D. A.; Fattebert, J.-L.; Gygi, F.; Cococcioni, M.; Marzari, N. A Unified Electrostatic and Cavitation Model for First-Principles Molecular Dynamics in Solution. *J. Chem. Phys.* **2006**, *124* (7), 074103-074110.
209. Tamura, H.; Yamazaki, H.; Sato, H.; Sakaki, S. Iridium-Catalyzed Borylation of Benzene with Diboron. Theoretical Elucidation of Catalytic Cycle Including Unusual Iridium(V) Intermediate. *J. Am. Chem. Soc.* **2003**, *125* (51), 16114–16126.
210. Sakaki, S.; Takayama, T.; Sumimoto, M.; Sugimoto, M. Theoretical Study of the Cp2Zr-Catalyzed Hydrosilylation of Ethylene. Reaction Mechanism Including New σ-Bond Activation. *J. Am. Chem. Soc.* **2004**, *126* (10), 3332–3348.
211. Wertz, D. H. Relationship between the Gas-Phase Entropies of Molecules and Their Entropies of Solvation in Water and 1-Octanol. *J. Am. Chem. Soc.* **1980**, *102* (16), 5316–5322.
212. Vilella, L.; Vidossich, P.; Balcells, D.; Lledós, A. Basic Ancillary Ligands Promote O–O Bond Formation in Iridium-Catalyzed Water Oxidation: A DFT Study. *Dalton Trans.* **2011**, *40* (42), 11241–11247.
213. Kärkäs, M. D.; Verho, O.; Johnston, E. V.; Åkermark, B. Artificial Photosynthesis: Molecular Systems for Catalytic Water Oxidation. *Chem. Rev.* **2014**, *114* (24), 11863–12001.
214. Blakemore, J. D.; Crabtree, R. H.; Brudvig, G. W. Molecular Catalysts for Water Oxidation. *Chem. Rev.* **2015**. DOI:10.1038/ncomms7469
215. Gilbert, J. A.; Eggleston, D. S.; Murphy, W. R.; Geselowitz, D. A.; Gersten, S. W.; Hodgson, D. J.; Meyer, T. J. Structure and Redox Properties of the Water-Oxidation Catalyst $[(bpy)_2(OH_2)RuORu(OH_2)(bpy)_2]^{4+}$. *J. Am. Chem. Soc.* **1985**, *107* (13), 3855–3864.
216. Betley, T. A.; Wu, Q.; Van Voorhis, T.; Nocera, D. G. Electronic Design Criteria for O−O Bond Formation via Metal−Oxo Complexes. *Inorg. Chem.* **2008**, *47* (6), 1849–1861.
217. Concepcion, J. J.; Jurss, J. W.; Norris, M. R.; Chen, Z.; Templeton, J. L.; Meyer, T. J. Catalytic Water Oxidation by Single-Site Ruthenium Catalysts. *Inorg. Chem.* **2010**, *49* (4), 1277–1279.
218. Savini, A.; Bucci, A.; Bellachioma, G.; Rocchigiani, L.; Zuccaccia, C.; Llobet, A.; Macchioni, A. Mechanistic Aspects of Water Oxidation Catalyzed by Organometallic Iridium Complexes. *Eur. J. Inorg. Chem.* **2014**, *2014* (4), 690–697.
219. Concepcion, J. J.; Tsai, M.-K.; Muckerman, J. T.; Meyer, T. J. Mechanism of Water Oxidation by Single-Site Ruthenium Complex Catalysts. *J. Am. Chem. Soc.* **2010**, *132* (5), 1545–1557.

220. Lin, X.; Hu, X.; Concepcion, J. J.; Chen, Z.; Liu, S.; Meyer, T. J.; Yang, W. Theoretical Study of Catalytic Mechanism for Single-Site Water Oxidation Process. *Proc. Natl. Acad. Sci.* **2012**, *109* (39), 15669–15672.
221. Gao, Y.; Åkermark, T.; Liu, J.; Sun, L.; Åkermark, B. Nucleophilic Attack of Hydroxide on a MnV Oxo Complex: A Model of the O−O Bond Formation in the Oxygen Evolving Complex of Photosystem II. *J. Am. Chem. Soc.* **2009**, *131* (25), 8726–8727.
222. Balcells, D.; Raynaud, C.; Crabtree, R. H.; Eisenstein, O. A Rational Basis for the Axial Ligand Effect in C−H Oxidation by [MnO(porphyrin)(X)]+ (X = $H_2O$, $OH^-$, $O^{2-}$) from a DFT Study. *Inorg. Chem.* **2008**, *47* (21), 10090–10099.
223. De Angelis, F.; Jin, N.; Car, R.; Groves, J. T. Electronic Structure and Reactivity of Isomeric Oxo-Mn(V) Porphyrins: Effects of Spin-State Crossing and pKa Modulation. *Inorg. Chem.* **2006**, *45* (10), 4268–4276.
224 Gaussian 09, Revision D.01, Frisch, M. J.; Trucks, G. W.; Schlegel, H. B.; Scuseria, G. E.; Robb, M. A.; Cheeseman, J. R.
225. Martin, R. L.; Hay, P. J.; Pratt, L. R. Hydrolysis of Ferric Ion in Water and Conformational Equilibrium. *J. Phys. Chem. A* **1998**, *102* (20), 3565–3573.
226. Sieffert, N.; Bühl, M. Hydrogen Generation from Alcohols Catalyzed by Ruthenium−Triphenylphosphine Complexes: Multiple Reaction Pathways. *J. Am. Chem. Soc.* **2010**, *132* (23), 8056–8070.
227. Anderson, T. M.; Neiwert, W. A.; Kirk, M. L.; Piccoli, P. M. B.; Schultz, A. J.; Koetzle, T. F.; Musaev, D. G.; Morokuma, K.; Cao, R.; Hill, C. L. A Late-Transition Metal Oxo Complex: $K_7Na_9[O{=}PtIV(H_2O)L_2]$, L = $[PW_9O_{34}]^{9-}$. *Science* **2004**, *306* (5704), 2074–2077.
228. Duan, L.; Xu, Y.; Gorlov, M.; Tong, L.; Andersson, S.; Sun, L. Chemical and Photochemical Water Oxidation Catalyzed by Mononuclear Ruthenium Complexes with a Negatively Charged Tridentate Ligand. *Chem. – Eur. J.* **2010**, *16* (15), 4659–4668.
229. Dogutan, D. K.; McGuire, R.; Nocera, D. G. Electocatalytic Water Oxidation by Cobalt(III) Hangman β-Octafluoro Corroles. *J. Am. Chem. Soc.* **2011**, *133* (24), 9178–9180.
230. McCrory, C. C. L.; Jung, S.; Peters, J. C.; Jaramillo, T. F. Benchmarking Heterogeneous Electrocatalysts for the Oxygen Evolution Reaction. *J. Am. Chem. Soc.* **2013**, *135* (45), 16977–16987.
231. Llobet A. *Molecular Water Oxidation Catalysis: A Key Topic for New Sustainable Energy Conversion Schemes*; John Wiley & Sons, Ltd, 2014.

232. McCrory, C. C. L.; Jung, S.; Ferrer, I. M.; Chatman, S. M.; Peters, J. C.; Jaramillo, T. F. Benchmarking Hydrogen Evolving Reaction and Oxygen Evolving Reaction Electrocatalysts for Solar Water Splitting Devices. *J. Am. Chem. Soc.* **2015**, *137* (13), 4347–4357.
233. Vesborg, P. C. K.; Jaramillo, T. F. Addressing the Terawatt Challenge: Scalability in the Supply of Chemical Elements for Renewable Energy. *RSC Adv.* **2012**, *2* (21), 7933–7947.
234. Tagore, R.; Crabtree, R. H.; Brudvig, G. W. Oxygen Evolution Catalysis by a Dimanganese Complex and Its Relation to Photosynthetic Water Oxidation. *Inorg. Chem.* **2008**, *47* (6), 1815–1823.
235. Mullins, C. S; Pecoraro, V. L. Reflections on Small Molecule Manganese Models That Seek to Mimic Photosynthetic Water Oxidation Chemistry. *Coord Chem Rev* **2008**, *252* (3-4), 416–443.
236. Zhang, C.; Chen, C.; Dong, H.; Shen, J.-R.; Dau, H.; Zhao, J. A Synthetic $Mn_4Ca$-Cluster Mimicking the Oxygen-Evolving Center of Photosynthesis. *Science* **2015**, *348* (6235), 690–693.
237. Kanan, M. W.; Nocera, D. G. In Situ Formation of an Oxygen-Evolving Catalyst in Neutral Water Containing Phosphate and $Co^{2+}$. *Science* **2008**, *321* (5892), 1072–1075.
238. Haber, J. A.; Cai, Y.; Jung, S.; Xiang, C.; Mitrovic, S.; Jin, J.; Bell, A. T.; Gregoire, J. M. Discovering Ce-Rich Oxygen Evolution Catalysts, from High Throughput Screening to Water Electrolysis. *Energy Environ. Sci.* **2014**, *7* (2), 682–688.
239. Park, J. H.; Kim, S.; Bard, A. J. Novel Carbon-Doped $TiO_2$ Nanotube Arrays with High Aspect Ratios for Efficient Solar Water Splitting. *Nano Lett.* **2006**, *6* (1), 24–28.
240. Fominykh, K.; Chernev, P.; Zaharieva, I.; Sicklinger, J.; Stefanic, G.; Döblinger, M.; Müller, A.; Pokharel, A.; Böcklein, S.; Scheu, C.; et al. Iron-Doped Nickel Oxide Nanocrystals as Highly Efficient Electrocatalysts for Alkaline Water Splitting. *ACS Nano* **2015**, *9* (5), 5180–5188.
241. Jiao, F.; Frei, H. Nanostructured Cobalt Oxide Clusters in Mesoporous Silica as Efficient Oxygen-Evolving Catalysts. *Angew. Chem. Int. Ed.* **2009**, *48* (10), 1841–1844.
242. Menezes, P. W.; Indra, A.; Littlewood, P.; Schwarze, M.; Göbel, C.; Schomäcker, R.; Driess, M. Nanostructured Manganese Oxides as Highly Active Water Oxidation Catalysts: A Boost from Manganese Precursor Chemistry. *ChemSusChem* **2014**, *7* (8), 2202–2211.
243. Concepcion, J. J.; Binstead, R. A.; Alibabaei, L.; Meyer, T. J. Application of the Rotating Ring-Disc-Electrode Technique to Water Oxidation by Surface-Bound Molecular Catalysts. *Inorg. Chem.* **2013**, *52* (19), 10744–10746.

244. Klepser, B. M.; Bartlett, B. M. Anchoring a Molecular Iron Catalyst to Solar-Responsive $WO_3$ Improves the Rate and Selectivity of Photoelectrochemical Water Oxidation. *J. Am. Chem. Soc.* **2014**, *136* (5), 1694–1697.
245. Hintermair, U.; Hashmi, S. M.; Elimelech, M.; Crabtree, R. H. Particle Formation during Oxidation Catalysis with Cp* Iridium Complexes. *J. Am. Chem. Soc.* **2012**, *134* (23), 9785–9795.
246. Nørskov, J. K.; Rossmeisl, J.; Logadottir, A.; Lindqvist, L.; Kitchin, J. R.; Bligaard, T.; Jónsson, H. Origin of the Overpotential for Oxygen Reduction at a Fuel-Cell Cathode. *J. Phys. Chem. B* **2004**, *108* (46), 17886–17892.
247. Perdew, J. P.; Burke, K.; Ernzerhof, M. Generalized Gradient Approximation Made Simple. *Phys. Rev. Lett.* **1996**, *77* (18), 3865–3868.
248. Kresse, G.; Furthmüller, J. Efficient Iterative Schemes for Ab Initio Total-Energy Calculations Using a Plane-Wave Basis Set. *Phys. Rev. B* **1996**, *54* (16), 11169–11186.
249. Kresse, G.; Furthmüller, J. Efficiency of Ab-Initio Total Energy Calculations for Metals and Semiconductors Using a Plane-Wave Basis Set. *Comput Mater Sci* **1996**, *6* (1), 15–50.
250. Zhang, H.; Soon, A.; Delley, B.; Stampfl, C. Stability, Structure, and Electronic Properties of Chemisorbed Oxygen and Thin Surface Oxides on Ir(111). *Phys. Rev. B* **2008**, *78* (4), 045436-045447.
251. Sen, F. G.; Kinaci, A.; Narayanan, B.; Gray, S. K.; Davis, M. J.; Sankaranarayanan, S. K. R. S.; Chan, M. K. Y. Towards Accurate Prediction of Catalytic Activity in $IrO_2$ Nanoclusters via First Principles-Based Variable Charge Force Field. *J. Mater. Chem. A* **2015**. DOI: 10.1039/C5TA04678E.
252. Bolzan, A. A.; Fong, C.; Kennedy, B. J.; Howard, C. J. Structural Studies of Rutile-Type Metal Dioxides. *Acta Crystallogr. Sect. B* **1997**, *53* (3), 373–380.
253. Lee, Y.; Suntivich, J.; May, K. J.; Perry, E. E.; Shao-Horn, Y. Synthesis and Activities of Rutile $IrO_2$ and $RuO_2$ Nanoparticles for Oxygen Evolution in Acid and Alkaline Solutions. *J. Phys. Chem. Lett.* **2012**, *3* (3), 399–404.
254. Rossmeisl, J.; Logadottir, A.; Nørskov, J. Electrolysis of Water on (oxidized) Metal Surfaces. *Chem Phys* **2005**, *319* (1-3), 178–184.
255. Klüpfel, S.; Klüpfel, P.; Jónsson, H. The Effect of the Perdew-Zunger Self-Interaction Correction to Density Functionals on the Energetics of Small Molecules. *J. Chem. Phys.* **2012**, *137* (12), 124102- 124112.

256. Doyle, A. D.; Montoya, J. H.; Vojvodic, A. Improving Oxygen Electrochemistry through Nanoscopic Confinement. *ChemCatChem* **2015**, *7* (5), 709–709.
257. Gong, Y.; Zhou, M.; Kaupp, M.; Riedel, S. Formation and Characterization of the Iridium Tetroxide Molecule with Iridium in the Oxidation State +VIII. *Angew. Chem. Int. Ed.* **2009**, *48* (42), 7879–7883.
258. Wang, G.; Zhou, M.; Goettel, J. T.; Schrobilgen, G. J.; Su, J.; Li, J.; Schlöder, T.; Riedel, S. Identification of an Iridium-Containing Compound with a Formal Oxidation State of IX. *Nature* **2014**, *514* (7523), 475–477.
259. Hintermair, U.; Hashmi, S. M.; Elimelech, M.; Crabtree, R. H. Particle Formation during Oxidation Catalysis with Cp* Iridium Complexes. *J. Am. Chem. Soc.* **2012**, *134* (23), 9785–9795.
260. Barton, D. H. R. *The Activation of Dioxygen and Homogeneous Catalytic Oxidation*; Springer US: New York, 1993.
261. Boisvert, L.; Goldberg, K. I. Reactions of Late Transition Metal Complexes with Molecular Oxygen. *Acc. Chem. Res.* **2012**, *45* (6), 899–910.
262. Stahl, S. S. Palladium Oxidase Catalysis: Selective Oxidation of Organic Chemicals by Direct Dioxygen-Coupled Turnover. *Angew. Chem. Int. Ed.* **2004**, *43* (26), 3400–3420.
263. Vedernikov, A. N. Direct Functionalization of M–C (M = PtII, PdII) Bonds Using Environmentally Benign Oxidants, $O_2$ and $H_2O_2$. *Acc. Chem. Res.* **2011**, *45* (6), 803–813.
264. M. A. Barteau; R. J. Madix. *The Chemical Physics of Solid Surfaces and Heterogeneous Catalysis*; Elsevier: Amsterdam, 1982.
265. Serafin, J. G.; Liu, A. C.; Seyedmonir, S. R. Surface Science and the Silver-Catalyzed Epoxidation of Ethylene: An Industrial Perspective. *J. Mol. Catal. Chem.* **1998**, *131* (1–3), 157–168.
266. Tejel, C.; Ciriano, M. A. Catalysis and Organometallic Chemistry of Rhodium and Iridium in the Oxidation of Organic Substrates. In *Organometallic Oxidation Catalysis*; Meyer, F., Limberg, C., Eds.; Topics in Organometallic Chemistry; Springer Berlin Heidelberg, 2006; pp 97–124.
267. Dauth, A.; Love, J. A. Reactivity by Design-Metallaoxetanes as Centerpieces in Reaction Development. *Chem. Rev.* **2011**, *111* (3), 2010–2047.
268. Feller, D. The Role of Databases in Support of Computational Chemistry Calculations. *J. Comput. Chem.* **1996**, *17* (13), 1571–1586.
269. Schuchardt, K. L.; Didier, B. T.; Elsethagen, T.; Sun, L.; Gurumoorthi, V.; Chase, J.; Li, J.; Windus, T. L. Basis Set

Exchange: A Community Database for Computational Sciences. *J. Chem. Inf. Model.* **2007**, *47* (3), 1045–1052.

270. Roy, L. E.; Hay, P. J.; Martin, R. L. Revised Basis Sets for the LANL Effective Core Potentials. *J. Chem. Theory Comput.* **2008**, *4* (7), 1029–1031.
271. Cooper, J.; Ziegler, T. A Density Functional Study of SN2 Substitution at Square-Planar Platinum(II) Complexes. *Inorg. Chem.* **2002**, *41* (25), 6614–6622.
272. Zhu, H.; Ziegler, T. Influence of Cis and Trans Ligands in Platinum(II) Complexes on the Ability of the Platinum Center to Activate C−H Bonds. A Density Functional Theory Study. *Organometallics* **2008**, *27* (8), 1743–1749.
273. Ben-Naim, A.; Marcus, Y. Solvation Thermodynamics of Nonionic Solutes. *J. Chem. Phys.* **1984**, *81* (4), 2016–2027.
274. Bryantsev, V. S.; Diallo, M. S.; Goddard III, W. A. Calculation of Solvation Free Energies of Charged Solutes Using Mixed Cluster/Continuum Models. *J. Phys. Chem. B* **2008**, *112* (32), 9709–9719.
275. Yamaguchi, K.; Jensen, F.; Dorigo, A.; Houk, K. N. A Spin Correction Procedure for Unrestricted Hartree-Fock and Møller-Plesset Wavefunctions for Singlet Diradicals and Polyradicals. *Chem. Phys. Lett.* **1988**, *149* (5–6), 537–542.
276. Yamanaka, S.; Kawakami, T.; Nagao, H.; Yamaguchi, K. Effective Exchange Integrals for Open-Shell Species by Density Functional Methods. *Chem. Phys. Lett.* **1994**, *231* (1), 25–33.
277. NBO 6.0. Glendening, E. D.; Badenhoop, J, K.; Reed, A. E.; Carpenter, J. E.; Bohmann, J. A.; Morales, C. M.; Landis, C.
278. Cramer, C. J.; Tolman, W. B.; Theopold, K. H.; Rheingold, A. L. Variable Character of O-O and M-O Bonding in Side-on ($\eta^2$) 1:1 Metal Complexes of $O_2$. *Proc. Natl. Acad. Sci.* **2003**, *100* (7), 3635–3640..
279 Woertink, J. S.; Tian, L.; Maiti, D.; Lucas, H. R.; Himes, R. A.; Karlin, K. D.; Neese, F.; Würtele, C.; Holthausen, M. C.; Bill, E.; et al. Spectroscopic and Computational Studies of an End-on Bound Superoxo-Cu(II) Complex: Geometric and Electronic Factors That Determine the Ground State. *Inorg. Chem.* **2010**, *49* (20), 9450–9459.
280 Solomon, E. I.; Heppner, D. E.; Johnston, E. M.; Ginsbach, J. W.; Cirera, J.; Qayyum, M.; Kieber-Emmons, M. T.; Kjaergaard, C. H.; Hadt, R. G.; Tian, L. Copper Active Sites in Biology. *Chem. Rev.* **2014**, *114* (7), 3659–3853.
281. Lewis, E. A.; Tolman, W. B. Reactivity of Dioxygen−Copper Systems. *Chem. Rev.* **2004**, *104* (2), 1047–1076.

282. Cho, J.; Sarangi, R.; Nam, W. Mononuclear Metal-$O_2$ Complexes Bearing Macrocyclic N-Tetramethylated Cyclam Ligands. *Acc. Chem. Res.* **2012**, *45* (8), 1321–1330.
283. Krom, M.; Coumans, R. G. E.; Smits, J. M. M.; Gal, A. W. Rearrangement of 3-Rhoda-1,2-Dioxolanes to Rhodium Formylmethyl Hydroxy Complexes. *Angew. Chem.* **2002**, *114* (4), 595–599.
284. García-Melchor, M.; Gorelsky, S. I.; Woo, T. K. Mechanistic Analysis of Iridium(III) Catalyzed Direct C-H Arylations: A DFT Study. *Chem. – Eur. J.* **2011**, *17* (49), 13847–13853.
285. Legault, C. Y.; Garcia, Y.; Merlic, C. A.; Houk, K. N. Origin of Regioselectivity in Palladium-Catalyzed Cross-Coupling Reactions of Polyhalogenated Heterocycles. *J. Am. Chem. Soc.* **2007**, *129* (42), 12664–12665.
286. Fernández, I.; Bickelhaupt, F. M. The Activation Strain Model and Molecular Orbital Theory: Understanding and Designing Chemical Reactions. *Chem. Soc. Rev.* **2014**, *43* (14), 4953–4967.
287. Strukul, G. *Catalytic Oxidations with Hydrogen Peroxide as Oxidant*; Springer: The Netherlands, 1992.
288. Sheldon, R. A.; Kochi, J. K.; Kochi, J. K. *Metal-Catalyzed Oxidations of Organic Compounds*; Sheldon, R. A., Ed.; Academic Press: New York, 1981.
289. Raba, A.; Cokoja, M.; Herrmann, W. A.; Kuhn, F. E. Catalytic Hydroxylation of Benzene and Toluene by an Iron Complex Bearing a Chelating Di-Pyridyl-Di-NHC Ligand. *ChemComm 50*, 11454-11457.
290. Shoji, O.; Kunimatsu, T.; Kawakami, N.; Watanabe, Y. Highly Selective Hydroxylation of Benzene to Phenol by Wild-Type Cytochrome P450BM3 Assisted by Decoy Molecules. *Angew. Chem. Int. Ed.* **2013**, *52* (26), 6606–6610.
291. Niwa, S.; Eswaramoorthy, M.; Nair, J.; Raj, A.; Itoh, N.; Shoji, H.; Namba, T.; Mizukami, F. A One-Step Conversion of Benzene to Phenol with a Palladium Membrane. *Science* **2002**, *295* (5552), 105–107.
292. Tani, M.; Sakamoto, T.; Mita, S.; Sakaguchi, S.; Ishii, Y. Hydroxylation of Benzene to Phenol under Air and Carbon Monoxide Catalyzed by Molybdovanadophosphoric Acid. *Angew. Chem. Int. Ed.* **2005**, *44* (17), 2586–2588.
293. Jia, J.; Pillai, K. S.; Sachtler, W. M. H. One-Step Oxidation of Benzene to Phenol with Nitrous Oxide over Fe/MFI Catalysts. *J. Catal.* **2004**, *221* (1), 119–126.
294. Nelly A. Kachurovskaya; Georgii M. Zhidomirov; Emiel J.M. Hensen; Rutger A. van Santen. Cluster Model DFT Study of the

Intermediates of Benzene to Phenol Oxidation by $N_2O$ on FeZSM-5 Zeolites. *Catal. Lett.* **2003**, *86* (1-3), 25–31.
295. Centi, G.; Perathoner, S. One-Step $H_2O_2$ and Phenol Syntheses: Examples of Challenges for New Sustainable Selective Oxidation Processes. *Catal. Today* **2009**, *143* (1–2), 145–150.
296. Patrícia M. Reis; José Armando L. Silva; João J.R. Fraústo da Silva; Armando J.L. Pombeiro. Peroxidative Oxidation of Benzene and Mesitylene by Vanadium Catalysts. *J. Mol. Catal. Chem.* **2004**, *224* (1-2), 189–195.
297. Ito, S.; Mitarai, A.; Hikino, K.; Hirama, M.; Sasaki, K. Deactivation Reaction in the Hydroxylation of Benzene with Fenton's Reagent. *J. Org. Chem.* **1992**, *57* (25), 6937–6941.
298. Walling, C.; Johnson, R. A. Fenton's Reagent. V. Hydroxylation and Side-Chain Cleavage of Aromatics. *J. Am. Chem. Soc.* **1975**, *97* (2), 363–367.
299. Bianchi, D.; Bortolo, R.; Tassinari, R.; Ricci, M.; Vignola, R. A Novel Iron-Based Catalyst for the Biphasic Oxidation of Benzene to Phenol with Hydrogen Peroxide. *Angew. Chem.* **2000**, *112* (23), 4491–4493.
300. Conde, A.; Díaz-Requejo, M. M.; Pérez, P. J. Direct, Copper-Catalyzed Oxidation of Aromatic C–H Bonds with Hydrogen Peroxide under Acid-Free Conditions. *Chem. Commun.* **2011**, *47* (28), 8154–8156.
301. Brillas, E.; Sirés, I.; Oturan, M. A. Electro-Fenton Process and Related Electrochemical Technologies Based on Fenton's Reaction Chemistry. *Chem. Rev.* **2009**, *109* (12), 6570–6631.
302. Chow, T. W.-S.; Liu, Y.; Che, C.-M. Practical Manganese-Catalysed Highly Enantioselective Cis-Dihydroxylation of Electron-Deficient Alkenes and Detection of a Cis-dioxomanganese(V) Intermediate by High Resolution ESI-MS Analysis. *Chem. Commun.* **2011**, *47* (40), 11204–11206.
303. Hage, J. P.; Llobet, A.; Sawyer, D. T. Aromatic Hydroxylation by Fenton Reagents {Reactive intermediate[Lx+FeIIIOOH(BH+)], Not Free Hydroxyl Radical (HO·)}. *Bioorg. Med. Chem.* **1995**, *3* (10), 1383–1388.
304. Marusawa, H.; Ichikawa, K.; Narita, N.; Murakam, H.; Ito, K.; Tezuka, T. Hydroxyl Radical as a Strong Electrophilic Species. *Bioorg. Med. Chem.* **2002**, *10* (7), 2283–2290.
305. Bossmann, S. H.; Oliveros, E.; Göb, S.; Siegwart, S.; Dahlen, E. P.; Payawan, L.; Straub, M.; Wörner, M.; Braun, A. M. New Evidence against Hydroxyl Radicals as Reactive Intermediates in the Thermal and Photochemically Enhanced Fenton Reactions. *J. Phys. Chem. A* **1998**, *102* (28), 5542–5550.

306. Hammett, L. P. The Effect of Structure upon the Reactions of Organic Compounds. Benzene Derivatives. *J. Am. Chem. Soc.* **1937**, *59* (1), 96–103.
307. Hammett, L. P. Some Relations between Reaction Rates and Equilibrium Constants. *Chem. Rev.* **1935**, *17* (1), 125–136.
308. Reed, A. E.; Curtiss, L. A.; Weinhold, F. Intermolecular Interactions from a Natural Bond Orbital, Donor-Acceptor Viewpoint. *Chem. Rev.* **1988**, *88* (6), 899–926.
309. Güell, M.; Luis, J. M.; Siegbahn, P. E. M.; Solà, M. Theoretical Study of the Hydroxylation of Phenols Mediated by an End-on Bound superoxo–copper(II) Complex. *J. Biol. Inorg. Chem.* **2008**, *14* (2), 273–285.
310. Crespo, A.; Martí, M. A.; Roitberg, A. E.; Amzel, L. M.; Estrin, D. A. The Catalytic Mechanism of Peptidylglycine α-Hydroxylating Monooxygenase Investigated by Computer Simulation. *J. Am. Chem. Soc.* **2006**, *128* (39), 12817–12828.
311. Garcia-Bosch, I.; Company, A.; Cady, C. W.; Styring, S.; Browne, W. R.; Ribas, X.; Costas, M. Evidence for a Precursor Complex in C-H Hydrogen Atom Transfer Reactions Mediated by a Manganese(IV) Oxo Complex. *Angew. Chem. Int. Ed.* **2011**, *50* (25), 5648–5653.
312. Wheland. Quantum Mechanical Investigation of the Orientation of Substituents in Aromatic Molecules. *J Amer Chem Soc* **1942**, *64*, 900-908.
313. Clayden, J.; Greeves, N.; Warren, S.; Wothers, P. *Organic Chemistry*, 1st ed.; Oxford University Press, 2001.
314. Capponi, M.; Gut, I. G.; Hellrung, B.; Persy, G.; Wirz, J. Ketonization Equilibria of Phenol in Aqueous Solution. *Can J Chem* **1999**, *77* (5-6), 605–613.
315. Jia, C.; Kitamura, T.; Fujiwara, Y. Catalytic Functionalization of Arenes and Alkanes via C−H Bond Activation. *Acc. Chem. Res.* **2001**, *34* (8), 633–639.
316. Nashed, N. T.; Sayer, J. M.; Jerina, D. M. Acid-Catalyzed Rearrangement of K-Region Arene Oxides: Observation of Ketone Intermediates and a Sterically Induced Change in Rate-Determining Step. *J. Am. Chem. Soc.* **1993**, *115* (5), 1723–1730.
317. Hassner, A. *The Chemistry of Heterocyclic Compounds, Small Ring Heterocycles*; John Wiley & Sons, 2009.
318. Yoshizawa, K.; Kihara, N.; Kamachi, T.; Shiota, Y. Catalytic Mechanism of Dopamine ß-Monooxygenase Mediated by Cu(III)−Oxo. *Inorg. Chem.* **2006**, *45* (7), 3034–3041.
319. Conde, A.; Vilella, L.; Balcells, D.; Díaz-Requejo, M. M.; Lledós, A.; Pérez, P. J. Introducing Copper as Catalyst for Oxidative Alkane Dehydrogenation. *J. Am. Chem. Soc.* **2013**, *135* (10), 3887–3896.

320. Kim, C.; Dong, Y.; Que, L. Modeling Nonheme Diiron Enzymes: Hydrocarbon Hydroxylation and Desaturation by a High-Valent $Fe_2O_2$ Diamond Core. *J. Am. Chem. Soc.* **1997**, *119* (15), 3635–3636.
321. Balcells, D.; Raynaud, C.; Crabtree, R. H.; Eisenstein, O. C–H Oxidation by Hydroxo manganese(V) Porphyrins: A DFT Study. *Chem. Commun.* **2009**, No. 13, 1772–1774.
322. Shi, S.; Wang, Y.; Xu, A.; Wang, H.; Zhu, D.; Roy, S. B.; Jackson, T. A.; Busch, D. H.; Yin, G. Distinct Reactivity Differences of Metal Oxo and Its Corresponding Hydroxo Moieties in Oxidations: Implications from a Manganese(IV) Complex Having Dihydroxide Ligand. *Angew. Chem. Int. Ed.* **2011**, *50* (32), 7321–7324.
323. Luo, Y.-R. *Comprehensive Handbook of Chemical Bond Energies*; CRC Press:BocaRatoń: FL, 2007.
324. Kopylovich, M. N.; Mahmudov, K. T.; Haukka, M.; Figiel, P. J.; Mizar, A.; da Silva, J. A. L.; Pombeiro, A. J. L. Water-Soluble Cobalt(II) and Copper(II) Complexes of 3-(5-Chloro-2-Hydroxy-3-Sulfophenylhydrazo)pentane-2,4-Dione as Building Blocks for 3D Supramolecular Networks and Catalysts for TEMPO-Mediated Aerobic Oxidation of Benzylic Alcohols. *Eur. J. Inorg. Chem.* **2011**, *2011* (27), 4175–4181.
325. Goberna-Ferrón, S.; Lillo, V.; Galán-Mascarós J. R. [Cu(L-prolinate)$_2$]: A Catalyst for Environmentally Friendly Oxidation of Alkanes and Alkenes with $H_2O_2$ and $O_2$. *Catal. Commun.* **2012**, *23*, 30–33.
326. Barton, D.H.R.; Bévière, S. D.; Chavasiri, W.; Csuhai, E.; Doller, D. The Functionalisation of Saturated Hydrocarbons. Part XXI. The Fe(III)-Catalyzed and the Cu(II)-Catalyzed Oxidation of Saturated Hydrocarbons by Hydrogen Peroxide: A Comparative Study. *Tetrahedron* **1992**, *48* (14), 2895–2910.
327. Kirillova, M. V.; Kirillov, A. M.; Guedes da Silva, M. F. C.; Pombeiro, A. J. L. Self-Assembled Two-Dimensional Water-Soluble Dipicolinate Cu/Na Coordination Polymer: Structural Features and Catalytic Activity for the Mild Peroxidative Oxidation of Cycloalkanes in Acid-Free Medium. *Eur. J. Inorg. Chem.* **2008**, *2008* (22), 3423–3427.
328. Siegbahn, P. E. M.; Crabtree, R. H. Manganese Oxyl Radical Intermediates and O−O Bond Formation in Photosynthetic Oxygen Evolution and a Proposed Role for the Calcium Cofactor in Photosystem II. *J. Am. Chem. Soc.* **1999**, *121* (1), 117–127.
329. Shaik, S.; Cohen, S.; Wang, Y.; Chen, H.; Kumar, D.; Thiel, W. P450 Enzymes: Their Structure, Reactivity, and Selectivity-Modeled by QM/MM Calculations. *Chem. Rev.* **2010**, *110* (2), 949–1017.

330. Meunier, B.; de Visser, S. P.; Shaik, S. Mechanism of Oxidation Reactions Catalyzed by Cytochrome P450 Enzymes. *Chem. Rev.* **2004**, *104* (9), 3947–3980.
331. Sawyer, D. T.; Kang, C.; Llobet, A.; Redman, C. Fenton Reagents (1:1 FeIILx/HOOH) React via [LxFeIIOOH(BH+)] (1) as Hydroxylases (RH .fwdarw. ROH), Not as Generators of Free Hydroxyl Radicals (HO.bul.). *J. Am. Chem. Soc.* **1993**, *115* (13), 5817–5818.